PREPARATION AND CHARACTERIZATION OF ALTERNATIVE POROUS MATERIALS FOR HYDROGEN STORAGE

PhD Dissertation

Orkun ERGÜRHAN

Eskişehir 2025

PREPARATION AND CHARACTERIZATION OF ALTERNATIVE POROUS MATERIALS FOR HYDROGEN STORAGE

Orkun ERGÜRHAN

PhD DISSERTATION

Department of Physics

Programme in General Physics

Supervisor: Prof. Dr. Burcu ERDOĞAN

Eskişehir

Eskişehir Technical University

Institute of Graduate Programs

June 2025

This thesis has been supported by the Scientific and Technological Research Council of Turkey (TÜBİTAK) under the Grant No. 124F012 and by the Eskişehir Technical University Scientific Research Projects Committee under Grant No. 22DRP360.

FINAL APPROVAL FOR THESIS

This thesis titled PREPARATION AND CHARACTERIZATION OF ALTERNATIVE POROUS MATERIALS FOR HYDROGEN STORAGE has been prepared and submitted by Orkun ERGÜRHAN in partial fulfillment of the requirements in "Eskişehir Technical University Directive on Graduate Education and Examination" for the Degree of PhD in Physics Department has been examined and approved on 13/06/2025.

Committee Members		**Title, Name and Surname**	**Signature**
Member	:	Prof. Dr. Burcu ERDOĞAN	
Member	:	Prof. Dr. Haldun KURAMA	
Member	:	Prof. Dr. İdris AKYÜZ	
Member	:	Prof. Dr. Ünal ŞEN	
Member	:	Assoc. Prof. Dr. Bilge ERDEM	

Prof. Dr. Harun BÖCÜK
Director of the Institute of Graduate Programs

13/06/2025

SUPERVISOR APPROVAL

PhD student Orkun ERGÜRHAN, whom I supervise, has completed this thesis titled PREPARATION AND CHARACTERIZATION OF ALTERNATIVE POROUS MATERIALS FOR HYDROGEN STORAGE. According to my inspections, the work is scientifically and ethically appropriate for the student to the thesis defense exam.

Supervisor
Prof. Dr. Burcu ERDOĞAN

ABSTRACT

PREPARATION AND CHARACTERIZATION OF ALTERNATIVE POROUS MATERIALS FOR HYDROGEN STORAGE

Orkun ERGÜRHAN

Department of Physics

Programme in General Physics

Eskişehir Technical University, Institute of Graduate Programs, June 2025

Supervisor: Prof. Dr. Burcu ERDOĞAN

This thesis presents an investigation into the hydrogen storage properties of three distinct porous materials: clinoptilolite (CLN) and its cation-exchanged forms, ZIF-8 (a zeolitic imidazolate framework) and porous silicon nanowires (SiNWs). The Na^+, K^+, Li^+, Ag^+, Ni^{2+}, Ca^{2+}, Cu^{2+}, and Mg^{2+} cation exchange procedure was applied to the H^+ form of CLN, which was obtained by contacting 1.0 M NH_4NO_3 solution at 80 °C, followed by calcination at 450 °C. The synthesis of ZIF-8 and its in situ modified forms with Li^+ and Na^+ cations was accomplished via the solvo-thermal method. The two-step MACE procedure was used to synthesise Au and Li-doped porous Si nanowires. The characterization of the CLN and ZIF-8 samples was performed using XRD, XRF, SEM, FT-IR, and N_2 adsorption at 77 K. The SiNW samples were characterized by means of SEM, EDS, and N_2 adsorption at 77 K. The hydrogen adsorption isotherms of all samples were obtained at temperatures 77 K up to a pressure of 113 kPa. Among all CLN samples, the sample modified with 0.5 M $LiNO_3$ was found to have the highest H_2 storage capacity of 3.458 mmol g^{-1}. By contrast, in situ modification with $LiNO_3$ did not result in any noticeable improvement to the BET surface area or H_2 storage performance of ZIF-8 samples. The H_2 adsorption capacities of the porous SiNWs were found to be the lowest among all the samples examined.

Keywords: Adsorption, Clinoptilolite, Hydrogen storage, Porous Si nanowire, ZIF-8

ÖZET

HİDROJEN DEPOLAMA İÇİN ALTERNATİF GÖZENEKLİ MALZEMELERİN HAZIRLANMASI VE KARAKTERİZASYONU

Orkun ERGÜRHAN

Fizik Anabilim Dalı

Genel Fizik Bilim Dalı

Eskişehir Teknik Üniversitesi, Lisansüstü Eğitim Enstitüsü, Haziran 2025

Danışman: Prof. Dr. Burcu ERDOĞAN

Bu tez, üç farklı gözenekli malzemenin hidrojen depolama özelliklerine ilişkin bir araştırma sunmaktadır: bunlar klinoptilolit (CLN) ve katyon değiştirilmiş formları, ZIF-8 (bir zeolitik imidazolat çerçeve) ve gözenekli silikon nanotellerdir (SiNW'ler). Na^{+}, K^{+}, Li^{+}, Ag^{+}, Ni^{+2}, Ca^{+2}, Cu^{+2} ve Mg^{+2} içeren katyon değişim prosedürü, 1.0 M NH_4NO_3 çözeltisinin 80 °C'de temas ettirilmesinin ardından 450 °C'de kalsinasyonu sonucu elde edilen CLN'nin H^{+} formuna uygulanmıştır. ZIF-8'in ve Li^{+} ve Na^{+} katyonları ile modifiye edilmiş formlarının sentezi solvo-termal yöntemle gerçekleştirilmiştir. Au ve Li-katkılı gözenekli Si nanotelleri sentezlemek için iki aşamalı MACE prosedürü kullanılmıştır. CLN ve ZIF-8 örneklerinin karakterizasyonu XRD, XRF, SEM, FT-IR ve 77 K'de N_2 adsorpsiyonu kullanılarak gerçekleştirilmiştir. SiNW örnekleri ise SEM, EDS ve 77 K'de N_2 adsorpsiyonu ile karakterize edilmiştir. Tüm örneklerin hidrojen adsorpsiyon izotermleri 113 kPa basınca kadar 77 K sıcaklıkta elde edilmiştir. Tüm CLN numuneleri arasında, 0,5 M $LiNO_3$ ile modifiye edilen numunenin 3,458 mmol g^{-1} ile en yüksek H_2 depolama kapasitesine sahip olduğu bulunmuştur. Buna karşılık, $LiNO_3$ ile modifikasyon, ZIF-8 numunelerinin BET yüzey alanında veya H_2 depolama performansında gözle görülür bir iyileşme sağlamamıştır. Gözenekli SiNW'lerin H_2 adsorpsiyon kapasiteleri, incelenen tüm örnekler arasında en düşük olarak bulunmuştur.

Anahtar Sözcükler: Adsorpsiyon, Gözenekli Si nanotel, Hidrojen depolama, Klinoptilolit, ZIF-8.

ACKNOWLEDGEMENTS

I would like to express my deepest gratitude to my advisor, Prof. Dr. Burcu ERDOĞAN, for sharing her scientific knowledge and experience with me throughout my doctoral studies, and for trusting and encouraging me to navigate uncharted waters with confidence during the entirety of this journey. I also owe special thanks to Prof. Dr. İdris AKYÜZ and Assoc. Prof. Dr. Bilge ERDEM, who served on all of my thesis monitoring committees, embraced my work as if it were that of their own graduate students, provided valuable guidance whenever I encountered challenges, and consistently supported me throughout this process.

I am grateful to Prof. Dr. Uğur SERİNCAN, Assoc. Prof. Dr. Mustafa KULAKCI, and Asst. Prof. Dr. Burcu ARPAPAY, who welcomed me into their laboratories as one of their own students during the course of my experimental work, and who generously offered both scientific assistance and meaningful conversations that greatly enriched my academic and personal point of view.

I would also like to express my sincere appreciation to Prof. Dr. Metin KUL, Prof. Dr. Müjdat ÇAĞLAR and Prof. Dr. İlker AVAN for granting me access to their laboratories, which was essential to the completion of this research.

My heartfelt thanks go to my mother and father, whose unwavering support and unconditional love have enabled me to become who I am today.

I extend my gratitude to my four-legged companions, Şivo and Rego, who, despite the complexity of life, reminded me of its fundamentally simple nature.

Last but not least, I'd like to thank my wonderful colleague, dear wife, and lifelong friend, Ayşe Aygül YILMAZ ERGÜRHAN, who has had my back throughout my whole career. Her love, patience, wisdom, and support have brightened even my darkest moments, inspired and empowered me in times of hardship, to keep me moving forward.

This dissertation is dedicated to all those who endeavor to ascertain their place in the grand realm of existence...

Orkun ERGÜRHAN

13/06/2025

STATEMENT OF COMPLIANCE WITH ETHICAL PRINCIPLES AND RULES

I hereby truthfully declare that this thesis is an original work prepared by me; that I have behaved in accordance with the scientific ethical principles and rules throughout the stages of preparation, data collection, analysis and presentation of my work; that I have cited the sources of all the data and information that could be obtained within the scope of this study, and included these sources in the references section; and that this study has been scanned for plagiarism with "scientific plagiarism detection program" used by Eskişehir Technical University, and that "it does not have any plagiarism" whatsoever. I also declare that, if a case contrary to my declaration is detected in my work at any time, I hereby express my consent to all the ethical and legal consequences that are involved.

Orkun ERGÜRHAN

CONTENTS

Page

LIST OF TABLES

Page

LIST OF FIGURES

LIST OF IMAGES

Page

GLOSSARY OF SYMBOLS AND ABBREVIATIONS

ΔG	:	Change of Gibbs free energy
ΔH	:	Change of enthalpy
ΔS	:	Change of entropy
σ	:	Total surface area
BET	:	Brunauer, Emmett and Teller
BJH	:	Barrett–Joyner–Halenda
C	:	BET constant
CLN	:	Clinoptilolite
d_{hkl}	:	Spacing between planes of crystal with corresponding Miller indices hkl
DFT	:	Density Functional Theory
EDS	:	Energy Dispersive X-Ray Spectroscopy
FT-IR	:	Fourier Transform Infrared
MACE	:	Metal Assisted Chemical Etching
N_A	:	Avogadro's Number
P	:	Pressure
P_0	:	Saturation pressure
R	:	Gas constant
S_0	:	The cross-sectional surface area of adsorbed gas molecule
SEM	:	Scanning Electron Microscopy
SiNW	:	Silicon Nanowire
T	:	Temperature
V_m	:	Monolayer capacity
XRD	:	X-Ray Diffraction
XRF	:	X-Ray Fluorescence
ZIF	:	Zeolitic Imidazolate Framework

1. INTRODUCTION

Our species is distinguished by its ability to modify its environment technologically according to its daily needs. The path that began with a simple knife made from an ordinary stone leads humanity to the intersection of energy demand and the climate crisis. Since the Industrial Revolution, fossil fuels have been a vital source of energy, enabling the production of heat and pressure through combustion reactions. These energy sources have enabled the transportation, heating and electricity generation that are integral to modern society. It is a fact that the use of fossil fuels also produces greenhouse gases. Given the limited sources of these fuels, the search for new energy sources was inevitable. Renewable energy sources like solar and wind energy are a clear alternative to fossil fuels. These sources have been successfully employed in the production of electricity and domestic heating, but they have been less efficient in transportation applications. At this point, hydrogen energy emerged as the obvious candidate.

The utilization of hydrogen energy on a daily basis is contingent upon the effective storage of this versatile energy source. Conventional storage methods, such as pressurized tanks or liquification at cryogenic temperatures, have been shown to have certain disadvantages in terms of efficiency and security. The physical adsorption using nanoporous materials offers a safer and more cost-effective alternative to high-pressure or cryogenic hydrogen storage methods. It provides fast and reversible hydrogen uptake, outperforming metal hydrides in terms of kinetics and requiring lower energy for hydrogen release, as it operates without high temperatures. Although metal hydrides like MgH_2 are more suitable for large-scale hydrogen storage, physical adsorption is generally safer, as it avoids the emission of toxic byproducts. Overall, physical adsorption stands out as a highly promising method for hydrogen storage.

Consequently, the investigation of hydrogen storage technologies represents an active research area within the scientific community. It is evident that, due to their regeneration efficiency and secure storage, physical adsorption (physisorption) of molecular hydrogen in porous materials is a promising candidate for hydrogen storage applications. Zeolites, metal organic frameworks (MOFs), covalent organic frameworks, carbon nanotubes and activated carbons have been the focus of extensive research. Nevertheless, the ultimate material that meets the DOE targets remains to be identified.

1.1. Thesis Overview

This thesis investigates the storage performance of molecular hydrogen via physisorption of three different porous materials: clinoptilolite (a natural zeolite), ZIF-8 (a zeolitic imidazolate framework, sub-class of MOF family) and Si nanowires. The thesis is organized as follows:

- Chapter 2 gives a concise overview of hydrogen, its storage methods, literature review and the motivation behind this research.
- Chapter 3 describes the theory of adsorption and the physical background of the characterization methods used.
- Chapter 4 sets out the properties of the materials used in the thesis.
- Chapter 5 represents the synthesis procedures and experimental methods.
- Chapter 6 presents the results and discusses them.

2. MOTIVATION

The energy demand of humanity is an unavoidable part of daily life. In the early eras of human civilization, three major activities required external energy sources: cooking, forging and heating. At present, the most commonly used energy sources are combustion materials such as firewood or coal. However, the advent of the steam engine, as pioneered by Thomas Newcomen in 1792, and the subsequent Industrial Revolution led to a fundamental shift in the necessity of energy [1]. The necessity for this became apparent not only in terms of the sustenance of day-to-day living, but also with regard to the sustenance of technology. At that juncture, fossil fuels (coal, oil, and natural gas) were used on a global scale to meet this additional energy demand. However, the burning of fossil fuels has resulted in the release of greenhouse gases, including carbon dioxide and methane, into the atmosphere [2]. Greenhouse gases are compounds that, due to their physical properties, absorb and retain some of the infrared radiation emitted from the Earth's surface, preventing it from being reflected back into space and the atmosphere [3]. The phenomenon was first identified by the French scientist Jean-Baptiste Fourier in 1827. It is now well established that the concentration of greenhouse gases in the atmosphere is increasing. For example, the atmospheric concentration of CO_2, which was 280 ppm between 1000 and 1750, increased by 31% to 368 ppm in 2000 and 402 ppm in 2014 as a result of fossil fuel consumption [4].

Another issue with the use of fossil fuels is that these resources are finite. It can be argued that meeting energy demand is one of the most significant challenges facing contemporary civilization [5]. The expansion of the global economy and the continued growth of the world's population have led to an exponential increase in energy demand [6]. To illustrate, the energy consumption of 10 billion people at their current lifestyle level would require at least ten terawatts (TW) of energy, which is equivalent to 150 million barrels of oil per day (150 M BOE/day) [7]. In light of these concerns, scientists have turned their attention to the search for renewable energy sources that do not contribute to greenhouse gas emissions and can serve as a viable alternative to fossil fuels.

The term "renewable energy" has been used since the early 1990s as a concept to counter the depletion of fossil fuels [8]. Energy sources that were used before the advent of fossil fuels are now included in the concept of 'renewable energy'. For example, since the discovery of fire, biomass energy has been the primary source of energy for basic needs such as heating and cooking. Hydropower and wind energy have also been used by

man throughout history. The following sources can be classified as renewable energy sources: Biomass energy, wind energy, solar energy, hydroelectric energy, tidal energy and geothermal energy. These are resources that are continuously replenished within the Earth's natural cycle [9].

Renewable energy sources appear to offer a solution to the global energy and climate crisis. However, there are still challenges to overcome before they can be widely integrated into the energy landscape. For example, the technologies used to utilize biomass and the installation of the necessary systems depend on local conditions, which include both physical and socio-economic factors. In many regions, biomass production costs are estimated to be between $1.5 and $2 per gigajoule. The implementation of improved and optimized production systems, coupled with a gradual transition towards biomass and multifunctional land use, has the potential to reduce the costs associated with biomass use to levels comparable to those of coal [9]. On a global scale, solar energy appears to be the most promising method of meeting the world's energy needs. With recent advances in photovoltaic technology, solar power plants are now being built in almost every region of the world. However, considering the annual sunshine duration of countries and the efficiency of existing solar cells, it seems unlikely that solar energy alone will be able to meet the world's energy needs in the near future [10, 11]. In light of these considerations, it becomes imperative to identify novel energy sources that can meet humanity's current energy needs. Hydrogen is one of the potential alternative sources capable of fulfilling this requirement.

2.1. Hydrogen

Hydrogen is the most abundant element in the universe. On Earth, however, it is mainly found in its bonded state with oxygen in water and in the structure of various compounds, including hydrocarbons. In its gaseous molecular form (H_2), it is non-toxic, tasteless, odorless and colorless [12–14]. Hydrogen has the highest energy gain per electron among the chemical elements. This is due to the fact that it contains the highest number of valence electrons per proton of any element in the periodic table [15]. Compared to fossil fuels, the gravimetric energy density of hydrogen (120 $MJ.kg^{-1}$) is about three times higher than that of natural gas (46.6 $MJ.kg^{-1}$) [16]. Combustion of hydrogen releases only water, making hydrogen an energy source that can be regenerated from its own combustion product [14]. Another characteristic of hydrogen as an

alternative energy source is its versatility in production. It can be produced by a variety of methods, further enhancing its potential as a viable alternative to the fossil fuels currently in use. Global hydrogen production currently stands at 50 billion tons per year. Of the total hydrogen produced, 49% comes from methane recovery, 9% from oil oxidation, 18% from coal gasification and 4% from water electrolysis [17]. In addition, other alternative energy sources have the potential to be used in the production of hydrogen in a variety of potential scenarios. For example, electricity from wind power facilitates the production of hydrogen by hydrolysis of water. It has been shown that hydrolysis of one cubic meter of water can yield 108.7 kilograms of hydrogen, which is comparable to the energy content of 422 liters of gasoline [18]. Hydrogen has a considerably wider range of flammability than other fuels. The combination of up to 4% hydrogen by volume with air results in a flammable mixture. As a result, hydrogen engines can operate more efficiently than their petrol counterparts [19]. Based on the above evidence, it can be argued that hydrogen is a viable alternative to fossil fuels. Unlike its traditional counterparts, hydrogen is not harmful to the environment and has the potential to meet the world's energy needs as a clean and renewable energy source.

With the growing concern of climate change and the depletion of oil and global gas reserves, it has become increasingly important to promote the use of environmentally sustainable energy sources for transportation and other applications. The use of hydrogen (H_2) as an energy carrier in fuel cell vehicles has the potential to revolutionize the transport sector, provided that the issue of efficient storage is adequately addressed. Currently, the storage systems used in commercial fuel cell electric vehicles use hydrogen storage tanks compressed at 700 bar. The aim is to develop efficient and safe hydrogen storage systems with a storage capacity of 5.5 wt% to achieve a range of over 500 km [20].

2.2. Storage of Hydrogen

Hydrogen storage methods are classified as physical methods, chemical methods and hybrid methods [21]. Physical methods include the use of high-pressure gas cylinders and cryogenic tanks to store hydrogen in liquid form. The chemical methods include the absorption of hydrogen in cracks in host metals, complex compounds, and the coexistence of metals and compounds with water. Finally, hybrid methods include adsorption of hydrogen in porous materials at cryogenic temperatures. Hydrogen storage can be either

reversible or irreversible. Reversible storage refers to the phenomenon whereby hydrogen is released from the stored material in proportion to the increase in temperature [22].

2.2.1. Storage in cryogenic tanks

Storage of hydrogen in the liquid state at low temperatures is a widely used method. Liquid hydrogen is stored in cryogenic tanks at 21.2 Kelvin and ambient pressure. Due to its critical temperature of 33 K, hydrogen can only be stored as a liquid in open systems. The volumetric energy density of hydrogen in its liquid state is 2.3 $kWh.L^{-1}$ [15]. The efficient realization of the liquefaction process in the cryogenic storage of hydrogen is a major challenge to be overcome. It is estimated that 30-40% of the energy stored by this method must already be consumed in the liquefaction process. In addition, the loss of hydrogen through evaporation, particularly in smaller tanks, is another significant problem. Thermal insulation of cryogenic tanks is another challenging aspect of this method [15, 16, 22].

2.2.2. Storage in high pressure cylinders

The use of high-pressure cylinders is a direct method of hydrogen storage. The most commonly utilized hydrogen cylinders can withstand pressures up to 20 MPa. However, when analyzed volumetrically, hydrogen has an energy density of only 0.8 $kWh.L^{-1}$ at a pressure of 35 MPa. In a separate study, the energy density of hydrogen stored at a pressure of 10,000 psi was found to be 4.4 $MJ.L^{-1}$, while the energy density of gasoline was found to be 31.6 $MJ.L^{-1}$ [22]. Accordingly, the energy density of hydrogen stored at high pressure is about one-seventh that of gasoline in the same volume. Another potential drawback of this approach is the lack of certainty regarding the safety of high-pressure cylinders. Commercially available tubes include those lined with aluminum and reinforced with carbon fiber. While aluminum-based tubes are easier to manufacture, carbon fiber tubes have superior durability compared to their aluminum counterparts. Conversely, the temperature of these materials must be kept below 85°C. However, the temperature can easily exceed this threshold as a result of gas compression during pressurized storage. It is therefore essential that filing systems are optimized as much as possible [16].

2.2.3. Storage in metal compounds

An alternative method of hydrogen storage is based on the utilization of host metals and metallic hydrates. The reaction of metals, intermetallic compounds and alloys with hydrogen typically results in the formation of solid metal-hydrogen structures. Consequently, MH_n (M=metal, n=1, 2, 3) structures are formed as a result of these reactions. In addition, hydrogen atoms can occupy tetrahedral and octahedral interstitial sites within the metal lattice. This process can be divided into two categories: reversible and irreversible. The reactions are reversible in terms of hydrogen storage and release. The metal-hydrites have storage capacities between 1.50-7.5 wt% [23]. In addition, dopant atoms play a significant role in the storage capacity of complex hydrates. The high energy storage capacity of hydrates per unit volume and the high reversible hydrogen storage capacity per mole of compound, the safe and explosion-free storage and the possibility to use the same storage units more than once make this method interesting [15, 16, 22]. However, despite these advantages, hydrate compounds have the potential to cause adverse effects on the environment and human health. For example, lithium hydrate (LiH) is corrosive, beryllium hydrate (BeH_2) is highly toxic, and diborane (B_2H_6) is classified as toxic in the literature [16]. In addition, a number of factors make the practical use of metal hydrate compounds in hydrogen storage a challenging endeavour. First and foremost, the recovery of hydrogen absorbed in metal hydrate compounds requires the storage tank to be heated to temperatures in exceeding 100 °C. This reduces the efficiency of the storage method in practice. In addition, the deterioration of the metal hydrate structure during re-use cycles and the toxic gases (ammonia, etc.) produced during the release of hydrogen from metal hydrates have the potential to damage fuel cells. Consequently, despite their apparent effectiveness as hydrogen storage media in terms of storage capacity, the practical use of metal hydrates for hydrogen storage remains unfeasible without the resolution of these issues [21].

2.2.4. Storage in porous solids

One of the most widely used techniques for hydrogen storage is the process of adsorption, where the gas is stored in channels and cavities within a porous material. Adsorption can be divided into two distinct categories: chemical adsorption and physical adsorption. Chemical adsorption is a consequence of the formation of chemical bonds

between the solid surface and the gas molecules. In this case, there is an exchange of electrons between the surface and the adsorbed molecule, resulting in a process that is typically irreversible. In contrast, physical adsorption is characterized by a weak interaction between the surface and the adsorbed gas molecule, typically due to van der Waals forces. Unlike chemical adsorption, physical adsorption is easily reversible. In other words, the removal of the adsorbed gas from the solid can be easily achieved by changing the temperature or pressure parameters. In contrast to chemical adsorption, the surface of the solid can accommodate more than one layer in physical adsorption [24, 25]. In addition to carbon-based materials such as activated carbon, fullerenes, single/multi-walled carbon nanotubes, graphene, metal-organic frameworks (MOFs), covalent organic frameworks (COFs), microporous metal coordination materials (MMOMs), and natural and synthetic zeolites are also used in this field.

In conclusion, a comparison of the various methods of hydrogen storage shows that the use of nanoporous adsorbents and metal hydrate-like compounds is a safer and more economical option than the use of high-pressure compressed vessels or cryogenic storage methods. The process of physical adsorption in nanoporous materials is characterized by rapid adsorption kinetics and reversibility. Therefore, physical adsorption is superior to metal hydrate type materials in terms of rapid adsorption and desorption of hydrogen. Furthermore, in terms of energy requirements, physical adsorption is more advantageous than metal hydrates and complex hydrates in that it can operate without the need for high temperatures during hydrogen recovery. In the context of mass hydrogen storage, compounds such as MgH_2 are more advantageous than physical adsorption in porous materials. In terms of safety, the storage of hydrogen in porous materials by physical adsorption is safer than in metal hydrates. This is due to the fact that there is no release of secondary toxic gases during recovery. For all of the aforementioned reasons, physical adsorption represents a highly effective option for hydrogen storage [13, 15, 21, 26].

2.3. Literature Survey and The Aim of the Thesis

A large number of studies dealing with hydrogen storage in porous materials can be found in the scientific literature (Appendix). For example, for zeolites, Zecchina et al. [27] reported a hydrogen adsorption capacity of 1.28 wt% for H-SSZ-13 at 77 K and up to 92 kPa. Similarly, Regli et al. [28] found that H-chabazite (Si/Al = 2.1), a chabazite-type zeolite from a different source, exhibited a hydrogen uptake of 1.10 wt% under the

same conditions. As reported by Erdoğan Alver and Sakızcı [29], the hydrogen adsorption capacity of Na-CHA was determined to be 1.08 wt% at 77 K and up to 100 kPa. In a similar study, Erdoğan and Dikmen [30] found that the acid-modified clinoptilolite (CLN) sample CLN-2N exhibited a hydrogen uptake of 0.48 wt% under the same conditions. Furthermore, Erdoğan Alver and Esenli [31] found that the sample M-3N retained 0.34 wt% H_2 at 77 K and up to 100 kPa. For zeolite-Y templated carbon and NaY samples, hydrogen retention capacities of 1.72 wt% (at 323 K) and 1.16 wt% (at 77 K) were reported by Wijiyati et al [32] and Raj et al [33], respectively. In a separate study, Fujiwara et al. [34] reported a hydrogen adsorption capacity of 0.006 wt% for synthetic zeolite ZSM-5-O at 77 K and 98 kPa. Tantawy and Ismail [35] found that nano-faujasite and nano-analcime zeolites retained 2.25 wt% and 0.74 wt% H_2 at 77 K under a high pressure of 2200 kPa. Bayrakdar Ateş [36] found that 0.2 M NaOH-modified CLN retained 26.47 $cm^3.g^{-1}$ of hydrogen at 77 K and 119.9 kPa, while Weitkamp et al. [37] found that sodalite retained 9.2 $cm^3.g^{-1}$ at 573 K and up to 10 MPa.

The majority of these studies focus on the hydrogen adsorption properties of CLN modified by direct treatment with salt or acid solutions. However, it is important to emphasize that these modification methods can have detrimental effects on the clinoptilolite (CLN) framework. For example, acid treatment, even at low molarities, can cause dealumination, leading to a rapid breakdown of the crystal structure. This structural collapse is evidenced by the appearance of a broad band in the X-ray diffraction (XRD) pattern, indicating the formation of amorphous SiO_2 [30]. An alternative approach to the structural modification of clinoptilolite is thermal treatment followed by ammonium (NH_4^+)ion exchange. In this process, the raw clinoptilolite is first treated with ammonium salt solutions and then calcined at temperatures between 400 and 600 °C. During calcination, the adsorbed ammonium ions thermally decompose, releasing ammonia (NH_3) and hydrogen ions (H^+). As a result, converting the material to its H^+ form after ammonium exchange provides several advantages: it facilitates the removal of exchangeable cations without compromising the integrity of the crystal structure, promotes structural homogenization, allows selective cation doping after treatment, and improves gas adsorption performance [31, 32].

ZIF-8 structures have also been studied in hydrogen storage research. Park et al. reported the H_2 adsorption capacity of ZIF-8 sample 3.1 wt% at 77 K and 55 bar [38]. Furthermore, H_2 adsorption capacity of ZIF-8 was found 3.3 wt% at 77 K and 30 bar and

0.13 wt% at ambient temperature and 60 bar [39]. Modified ZIF-8 structures have also been investigated by various researchers. For example, H_2O pre-treated ZIF-8 samples showed 0.23 wt% at 50 bar after ZIF-8 [40]. The Mg decorated ZIF-8 nanoparticles were observed to have a hydrogen storage density of 5.3 wt% [41]. In another study, Pd decorated ZIF-8 samples exhibited 30% higher hydrogen storage capacity than pristine ZIF-8 [42]. On the other hand, Bose et al. find that pristine ZIF-8 sample has 3.13 wt% hydrogen storage capacity at 77 K and 50 bar [43]. In another study, ZIF-8 pellets showed hydrogen adsorption capacities of 2.64-2.82 wt% at 25 bar and 77 K [44].

A review of the literature shows that the hydrogen storage properties of porous silicon (Si) nanostructures have been extensively investigated [45–51]. For example, Si nanoparticles were reported to have a hydrogen storage capacity of 2.25 wt% at a pressure of 9.87 bar and a temperature of 120 °C [48]. In a more recent study, ball-milled porous Si showed a hydrogen uptake of 10.7 wt% under conditions of 120 °C and 80 bar [46]. Similarly, Muduli et al. reported that porous Si films prepared by electrochemical anodization of bulk Si and subsequently stripped from the Si wafer by electropolishing achieved a storage capacity of approximately 0.101 wt% at 120 °C and 20 bar [50]. In addition to pure porous Si structures, various hybrid and surface modified Si-based materials have also been investigated for their hydrogen storage capabilities. For example, Li-dispersed silica nanotubes exhibited storage capacities of 0.15 wt% and 0.29 wt% at 77 K under 4.5 MPa [52]. A porous Si nanowire–LiH (SiNWs–LiH) alloy demonstrated a higher uptake of 3.95 wt% at around 4 MPa and 400 °C (673 K) [49]. Furthermore, a hybrid material composed of nanoporous Si and single-walled carbon nanotubes showed a hydrogen storage capacity of 0.0793 $mmol \cdot g^{-1}$ [53].

In summary, these results indicate that the CLN, porous SiNWs, and ZIF-8 materials are promising candidates for hydrogen storage applications, especially under high pressure and elevated temperature conditions, with the potential to meet the US Department of Energy (US DOE) goals [47].

However, the lack of these materials is they are not cost-effective and not feasible for daily life applications. Furthermore, the applicability of zeolites in H_2 storage applications can be possible, if the microporosity and cation homogeneity of these materials can be improved. Also, the Si based nanowires in hydrogen storage technologies is relatively new materials and there is a gap in the literature about their storage

performance via physisorption. On the other hand, ZIF-8 is a well-know porous material in the field of H_2 storage, but its modified forms are rarely investigated.

For the reasons explained previously, this thesis is divided into three distinct parts, each investigating a different material. Firstly, the effect of doping with Na^+, K^+, Ag^+, Li^+, Ni^{2+}, Cu^{2+}, Ca^{2+} and Mg^{2+} cations after ammonium nitrate pre-treatment on the textural and hydrogen adsorption properties of clinoptilolite was investigated, where the H^+ form is obtained without damaging the crystal structure. This method has the potential to improve the microporosity of CLN without damaging its crystal structure. Secondly, pristine ZIF-8 material was synthesized for use as a reference material. Furthermore, the effect of in situ doping with Na and Li ions on the porosity and hydrogen adsorption capacities of ZIF-8 was investigated. It is expected that these modifications will improve the H_2 adsorption capacity of ZIF-8. Finally, the hydrogen adsorption-desorption behavior of silicon-based porous materials and their surface-functionalized derivatives at cryogenic temperatures and atmospheric pressure remains largely unexplored in the current literature. Accordingly, the novel aspect of the third part of this work is the investigation of the molecular hydrogen physisorption properties of Au- and Li-functionalised porous SiNWs.

With the findings of this thesis:

- The H_2 storage properties of natural CLNs will be better understood.
- The effect of in situ modification with monovalent cations on the porosity and H_2 storage properties of ZIF-8 will also be explored.
- To the best of our knowledge, this will be the first demonstration of the hydrogen storage properties of porous SiNWs via physisorption at 77 K and up to 113 kPa of pressure.

3. THEORETICAL BACKGROUND

Porous materials have been used in adsorption applications since ancient times. It is an established fact that materials such as clay, charcoal and sand have been used to desalinate water, cure diseases and clarify oil. However, systematic studies did actually begin after the 1750s. It is an established fact that the principles that govern the adsorption process were discovered in the first quarter of the 20th century [54]. Adsorption is vital for industrial applications, including gas purification and separation [55–57] and the removal of heavy metals and radioactive nuclei from drinking water [58–61]. Researches are being actively conducted into the storage of gases in porous solids like hydrogen or ammonia via the adsorption process [62–68] This section describes adsorption phenomena. Additionally, the physical principles underlying the chosen characterization methods will be presented.

3.1. Adsorption Phenomena

Atoms or molecules attach to an interface (which can be the surface of a solid or liquid bulk material) when there is a strong interaction energy between the interface and the atoms/ molecules. This process is called adsorption. The adsorption process is dependent on the physical and chemical properties of the interface and the atoms/ molecules that interact with it. In this thesis, adsorption phenomena will be discussed only in the context of interactions between solid surfaces and gas molecules. As shown in Figure 3.1., when gases adsorb on solids, the solid surface is known as the adsorbent. The fluid in the adsorbed state is called the adsorbate, while the gas that has not yet been adsorbed is known as the adsorptive [25, 69].

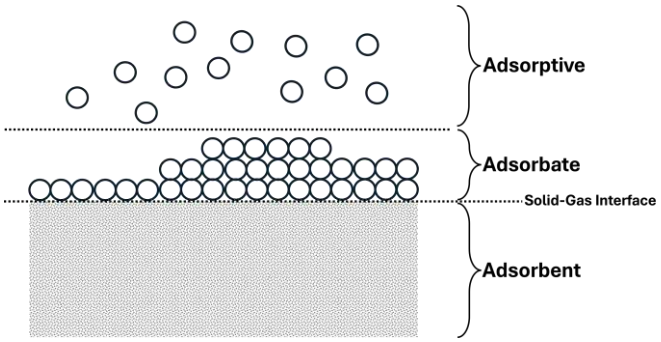

Figure 3.1. *Schematic representation of adsorption process*

The two types of adsorptions were determined in the literature according to strength of interaction: **Chemical adsorption (or chemisorption)** is governed by high interaction potentials and is irreversible. The **physical adsorption (or physisorption)** is reversible, and is ruled by relatively weak interaction potentials [25]. Table 3.1 clearly outlines the main properties and distinguishing features of these two types of adsorptions.

Table 3.1. *Properties of physical and chemical adsorption [25]*

The Type of Adsorption	Physical	Chemical
	Low interaction energies	High interaction energies
	Van der Waals' forces	Chemical interactions
	Reversible	Irreversible
	High adsorption kinetics	Low adsorption kinetics
	Localized	Not localized
	Can be multilayer	Only monolayer

Physical adsorption occurs via Van der Waals' forces, including ion-dipole, dipole-dipole, ion-induced dipole, quadrupole interactions and dispersion forces. These interactions are weak between adsorbent and adsorbate. From now on, the term "adsorption" will be used to describe only the physical adsorption that takes place on the solid-gas surface, unless otherwise specified. Adsorption of gases on solid surfaces is always exothermic. Adsorption decreases Gibbs free energy and the degrees of freedom of gas atoms/ molecules (due to restricted movement of particles in 2D). The entropy of the adsorbed gas therefore also decreases. Therefore, according to Eq. 3.1, ΔH has to be negative. It is clear that the adsorption process must be exothermic [25].

$$\Delta G = \Delta H - T\Delta S \tag{3.1}$$

3.2. Classification of Pore Size

The International Union of Pure and Applied Chemistry (IUPAC) states that pores of solids can be classified according to their internal width [70].

i . A pore has an internal width of less than 2 nm is known as a micropore.

ii. A pore has internal width between 2 and 50 nm and is defined as mesopore.

iii. A pore with an internal width of more than 50 nm is called a macropore.

It is clear from the most recent literature that micropores with an internal width between 2 and 0.7 nm are defined as super-micropores, and those with an internal width below 0.7 nm are defined as ultra-micropores [71].

3.2.1. Adsorption potential

The adsorption behaviour of molecules is determined by a number of factors. These include intermolecular (fluid-fluid) interactions between adsorbate molecules and fluid-surface interactions. The latter depend on the adsorption potential (fluid-wall attraction) of the surface. The macropores are too wide to display different interactions with flat surfaces (Figure 3.2.a). In mesopores, adsorption is influenced by fluid wall attraction and fluid-fluid interactions (Figure 3.2.b). It is clear that gas molecules condense to a liquid-like phase in mesopores under the value of saturation pressure (P_0) due to fluid-fluid interactions. This is known as capillary condensation (pore condensation). It is clear that the adsorption behaviour of the adsorbent molecules is almost entirely determined by fluid-wall interactions in micropores. In fact, the adsorption potentials of the pore surfaces overlap in micropores. It is clear that the pore walls are very close together (Figure 3.2.c) [25].

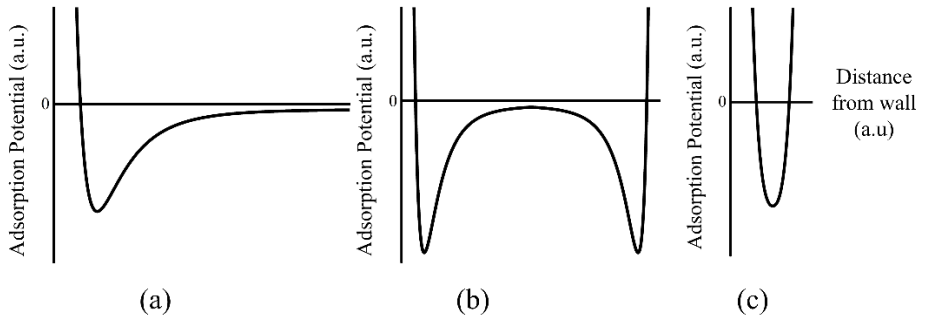

Figure 3.2. *Adsorption potentials in different pores. (a): macropore, (b): mesopore, (c): micropore*

3.3. Adsorption Isotherms

An adsorption isotherm represents the relationship between the amount of adsorbed gas and its pressure under constant temperature [69]. IUPAC clearly states that there are six types of adsorption isotherms (Figure 3.3) [70]. In physical adsorption, sorption

and high uptakes are clearly observed at relatively low pressures, due to the narrow pore width and high adsorption potential. Type-II sorption isotherms are obtained for non-porous or macroporous adsorbents. These isotherms show unrestricted monolayer-multilayer adsorption. The inflection point, or knee, of the isotherm is point B. This point marks the point at which monolayer coverage is complete and multilayer adsorption begins.

The reversible Type-III isotherm is convex with regard to the P/P_0 axis over its entire range and thus point B is not exhibited. This indicates that the attractive adsorbate-adsorbent interactions are relatively weak and that the adsorbate-adsorbate interactions play an important role. Type-IV isotherms are a common feature of mesoporous materials. The most characteristic feature of the Type-IV isotherm is the hysteresis loop, which is associated with the occurrence of pore condensation. The initial part of the Type IV curve can be attributed to monolayer-multilayer adsorption, as with the Type II isotherm. Type-V isotherms show clear evidence of pore condensation and hysteresis. The initial part of this sorption isotherm is clearly related to the adsorption isotherms of Type-III. This indicates relatively weak attractive interactions between the adsorbent and the adsorbate. The Type-VI isotherm is a special case. It represents stepwise multilayer adsorption on a uniform, non-porous surface [25].

The shape of both the adsorption isotherm and the hysteresis loop provides definitive information about the pore structures of solids. According to IUPAC, four types of hysteresis shape can be obtained in adsorption isotherms. (Figure 3.4) Type H1 is associated with porous materials consisting of well-defined cylindrical-like pore channels. Materials that give rise to H2 hysteresis are often disordered, and the distribution of pore size and shape is not well defined. Isotherms revealing type H3 hysteresis do not exhibit any limiting adsorption at high P/Po. This is in contrast to non-rigid aggregates of plate-like particles giving rise to slit-shaped pores. Type H4 hysteresis loops are associated with narrow slit pores and now include pores in the micropore region. Hysteresis loops always display an open or closed shape, depending on the porous material.

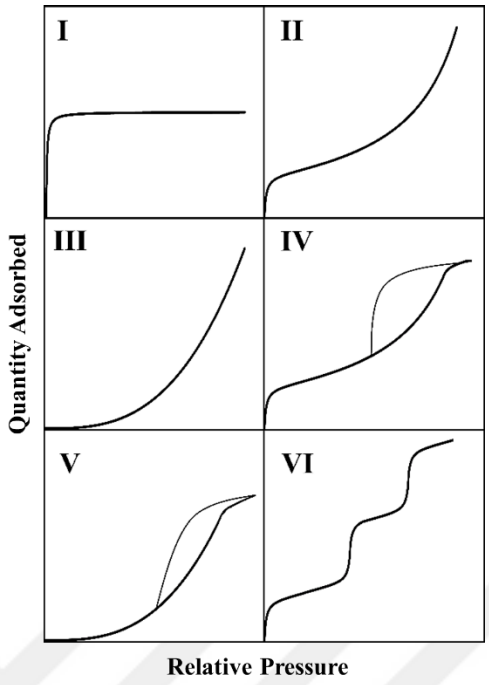

Figure 3.3. *Adsorption isotherms according to IUPAC classification (Dashed lines represent open hysteresis loops) [54]*

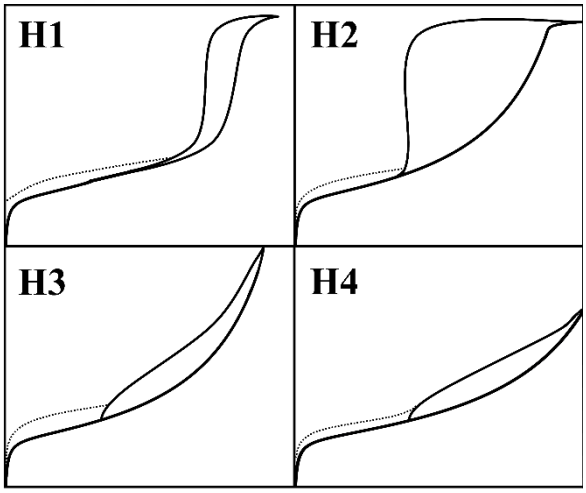

Figure 3.4. *Hysteresis loops according to IUPAC classification (Dashed lines represent open hysteresis loops) [54]*

3.4. Theories of Adsorption

3.4.1. Langmuir theory

Theoretical studies on adsorption began in the early 20th century. The first model was proposed by Langmuir in 1918 [72]. This theory is based on assumptions given below [73]:

i. The surface of the solid is homogeneous and flat.
ii. The adsorbate is an ideal gas and is not a mixture of different species.
iii. The adsorbent and the adsorbate are in equilibrium.

Under these assumptions, Langmuir equation can be presented as follows:

$$\frac{P}{V} = \frac{1}{KV_m} + \frac{P}{V_m} \tag{3.2}$$

Langmuir theory is the definitive description of monolayer adsorption and Type-I isotherms. However, it fails to treat Type-II and Type-IV isotherms, which are related to physical adsorption. This problem needs a more generalized theory to be solved.

3.4.2. The Brunauer, Emmett and Teller (BET) theory

During the physical adsorption process, more than one layer of gas molecules can cover the surface of the adsorbent. The BET theory successfully extends Langmuir's theory to multilayer adsorption. The BET equation is derived through the equilibration of the rates of adsorbate evaporation and condensation across the various adsorbed molecular layers. This derivation is based on the assumption that a characteristic enthalpy of adsorption, ΔH_1, applies to the initial monolayer, and that the enthalpy of liquefaction, ΔH_{liq} is relevant to adsorption within the second and subsequent layers [25, 69]. The BET equation is given below:

$$\frac{P}{V(P_0 - P)} = \frac{1}{V_m C} + \frac{(C-1)}{V_m C}\frac{P}{P_0} \tag{3.3}$$

In his equation, "V_m" represents monolayer capacity and "C" is a constant which equals to

$$C = \exp\left[\frac{\Delta H_{liq} - \Delta H_1}{RT}\right] \tag{3.4}$$

Once the V_m is determined from the isotherms, the surface area can be calculated with

$$\sigma = \frac{V_m S_0 N_A}{22400} \tag{3.5}$$

In Eq. 3.5 "σ" corresponds to total surface area, "S_0" represent the cross-sectional surface area of adsorbed gas molecule and N_A is Avogadro's number.

The BET equation fits many experimental isotherms well, especially those with a pressure range of 0.05-0.35 P/P_0. BET theory must be applied with caution when using microporous materials. The Rouquerol criteria definitively enhance the validity of surface area values calculated with BET theory [74].

3.5. Characterization Methods

3.5.1. X-Ray diffraction

Since X-Rays were discovered by Röntgen in 1895 and their diffraction was explained by Laue, Friedrich and Knipping in 1912, X-Ray Diffraction (XRD) has been the main technique used to examine crystal structures. This technique is mainly based on studies of Bragg's [75]. Bragg explains that crystal planes act as a reflective surface for X-rays. Intense reflected beams are generated when the path length difference between reflections originating from consecutive crystallographic planes within a set is equivalent to an integer multiple of the incident radiation's wavelength [76]. Bragg's law is expressed mathematically as follows:

$$n\lambda = 2d_{hkl} \sin\theta \tag{3.6}$$

where λ is the wavelength of the incident X-ray, n is the order of reflection, d_{hkl} is the spacing between planes of crystal with corresponding Miller indices hkl and θ is the angle between incident or reflected beams of X-ray and crystal planes [76]. Geometrical representation of Bragg's law is given in Figure 3.5 (a).

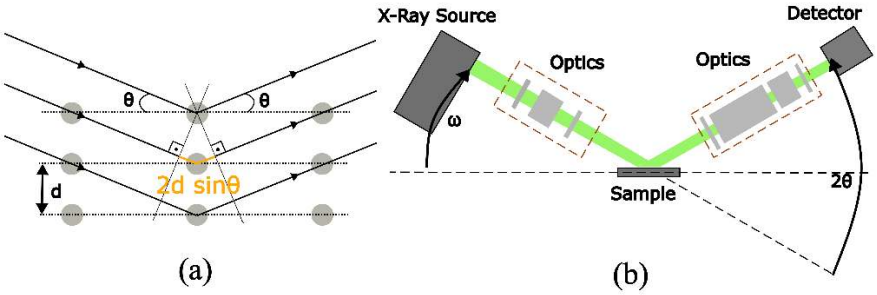

Figure 3.5. *Schematic representation of (a): Bragg's law and (b): X-Ray Diffractometer [77]*

Thermionic emission is the foundational principle in the generation of X-rays within the X-ray Diffractometer source. The process starts with the heating of a filament, usually made of tungsten. When the thermal energy threshold is surpassed, electrons are ejected from the filament's surface. Subsequent to emission, these electrons are subjected to a high potential difference, often on the order of tens to hundreds of kilovolts, established between the filament (cathode) and a target material (anode). The anode is typically crafted from a material with a high atomic number, such as copper. Upon impact with the anode, the high-speed electrons undergo rapid deceleration. This abrupt deceleration results in the form of X-rays. The X-ray spectrum is made up of two components: bremsstrahlung radiation (also known as braking radiation) and characteristic X-rays. Bremsstrahlung is produced when electrons decelerate as they interact with the electric field of the anode nuclei, yielding a continuous spectrum of X-ray energies. Characteristic X-rays are emitted when incident electrons eject inner-shell electrons of the anode atoms. Subsequent electronic transitions to fill these vacancies result in the emission of photons with discrete, energy-specific wavelengths characteristic of the anode material. It is clear that the intensity and energy spectrum of the produced X-rays are primarily governed by the accelerating voltage and the current of the electron beam [76, 77].

3.5.2. X-Ray fluorescence spectroscopy

X-ray fluorescence (XRF) spectroscopy is the analytical technique of choice for determining the elemental composition of a wide range of materials. The fundamental principle underlying XRF is the phenomenon of secondary (or fluorescent) X-ray emission following the excitation of a sample by a primary X-ray source. This non-destructive method is based on the unique atomic structure of each element, which determines the energy of the emitted fluorescent X-rays. The analytical process in XRF is initiated by irradiating the sample with a high-energy X-ray beam. These primary X-rays have enough energy to dislodge inner-shell electrons (e.g. K or L shell electrons) and create electron vacancies. The ionization process makes the atom energetically unstable. At the same time, an electron from a higher-energy outer shell transitions to fill the inner-shell vacancy. This electronic transition is accompanied by the characteristic fluorescent X-ray. The energy of this emitted fluorescent X-ray is precisely equal to the energy difference between the electron shells involved in the transition. Energy differences are unique to each element. Detecting and measuring the energies (or wavelengths) of the emitted X-rays creates a 'fingerprint' that identifies the constituent elements in the sample. The intensity of the fluorescent X-ray at a specific energy is directly proportional to the concentration of the corresponding element in the sample. This enables quantitative analysis [78, 79].

3.5.3. Fourier transform infrared spectroscopy

Fourier transform infrared (FT-IR) spectroscopy is the analytical technique used to identify and quantify chemical bonds and functional groups within a sample. The resulting raw data, known as an interferogram, is then subjected to Fourier transformation to yield the familiar infrared spectrum, which plots absorbance or transmittance as a function of wavenumber or wavelength. The fundamental principle of FT-IR spectroscopy is the interaction of IR radiation with the vibrational modes of molecules. Different functional groups (e.g. Si-O, O-H, C-H) exhibit characteristic vibrational frequencies. These fall within specific regions of the infrared spectrum (typically 4000 to 400 cm^{-1}). However, homonuclear molecules (N_2, O_2, etc.) and symmetric molecules like CCl_4 do not interfere with the IR radiation since there is no dipole moment chance during their vibrational modes [80].

The Michelson interferometer is the core component of an FT-IR spectrometer (Figure 3.6.). This optical device is made up of a beam splitter, a fixed mirror, and a moving mirror. The infrared beam from the source is split into two paths by the beam splitter. One beam is reflected off the fixed mirror, and the other is reflected off the moving mirror. These two beams are then recombined, creating an interference pattern that varies as the position of the moving mirror changes. This variation in interference as a function of the moving mirror's position is the interferogram. The interferogram contains all the information about the infrared frequencies absorbed by the sample. The individual frequencies and their corresponding intensities are extracted using a mathematical algorithm called the Fourier transform on the interferogram. This transformation converts the time-domain interferogram into a frequency-domain spectrum, revealing the characteristic absorption bands of the sample's constituent molecules.

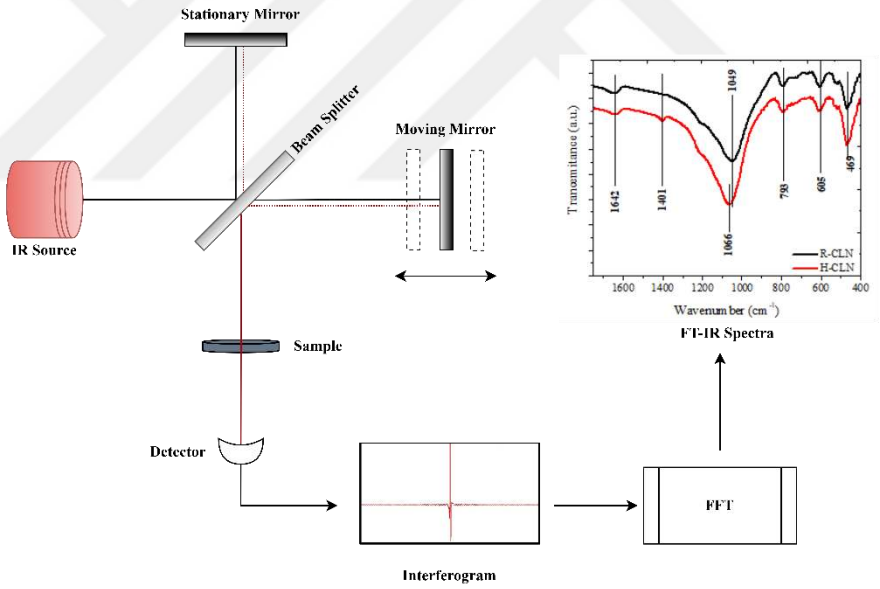

Figure 3.6. *Schematic representation of FT-IR spectroscopy*

The preparation of samples for FT-IR analysis varies depending on the nature of the sample. Solids can be analyzed as powders mixed with an inert matrix (e.g. KBr) and pressed into a pellet, as thin films. The resulting infrared spectrum definitively identifies the functional groups in the sample. The intensity of the absorption bands is directly proportional to the concentration of the corresponding functional groups, enabling

quantitative analysis. The shape and width of the bands definitively provide insights into the sample's environment and physical state.

3.5.4. Scanning electron microscopy and energy dispersive X-ray spectroscopy

Scanning electron microscopy (SEM) is the best technique for examining materials' morphology. This technique uses a focused beam of electrons accelerated under high voltages (up to 30 kV) [81]. When the accelerated electron beam interacts with the sample, different interactions occur between the electrons and the atoms of the specimen (Figure 3.7):

- Electrons can interact with the nuclei of the atom and are scattered with low angles or with high angles (Back-scattered electrons (BSE)).
- Electrons can interact with another electron of the atom and produce secondary electron (SE),
- Electrons can interact with another electron of the atom and produce secondary electrons and characteristic X-rays [82].

The BSE electrons provide definitive information about the composition, topography, mass thickness and crystallography of the sample. SE images are useful for obtaining topographic contrast [83].

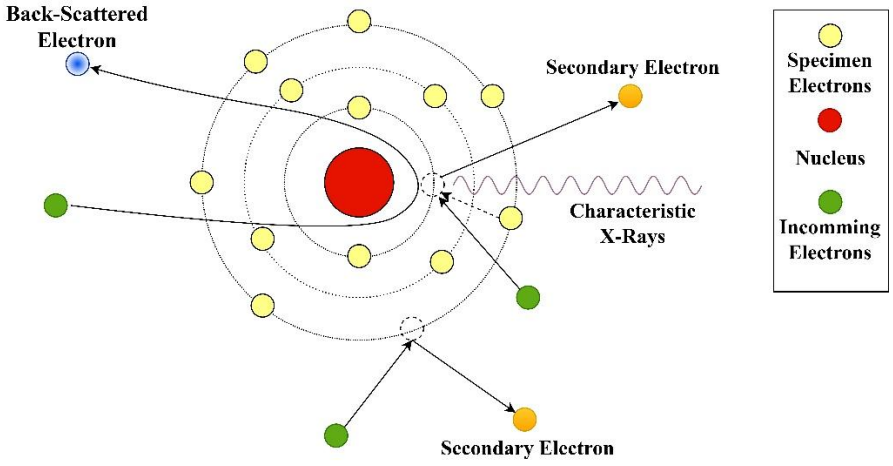

Figure 3.7. *Schematic representation of electron-atom interactions*

The characteristic X-Rays produced during electron-atom interactions can be used for elemental analysis of the samples. This technique is called Energy Dispersive X-Ray Spectroscopy (EDS). EDS can be used to determine the elemental composition of the specimen quantitatively and qualitatively, just same as XRF measurements [83].

3.5.5. Volumetric adsorption analysis

The volumetric (manometric) method is the most widely adopted technique for gas adsorption characterization. This technique allows us to indirectly determine the amount of gas adsorbed by a solid material under defined temperature and pressure conditions by monitoring pressure changes within a closed system. Volumetric analysis is the most effective way to evaluate the specific surface area, pore size distribution in microporous and mesoporous materials, and the physisorption-based gas storage capacities of adsorbates such as hydrogen, nitrogen, etc. The technique is based on the ideal gas law, or its corrected form for real gas behaviour. It is essential that all volumetric components of the apparatus are precisely calibrated prior to measurement. This includes the reference reservoir, sample cell and connecting lines (Figure 3.8).

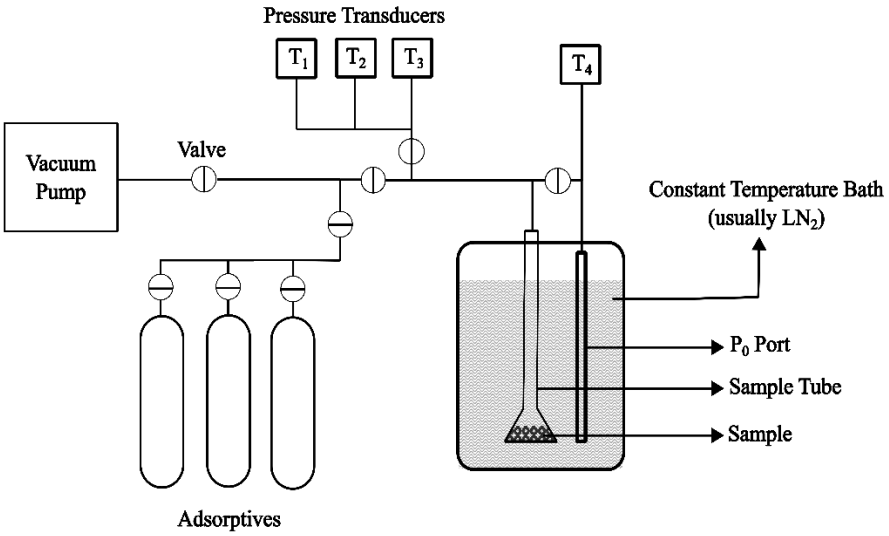

Figure 3.8. *Schematic representation of volumetric adsorption apparatus*

Sample preparation is a critical step that significantly affects the accuracy of adsorption data. The sample is placed in a dedicated cell and subjected to a degassing (activation) procedure under vacuum, typically within a temperature range of 100–300°C. This process removes any pre-adsorbed species such as moisture or residual gases. The

complete removal of surface-bound contaminants is essential for obtaining reliable adsorption isotherms.Following activation, the measurement phase begins with the introduction of a known amount of adsorbate gas into the reference reservoir, where it is pressurised to a predetermined value. The total amount of gas is calculated based on the known volume and pressure of the reservoir. The gas then expands into the sample cell, where some of it is adsorbed onto the material's surface, with the rest remaining in the free volume. Once equilibrium is reached, the amount of gas adsorbed is determined from the pressure drop between the initial and final states. This dosing process is repeated with incremental pressure steps to construct a complete adsorption isotherm. Optionally, a desorption isotherm may also be obtained by sequentially withdrawing the gas, allowing for analysis of hysteresis and adsorption reversibility. Measurements are conducted under isothermal conditions; cryogenic temperatures (e.g., 77 K for nitrogen) are maintained using liquid nitrogen bath. The experimental data are analyzed using established models. Surface area is typically calculated via the Brunauer–Emmett–Teller (BET) method, while pore size distribution is evaluated using techniques such as Barrett–Joyner–Halenda (BJH) or Density Functional Theory (DFT), depending on the pore structure and measurement range [25, 84, 85].

4. MATERIALS

4.1. Zeolites

Zeolites are aluminosilicate minerals that have been recognized for nearly three centuries. The first documented instance of natural zeolites was in 1756, when the Swedish mineralogist Fredrich Crostedt discovered these crystals and designated them zeolites, which means boiling rock in Greek (ζέω (zéō), meaning "to boil" and λίθος (líthos), meaning "stone) due to their propensity to expel water when heated, thereby giving the appearance of boiling [86, 87]. These minerals are commonly found in nature. These mineral deposits are characteristically formed as fine crystals of hydrothermal origin within geodes and fissures of eruptive rocks. Alternatively, they can occur as microcrystalline masses of sedimentary origin, thereby demonstrating the versatility of their formation environments [86]. The crystalline framework of zeolites consists of tetrahedral units with a general formula of TO_4, where T represents silicon (Si) or aluminum (Al), and O denotes oxygen. These tetrahedral units combine to form three-dimensional networks with cavities, channels, and exchangeable cations such as Na^+, Mg^{2+}, and Ca^{2+}. The replacement of trivalent cations (e.g. Al^{3+} or Ga^{3+}) with zeolite frameworks introduces a negative charge, which is balanced by these exchangeable cations. Depending on their structural arrangement, zeolites have the capacity to exhibit either two-dimensional (2D) or three-dimensional (3D) channel networks. These networks contribute to the porosity and adsorption properties of the material [86, 88].

These minerals occur in their natural state and as the result of synthetic production. To date, approximately 45 types of natural zeolites (among a total of 258 framework types) have been identified, exhibiting a diverse array of chemical and crystallographic properties [89]. The identification and classification of different framework types remains an active area of research. For instance, during the composition of this thesis, the International Zeolite Association (IZA) Structure Commission approved two novel framework type codes (HZF and ZJN) [90–92].

4.1.1. Clinoptilolite

Clinoptilolite, a naturally occurring zeolite, is classified within the heulandite (HEU) framework family. The generalized chemical formula for clinoptilolite is expressed as $(Na,K)_6(Al_6Si_{30}O_{72})\cdot 20H_2O$. The primitive cell parameters are thus

determined as a = 17.62 Å, b = 17.91 Å, c = 7.39 Å, and β = 116°16'. Its framework structure, exhibiting monoclinic $C_{2/m}$ symmetry, bears a close structural resemblance to that of heulandite [86]. However, clinoptilolite demonstrates superior structural stability compared to heulandite at elevated temperatures. Consequently, Mumpton defined clinoptilolite as a zeolite that is capable of withstanding overnight heating at 450 °C [93].

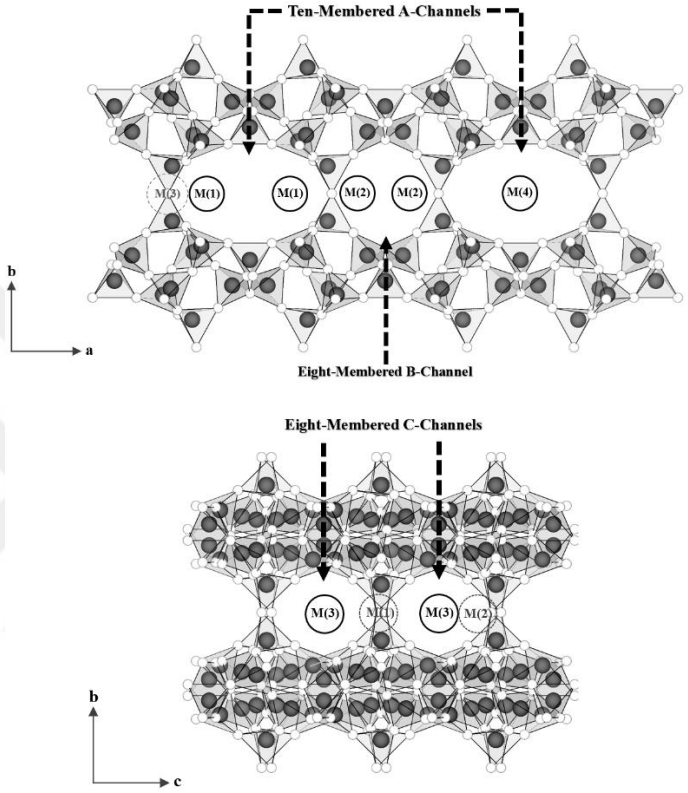

Figure 4.1. *Framework structure and cation locations of CLN along c-axis and a-axis, respectively [94]*

Clinoptilolite is characterized by a two-dimensional channel system, comprising three distinct channels (Figure 4.1). It is evident that channels A and B are aligned along the c-axis, while channel C intersects these channels along the a-axis. It is noteworthy that the structure is lacking a channel along the b-axis, thereby restricting matter transfer within clinoptilolite to the a- and c-axes. Channel A represents the largest tunnel, delineated by a 10-membered ring within the clinoptilolite structure. In comparison, channels B and C, which consist of 8-membered rings, are comparatively smaller than channel A [86, 95]. Clinoptilolite is characterized by the presence of four cation sites within the designated channels, designated as M(1), M(2), M(3), and M(4) (Figure 1). The M(1) site is located within channel A, typically occupied by Na^+ and Ca^{2+} cations.

The M(4) site, positioned at the center of channel A, accommodates the Mg^{2+} cation coordinated with water molecules. The M(2) site, situated within channel B, is predominantly occupied by Ca^{2+}, whereas the M(3) site, located at the center of channel C, is occupied by K^{+} ions. Furthermore, studies have indicated the potential for clinoptilolite to host other cation positions, including Cs^{+}, Ag^{+}, Pb^{2+}, Cd^{2+}, and Hg^{2+} ions [57, 96–98]. In addition to the cations previously mentioned, alternative cations, including Li^{+}, Ag^{+}, and Ni^{2+}, have been observed to occupy distinct sites within the clinoptilolite structure. As demonstrated by Dimova et al., for instance, Ag^{+} cations have been shown to be present at both the M(1) and M(2) sites [99]. However, a supplementary site within the A channel, in close proximity to the intersection of channels A, B, and C, has also been identified as a potential location for Ag^{+} cations. In contrast, Li^{+} ions have been documented to reside at the M(4) site [98]. The precise localization of Ni^{2+} and Cu^{2+} cations within the channel system remains ambiguous. One study posits that the positional distribution of Ni^{2+} is contingent upon the initial cation composition of the starting material. Specifically, Ni^{2+} cations occupy the M(1) and M(2) sites in Na- and K-rich clinoptilolites (CLNs), whereas they are found at the M(3) site in Mg- and Ca-rich CLNs [100]. Furthermore, Armbruster et al. identified four potential cation sites for Cu^{2+} ions, corresponding to the M(1), M(2), and M(4) sites, alongside a novel site located above and below the M(4) site, with respective occupancy factors of 0.056, 0.392, 0.71, and 0.052 [101]. In contrast, Garcia-Basabe and colleagues investigated the occupancy of the Ni^{2+} site in protonated and dealuminated forms of clinoptilolite (CLN). The CLN samples were obtained through calcination following ammonium exchange and stepwise HCl treatment, respectively. Their findings indicate that, in the protonated form of CLN, Ni^{2+} cations may be localized at the M(4) site and near the channel B window. For Cu^{2+}, localization at the M(1) and M(4) sites was observed, with distances of 1.45 and 1.65 Å, respectively [102]. Due to its structural attributes, clinoptilolite finds applications in gas separation and the removal of toxic gases [103–106].

4.2. Zeolitic Imidazolate Frameworks

Zeolitic Imidazolate Frameworks (ZIFs) represent a subset within the broader category of Metal-Organic Frameworks (MOFs). ZIFs are distinguished by their three-dimensional, porous crystalline architecture, characterized by a tetrahedral topology that shares structural analogies with zeolites [107]. These frameworks are constituted by

transition metal (M) atoms, which are coordinatively bonded to nitrogen atoms from imidazolate (Im) ligands (Figure 4.2). Notably, the M–Im–M bond angle within ZIFs approximates 145°, a value that closely aligns with the Si–O–Si bond angle observed in zeolites [108].

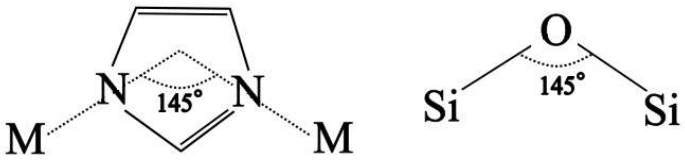

Figure 4.2. *Comparison of ZIF and Zeolite basic building blocks.*

Among the diverse array of ZIF variants, ZIF-8, synthesized via the coordination of zinc ions with 2-methylimidazole (mIm), adopts a sodalite (SOD) topology (Figure 4.3), characterized by the presence of four- and six-membered ZnN_4 rings [39]. ZIF-8 exhibits notable attributes, including exceptional thermal and chemical stability, a high specific surface area, and tunable porosity [43, 44]. Additionally, the ZIF-8 framework exhibits flexibility. It is evident that the geometry and pore size of the ZIF-8 framework are capable of variation when influenced by external factors such as pressure or molecule adsorption [109]. The 'swing effect' is a pertinent exemplification of this phenomenon. The width of the pore-connecting windows has been observed to expand from approximately 3.4 Å to approximately 4.2 Å upon the adsorption of molecules [110]. The synthesis of ZIF-8 can be accomplished through a variety of methodologies, encompassing solvothermal [38, 111, 112], sonochemical [113, 114], mechanochemical [115, 116] and microwave-assisted techniques [117–119].

ZIF-8 has a variety of applications, including gas storage [120, 121], CO_2 capture [122], heat storage [123], electrochemical sensors [124], wastewater treatment [125], biomedical applications [126, 127] and hydrogen storage [41, 42].

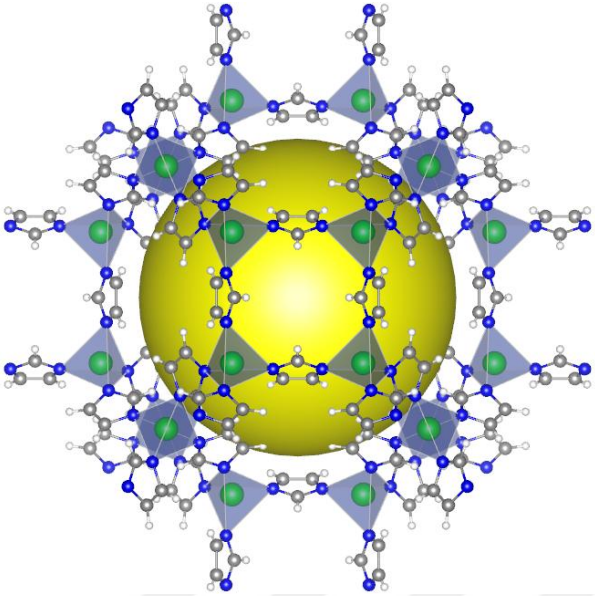

Figure 4.3. *Crystal structure of ZIF-8 framework (The yellow sphere represents the space in the cage. Colored balls represent atoms of Zn: green, N: blue, C: gray and H: white) [128]*

4.3. Porous Si Nanowires

Silicon-based zero-dimensional (quantum dots) and one-dimensional (Si nanowires) materials have attracted considerable attention due to their distinctive morphological, optical, electrical, and thermoelectric properties [129–132]. The methodologies employed for the fabrication of such materials are broadly categorized into top-down and bottom-up approaches. The principal distinction between these approaches lies in the fact that top-down methods involve the processing of macroscale materials through various physical and chemical procedures to yield nanomaterials, whereas bottom-up methods entail the growth of nanomaterials from the atomic level to the nanoscale via techniques such as molecular beam epitaxy (MBE), chemical vapor deposition (CVD), or chemical synthesis. In the specific context of Si nanowires, CVD can be cited as an example of a bottom-up approach, while electrochemical anodization and metal-assisted chemical etching (MACE) are illustrative examples of top-down methodologies [133–138]. In comparison to alternative techniques that necessitate specialised equipment, exhibit limited large-scale production capabilities, and are not cost-effective, the MACE method presents itself as an alternative and efficient approach for the fabrication of Si nanowires and porous Si nanowires [139]. Dimova-Malinovska et al. [140] published their initial observations in 1997, which revealed that aluminum

metal films enhance pore formation on Si surfaces in the presence of hydrofluoric acid (HF) and nitric acid (HNO_3). Subsequently, Li and Bohn [141] demonstrated that this finding constitutes a wet chemical route, utilizing transition metal atoms such as silver (Ag), gold (Au), or platinum (Pt) as catalysts, for the synthesis of low aspect ratio (small diameter and high length) Si nanowires. Furthermore, extant research suggests the feasibility of fabricating porous Si nanowires via a two-step MACE process [131, 139, 142–144]. The process of Si nanowire formation via the Metal-Assisted Chemical Etching (MACE) method is depicted below. Initially, the silicon material to be etched, for instance, a Si substrate, undergoes a step to facilitate the deposition of metal catalyst nanoparticles. This is achieved by exposing the Si substrate to a metal-containing solution. Subsequently, the Si substrate, now bearing the metal nanoparticles, is brought into contact with an etchant solution, leading to the formation of Si nanowires [145]. The MACE method is broadly categorized into one-step and two-step approaches. In the one-step MACE process, the Si material to be etched is exposed solely to an HF/metal solution. Consequently, the deposition of metal catalyst nanoparticles, the etching process and the formation of Si nanowires occur simultaneously.

Conversely, the two-step MACE method (Figure 4.4.) involves an initial step where metal nanoparticle deposition on the Si material is conducted within an HF/metal solution. The Si material is then exposed to a HF/hydrogen peroxide (H_2O_2) solution to form Si nanowires. The physical properties of Si nanowires produced by the MACE method depend on several parameters, in particular the majority carrier type of the Si material used (n-type or p-type), the doping concentration (high and low doping), the crystalline properties (single crystallinity and crystal orientation) and the type and size of the deposited metal nanoparticles. Previous research has shown that the use of n-type and highly doped (low resistivity) Si substrates, in particular, increases the porosity of porous Si nanowires fabricated by the two-step MACE method [146]. Another parameter influencing the porosity characteristics of Si nanostructures formed through the MACE process is denoted as ρ. The mathematical expression for the ρ parameter is as follows:

$$\rho = \frac{M_{HF}}{M_{HF} + M_{H_2O_2}} \tag{4.1}$$

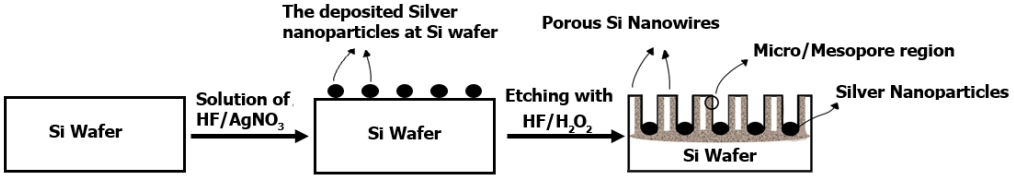

Figure 4.4. *Two step MACE process*

This parameter has a direct influence on the porosity characteristics of the resulting Si nanostructures. In particular, the existing literature has shown that a ρ value in the range of 0.85-0.95 is required for the synthesis of porous Si nanowires using n-type substrates [146]. Furthermore, the use of low resistivity n-type substrates is of great importance for the fabrication of porous Si nanostructures. Si nanowires find applications in various technological fields, including thermoelectric devices [147], photonics [148], electronic biosensors [149], lithium-ion batteries [150], and gas sensors [151].

5. EXPERIMENTAL

5.1. Synthesis of Cation Exchanged CLNs

The synthesis route of the cation-exchanged CLNs is illustrated in Figure 5.1. The raw CLN was used obtained from Gördes region in Türkiye. The 63-µm fraction was obtained by sieving the CLN. In order to eliminate soluble impurities, each 5.0 g zeolite sample was placed in 100 ml deionized water at 80 °C for six hours. Following this, all samples underwent separation and repeated washing with hot distilled water. In the second step of the process, the H^+ form (H-CLN) was obtained with 100 ml of 1.0 M NH_4NO_3 solutions at 80 °C for 12 h following calcination of the samples at 450 °C for 6 h. Subsequently, 5.0 g of each H-CLN sample was exchanged with 0.1 and 0.5 M solutions of $NaNO_3$, KNO_3, $LiNO_3$, $AgNO_3$, $Ni(NO_3)_2$, $Ca(NO_3)_2$, $Cu(NO_3)_2$, and $Mg(NO_3)_2$ at 80 °C for 12 h.

(a) (b)

Image 5.1 *(a): The reflux system used to cation exchange, (b) CLN sample after filtration*

The cation-exchanged samples were then separated and washed several times with deionized water at boiling point, and the dried samples were kept in an oven at 110 °C for 20 h and stored in a desiccator. The cation exchanged samples of H-CLN were labelled as M-X-CLN, where M and X represent the solution molarity and cation species respectively. The list of cation exchanged forms of the CLN sample is as follows: 0.1-Na-CLN, 0.1-K-CLN, 0.1-Ag-CLN, 0.1-Li-CLN, 0.1-Ca-CLN, 0.1Ma-CLN, 0.1-Cu-CLN, 0.1-Ni-CLN, 0.5-Na-CLN, 0.5-K-CLN, 0.5-Ag-CLN, 0.5-Li-CLN, 0.5-Ca-CLN, 0.5Ma-CLN, 0.5-Cu-CLN, 0.5-Ni-CLN.

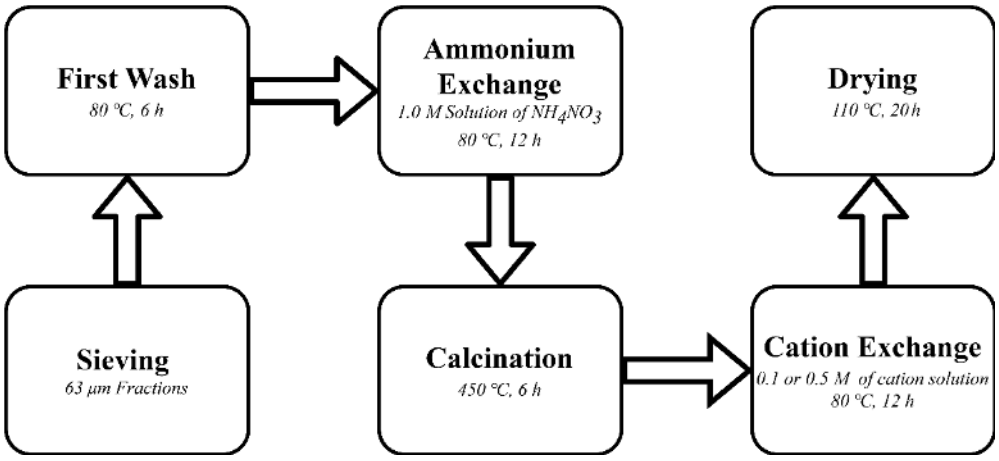

Figure 5.1. *The synthesis route of the cation-exchanged CLNs.*

5.2. Synthesis of ZIF-8 Samples

Pure ZIF-8 was synthesized by the solvothermal method as summarized below: First, 2-methylimidazole (2-mIm, 8 mmol) and zinc nitrate hexahydrate ($Zn(NO_3)_2$, 1 mmol) were separately added to methanol (MeOH, 11.2 mL). The zinc nitrate solution was then added to the 2-mIm solution and the final mixture was left at room temperature for 24 hours without stirring (Figure 5.2).

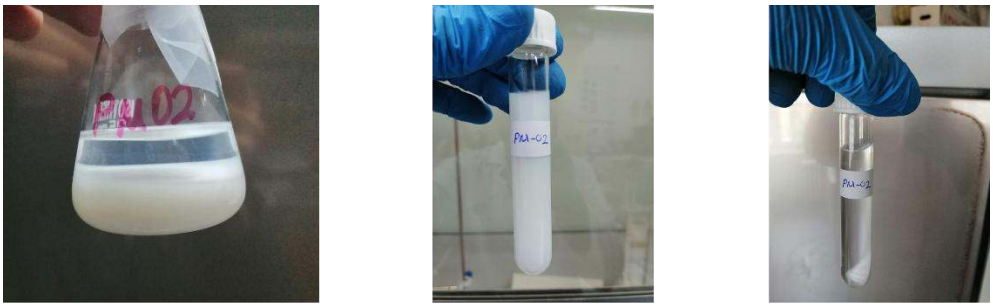

(a) (b) (c)

Image 5.2. *(a): 2- methylimidazole and zinc nitrate hexahydrate solution after 24 h, (b): solution before centrifugation, (c): solution after centrifugation*

This sample was designated ZIF-8_P. The synthesized ZIF-8 particles were collected by centrifugation at 4000 rpm for 10 minutes. After three washes with MeOH, all samples were dried at 80 °C for 24 hours. The cation-doped ZIF-8 samples were

synthesized using a method similar to that described above. The only difference was that different proportions (5%, 10% and 20%) of sodium or lithium cations were added to the zinc nitrate solution, keeping the total cation molarity (Zn + Li/Na) constant (1 mmol).

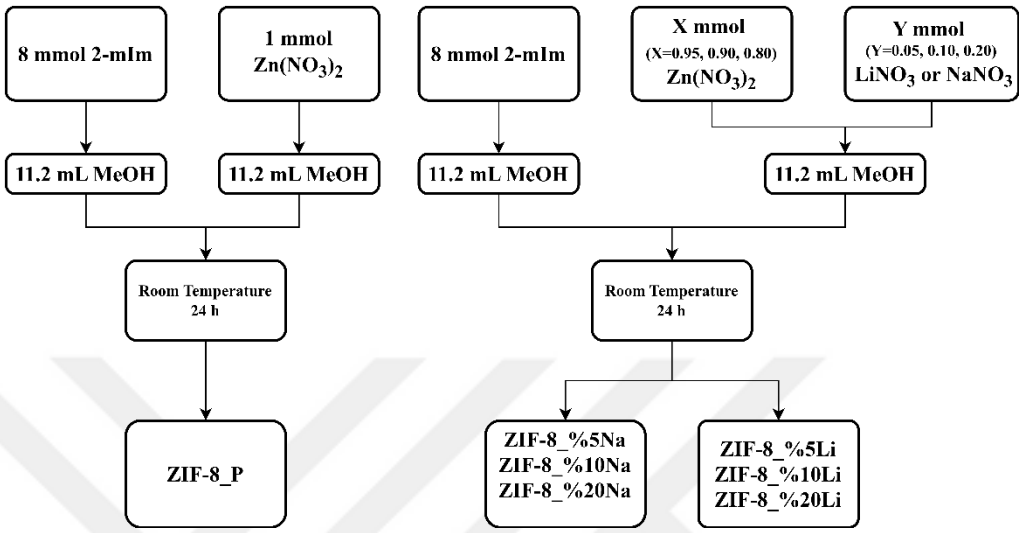

Figure 5.2. *The family tree of ZIF-8 samples*

5.3. Synthesis of Porous SiNW Samples

In this study, porous SiNWs were synthesized on n-type Si wafers using a two-step metal-assisted chemical etching (MACE) method. The wafers were single-crystal, 4-inch n-type Si with low resistivity (0.001–0.005 Ω·cm) and (100) orientation. They were first cut into 1.0 × 1.0 cm pieces and subjected to ultrasonic cleaning in acetone and isopropyl alcohol for five minutes each to remove soluble impurities. The samples were then rinsed with ultrapure water (R = 18 MΩ) and immersed in a piranha solution (V_{H2SO4}:V_{H2O2}=3:1) for 15 minutes to remove organic contaminants. They were then rinsed again with ultrapure water and treated with a dilute (5-10%) HF solution for 15 minutes to remove the native oxide layer.

For the first etching step, a mixture of 4.6 M HF and 0.005 M $AgNO_3$ was prepared in a 1:1 volume ratio. The samples were then immersed in this solution to deposit silver (Ag) on their surfaces. The deposition time varied between 10 and 30 seconds to determine the optimum duration. The second etching step, which led to the synthesis of porous nanowires, was then carried out. Ag-coated samples were immersed in a 1:1 (by volume) mixture of 4.6 M HF and X M H_2O_2 (X = 0.3 and 0.5) for 60, 90 and 180 minutes.

After etching, the samples were soaked in nitric acid for 10 minutes to remove the silver nanoparticles. Finally, they were treated with a 38% HF solution for 10 minutes to achieve surface passivation. The sample codes and family classifications for these pristine porous SİNWs are given in Table 5.3.1.

Table 5.1. *Synthesis parameters of undoped samples*

Sample	Ag Deposition Time(s)	H_2O_2 Molarity(M)	Etching Duration (minutes)
PNW-1	10	0.3	60
PNW-2	20	0.3	60
PNW-3	30	0.3	60
PNW-4	10	0.5	60
PNW-5	20	0.5	60
PNW-6	30	0.5	60
PNW-7	10	0.3	90
PNW-8	20	0.3	90
PNW-9	30	0.3	90
PNW-10	10	0.5	90
PNW-11	20	0.5	90
PNW-12	30	0.5	90
PNW-13	10	0.3	180
PNW-14	20	0.3	180
PNW-15	30	0.3	180
PNW-16	10	0.5	180
PNW-17	20	0.5	180
PNW-18	30	0.5	180

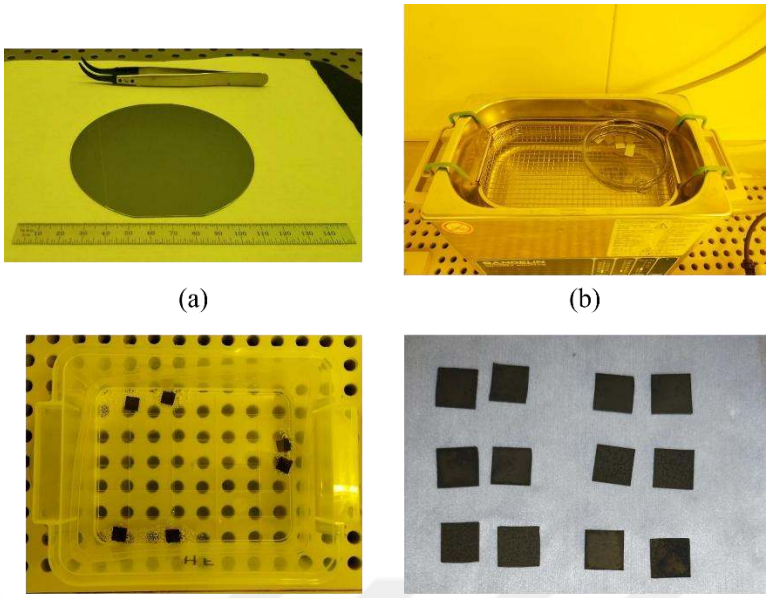

Image 5.3. *(a): N-type Si wafer used to synthesize porous Si nanowires, (b): samples cleaned with acetone in an ultrasonic bath, (c): samples during etching. (d): samples after etching*

Table 5.2. *Synthesis parameters of Au and Li doped samples*

Sample	Doped Atom	Molarity (mM)	Doping Duration (s)
PNW-A1	Au	0.001	5
PNW-A2	Au	0.001	15
PNW-A3	Au	0.01	5
PNW-A4	Au	0.01	15
PNW-L1	Li	0.001	5
PNW-L2	Li	0.001	15
PNW-L3	Li	0.01	5
PNW-L4	Li	0.01	15

For surface functionalization, the procedure optimized for the sample with the highest BET specific surface area (PNW-5) was used. Chloroauric acid ($HAuCl_4$) and lithium nitrate ($LiNO_3$) were used as Au and Li sources respectively. In this step, the samples were exposed to 4.6 M HF/X mM Au or Li solutions (X = 0.001 and 0.01) during the final step of the MACE process, coinciding with the surface passivation. The codes for the surface functionalized samples are given in Table 5.2.

5.4. Characterization Methods and Parameters

5.4.1. XRD

The crystallographic structure of clinoptilolite and ZIF-8 samples were examined by XRD measurements. X-ray powder diffraction (XRD) patterns was recorded using a Bruker D8 Advance XRD with Cu-Kα radiation (λ = 1.542 Å) at 40 kV and 40 mA. Data were collected at room temperature over a 2θ range of 5–40° with a step size of 0.02°.

Image 5.4. *The Bruker D8 Advance XRD*

5.4.2. XRF

Elemental analysis of all clinoptilolite samples was performed using a Rigaku ZSX Primus X-ray fluorescence (XRF) spectrometer using the fusion method to determine their chemical composition. Loss of ignition (LOI) was measured by recording the change in mass after heating the samples to 1000°C at a controlled heating rate of 10 °C.min^{-1}. The samples were held at this temperature for 1 hour before cooling to room temperature at the same rate.

Image 5.5. *Rigaku ZSX Primus XRF spectrometer*

5.4.3. FT-IR

Fourier Transform Infrared (FT-IR) spectra of the clinoptilolite samples were recorded using a BRUKER Vertex 80v spectrometer in the range 400-4000 cm^{-1} with a resolution of 4 cm^{-1}. Prior to analysis, both the clinoptilolite samples and potassium bromide (KBr) were dried in an oven at 105 °C for 3 hours to remove moisture.

Image 5.6. *BRUKER Vertex 80v FT-IR spectrometer.*

The dried sample was then mixed with KBr in a mass ratio of 1:400 (sample:KBr) to ensure uniform dispersion. The resulting mixture was pelletized using a manual hydraulic press under a load of 2 tons for approximately 2 minutes to form transparent pellets suitable for infrared analysis.

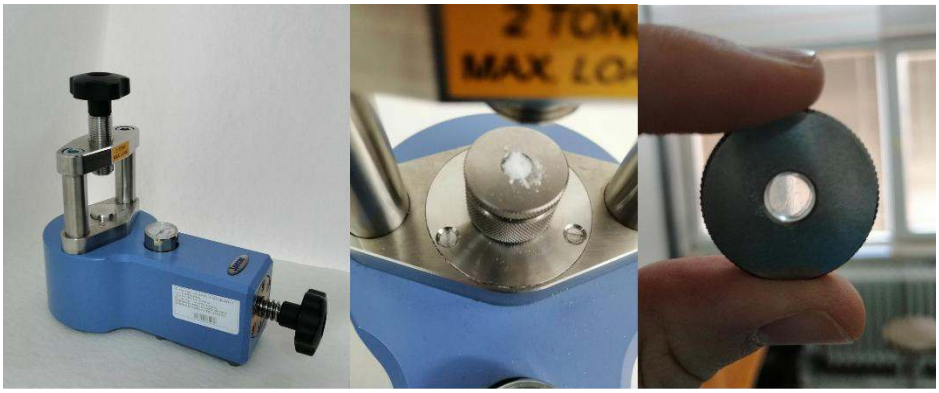

(a) (b) (c)

Image 5.7. *The apparatus under consideration is a hydraulic press that is utilized for the purpose of pellet pressing. (a): hydraulic press used for pressing pellets, (b): pellet pressing stage, (c): pellet ready for analysis*

5.4.4. SEM and EDS

Scanning electron microscopy (SEM) images were obtained using a Zeiss Ultra Plus field emission scanning electron microscope (FE-SEM) operated at an acceleration voltage of 5 kV (for CLN and ZIF-8 samples) and 5-15 kV (for porous SiNWs). Prior to analysis, CLN and ZIF-8 samples were coated with a thin gold layer to improve conductivity and image quality. The chemical composition of the porous SiNW samples was analyzed by energy dispersive X-ray spectroscopy (EDS) using an EDAX Pegasus system integrated with a FE-SEM apparatus. For the EDS analysis, spectra were acquired from three randomly selected points on each sample and the elemental composition was determined by averaging the data obtained.

Image 5.8 *Zeiss Ultra Plus FE-SEM and EDAX Pegasus system*

5.4.5. Obtaining and analysis of N_2 adsorption isotherms

The specific surface area and micropore characteristics of CLN, ZIF-8 and porous SiNW samples were determined from nitrogen adsorption measurements at 77 K up to a relative pressure of P/P_0=1. N_2 adsorption analyses of all samples were performed using a Micromeritics 3Flex volumetric adsorption apparatus. Samples were degassed using a Micromeritics Smart VacPrep device. CLN samples were degassed at 350 °C for 8 hours. ZIF-8 samples were degassed at 90°C for 1 hour followed by a second degassing at 190 °C for 4 hours. Porous SiNw samples were degassed under vacuum conditions at 150 °C for 8 hours. High purity N_2 gas (99.99%) was used for all adsorption experiments to ensure measurement accuracy. The BET method was used to determine the specific surface area from the adsorption isotherms within a relative pressure range of 0.05-0.35 P/P_0. The pore size distribution was analyzed using the t-plot and density functional theory (DFT) methods implemented in the MicroActive software supplied with the Micromeritics 3Flex instrument. A cylindrical pore geometry was assumed for porous SiNWs to perform DFT calculations. The t-plot method was also not applicable to these samples.

(a) (b)

Image 5.9. *(a): Micromeritics 3Flex volumetric adsorption analyzer, (b): Micromeritics Smart VacPrep apparatus*

5.4.6. Obtaining of H_2 adsorption isotherms

Hydrogen adsorption isotherms were recorded at 77 K up to 113 kPa. H_2 adsorption analyses of all samples were performed using a Micromeritics 3Flex volumetric adsorption apparatus using the same degassing procedures as for N_2 adsorption analysis. High purity H_2 gas (99.99%) was used in all adsorption experiments.

6. RESULTS AND DISCUSSION

In this chapter, a detailed discussion of the experimental results will be presented. In order to ensure a coherent flow, it is first necessary to evaluate each material according to the specific characterization techniques applied. Finally, the hydrogen storage properties of all samples utilized in this study will be examined, and the obtained results will be compared with relevant data from the literature.

6.1. Characterization of CLN Samples

6.1.1. XRD

The powder X-ray diffraction (XRD) patterns of the raw CLN, H-CLN, and their cation-exchanged derivatives are presented in Figures 6.1 and 6.2. For the CLN sample, characteristic reflections of clinoptilolite were observed at d-spacings of 8.95, 7.91, 3.96, and 2.79 Å, corresponding to 2θ values of 9.88°, 11.17°, 22.50°, and 32.01° with Miller indices (hkl) of (020), (200), (131), and (530), respectively [36, 152]. In accordance with the methodology established by Esenli and Sirkecioğlu [153], phase analysis of the raw CLN sample indicated a predominant clinoptilolite phase (80-85%), accompanied by minor constituents of feldspar (3%), opal-A (5-10%), and illite (2%).

In the XRD patterns of H-CLN and its cation-exchanged counterparts, a reduction in the relative intensity of the (200) reflection was observed in comparison to the (020) reflection, while the angular positions of the principal clinoptilolite reflections remained largely unchanged. In accordance with the established dependence of the (020) reflection intensity on the Na/K ratio within clinoptilolite samples, the observed variations in the absolute and relative intensities of the characteristic clinoptilolite reflections can be attributed to alterations in the exchangeable cation ratio, in addition to modifications in the pore dimensions and morphology of the clinoptilolite framework [98, 154–156] . A broad baseline feature between 19° and 30° 2θ is typically associated with the direct modification of clinoptilolite-type zeolites via acid treatment. However, this characteristic hump was absent in the patterns of H-CLN and its cation-modified forms in this study.

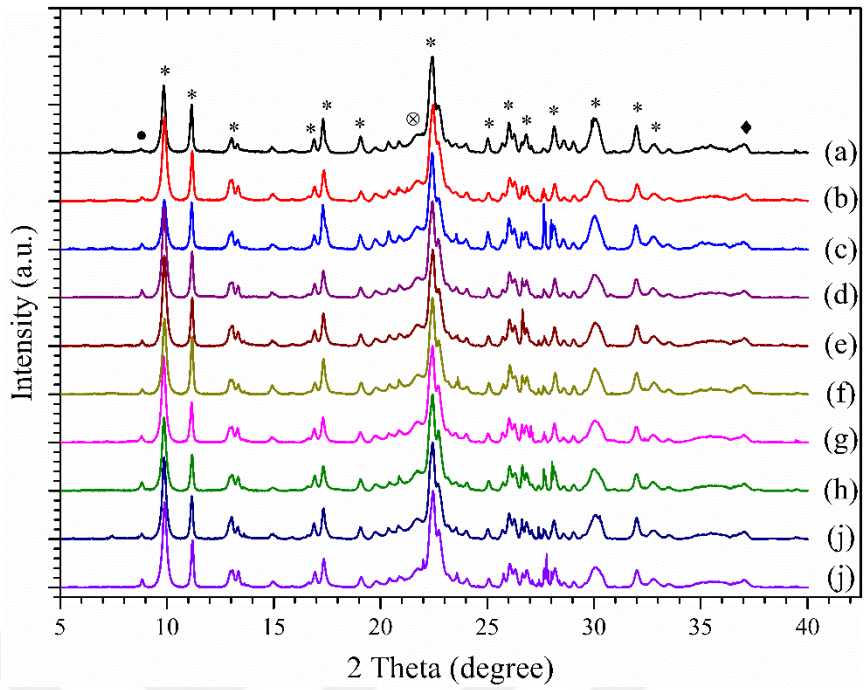

Figure 6.1. *XRD patterns belongs to specimens of (a): Raw-CLN, (b): Parent-CLN, (c): 0.1-Ag-CLN, (d): 0.1-Li-CLN, (e): 0.1-Na-CLN, (f): 0.1-K-CLN, (g): 0.1-Ni-CLN, (h): 0.1-Cu-CLN, (i): 0.1-Ca CLN, (j): 0.1-Mg-CLN (*clinoptilolite, •: illite, ⊗: opal A, •: feldspar)*

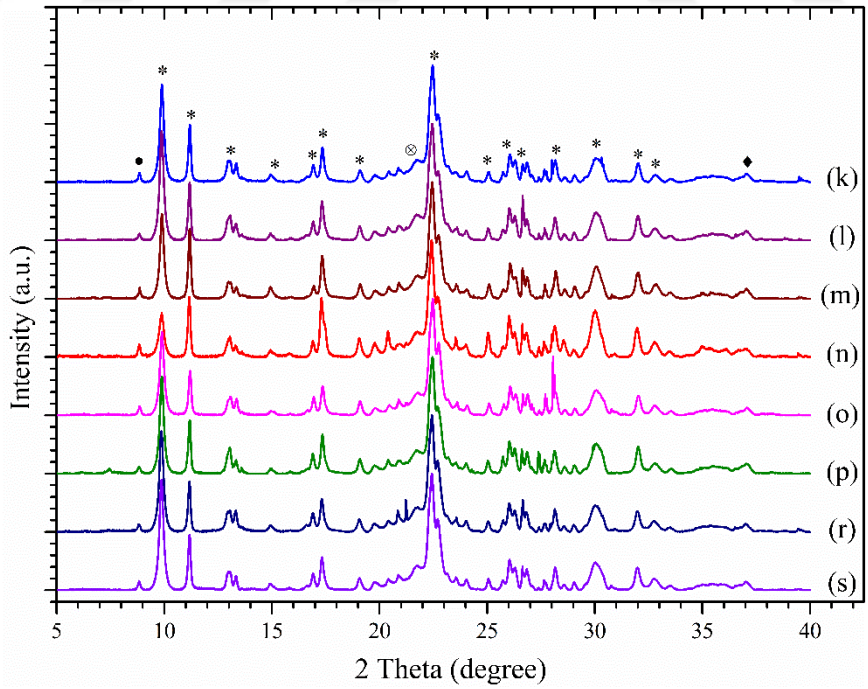

Figure 6.2. *XRD patterns belongs to specimens of (k): 0.5-Ag-CLN, (l): 0.5-Li-CLN, (m): 0.5-Na-CLN, (n): 0.5-K-CLN, (o): 0.5-Ni-CLN, (p): 0.5-Cu-CLN, (r): 0.5-Ca-CLN, (s): 0.5-Mg-CLN (*clinoptilolite, •: illite, ⊗: opal A, •: feldspar)*

This absence is attributed to the indirect generation of the H^+ form through ammonium nitrate modification followed by calcination, a process that did not induce significant structural degradation of the clinoptilolite framework [98, 157]. The unit cell parameters (a, b, c, and β) and volumes of the CLN, H-CLN, and their cation-exchanged derivatives, derived from the miller indices (hkl) which define the planes within the monoclinic crystal system, are compiled in Table 6.1. A decrease in the unit cell volume of the H-CLN sample was observed in comparison to the CLN, a reduction attributed to calcination consistent with findings reported in other studies on clinoptilolite [158, 159].

Table 6.1. *Unit cell parameters of CLN samples*

Sample	a (Å)	b (Å)	c (Å)	β (°)	V (Å^3)
Raw-CLN	17.76	17.94	7.41	117.10	2100.68
H-CLN	17.79	17.88	7.41	117.23	2095.69
0.1-K-CLN	17.74	17.88	7.40	116.88	2093.18
0.5-K-CLN	17.74	17.86	7.40	116.98	2090.25
0.1-Na-CLN	17.77	17.90	7.41	117.14	2097.35
0.5-Na-CLN	17.77	17.90	7.41	117.08	2099.19
0.1-Ca-CLN	17.78	17.92	7.41	117.21	2099.63
0.5-Ca-CLN	17.77	17.88	7.41	117.10	2094.01
0.1-Mg-CLN	17.78	17.88	7.40	117.16	2093.43
0.5-Mg-CLN	17.77	17.92	7.41	117.11	2099.70
0.1-Li-CLN	17.77	17.92	7.40	117.06	2098.19
0.5-Li-CLN	17.77	17.95	7.41	117.06	2104.70
0.1-Ag-CLN	17.77	17.90	7.41	117.00	2100.02
0.5-Ag-CLN	17.78	17.90	7.41	116.99	2100.27
0.1-Ni-CLN	17.77	17.95	7.41	117.22	2101.38
0.5-Ni-CLN	17.78	17.88	7.40	117.16	2093.43
0.1-Cu-CLN	17.76	17.92	7.40	117.05	2097.19
0.5-Cu-CLN	17.76	17.86	7.40	117.06	2089.00

6.1.2. Elemental composition

The results of the X-ray fluorescence (XRF) analysis conducted on the pristine CLN, H-CLN, and their cation-exchanged derivatives are presented in Table 6.2. The elemental composition of the raw CLN indicates a high abundance of calcium and potassium. It is noteworthy that the SiO_2/Al_2O_3 ratios of H-CLN (5.6) and its cation-modified forms (ranging from 5.5 to 5.8) demonstrate no significant variation when

compared to that of the raw CLN (5.4). This consistency can be attributed to the preservation of the crystal structure during the calcination step following ammonium nitrate pretreatment, thereby preventing progressive delamination. A comparative analysis of the chemical composition between the raw sample and the H-CLN samples reveals a significant depletion of exchangeable cations, particularly CaO and K_2O components, from the structure after treatment with 1.0 M ammonium nitrate solution and subsequent calcination. Subsequent to the ion exchange of H-CLN with various cations, an enrichment in the respective oxide compositions of the cation-exchanged forms was observed, directly proportional to the specific salt solution employed and its increasing molarity. However, the presence of lithium in the structure cannot be directly detected. This phenomenon can be attributed to the low intensity and long wavelength of the emitted fluorescence, which is characteristic of light elements.

Table 6.2. *Effective ionic and hydrated radius of the cations employed (L.O.I. values belongs to the samples which are modified with 0.5 M solutions)*

Cation	Effective Ionic Radius (nm)	Hydrated Radius (nm)	L.O.I (%)
K^+	0.149	0.331	6.09
Ag^+	0.126	0.341	6.26
Na^+	0.117	0.358	7.34
Li^+	0.094	0.382	7.54
Ni^{2+}	0.100	0.404	7.71
Ca^{2+}	0.100	0.412	7.20
Mg^{2+}	0.072	0.428	7.54
Cu^{2+}	0.073	0.600	7.27
H^+	0.01	0.025	6.80

An inverse relationship exists between the hydrated radius of a cation and its effective ionic radius [160]. Consequently, an increase in glow loss rates can be anticipated in samples modified with cations that possess small effective ionic radii. The results presented in Table 6.2 lend credence to this scenario.

6.1.3. FT-IR

The Fourier Transform Infrared (FT-IR) spectra of raw CLN and H-CLN samples are presented in Figure 6.3. The characteristic vibrational bands of the CLN structure are observed within the wavenumber range of 400-1200 cm^{-1}. The absorption band centered at approximately 3640 cm^{-1} and the broad absorption band at 3440 cm^{-1} are attributed to the stretching vibrations of structural OH groups and the OH stretching vibrations of adsorbed water molecules, respectively. The bending mode of water molecules is evident at 1642 cm^{-1}. The band at 793 cm^{-1} is assigned to the three-dimensional silica network, while the band at 466 cm^{-1} corresponds to Si-O-Si bending vibrations. The most intense band, located at 1049 cm^{-1}, is attributed to the T-O (T=Si or Al) stretching mode [161]. The position of this band is directly correlated with the Si and Al content of the CLN framework; a decrease in the number of Al^{3+} ions within the CLN unit cell results in a shift of this band to higher wavenumbers.

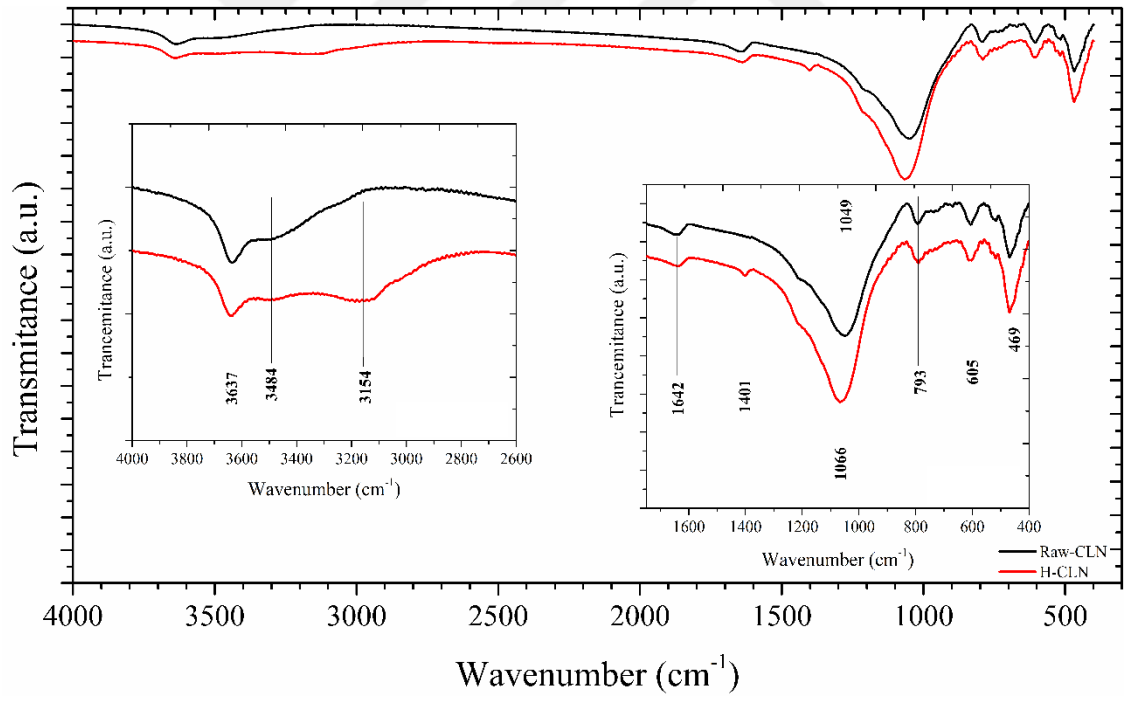

Figure 6.3. *FT-IR spectra of raw CLN and H-CLN samples*

For the H-CLN sample, this band exhibits a slight shift to a higher wavenumber of 1066 cm^{-1}. This phenomenon can be ascribed to the migration of aluminum ions from the tetrahedral centers of the zeolite framework to cationic sites at calcination temperatures

exceeding 400 °C, leading to a rearrangement of Al^{3+} species [162]. The pretreatment protocol employed to obtain the H^+ form of CLN did not induce dealumination but exclusively resulted in modifications within the tetrahedral Al^{3+} environment, as corroborated by the absence of a broad baseline between 19-30 degrees 2θ in the X-ray diffraction patterns (Figure 6.1 and 6.2). Furthermore, the FT-IR spectrum of the H-CLN sample revealed the emergence of new bands at 1401 and 3154 cm^{-1}, which are attributable to the presence of ammonium ions [162, 163].

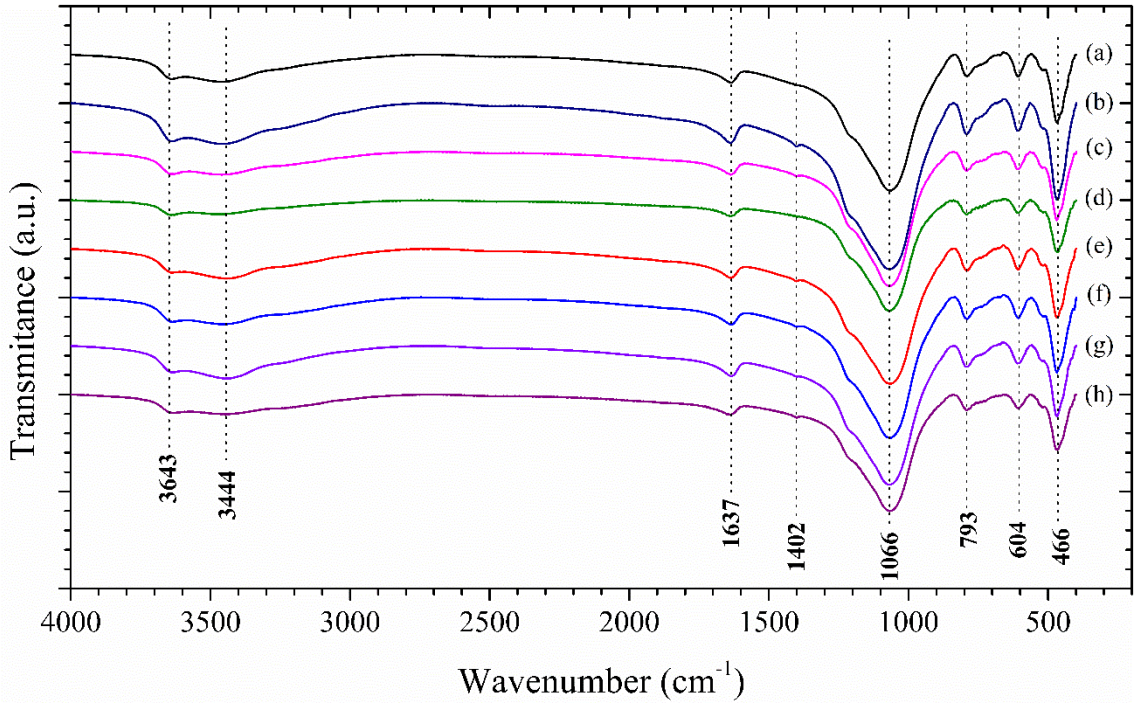

Figure 6.4. *FT-IR spectra of (a):0.1-Ag-CLN, (b):0.1-Li-CLN, (c):0.1-Na-CLN, (d):0.1-K-CLN, (e):0.1-Ni-CLN, (f):0.1-Cu-CLN, (g):0.1-Ca-CLN, (h):0.1-Mg-CLN*

Notably, the subsequent cation exchange process did not elicit significant alterations in the IR spectra of the Ag^+, Na^+, Li^+, K^+, Mg^{2+}, Ca^{2+}, Cu^{2+}, and Ni^{2+} exchanged forms (Figures 6.4 and 6.5), a finding consistent with previous investigations [164–168].

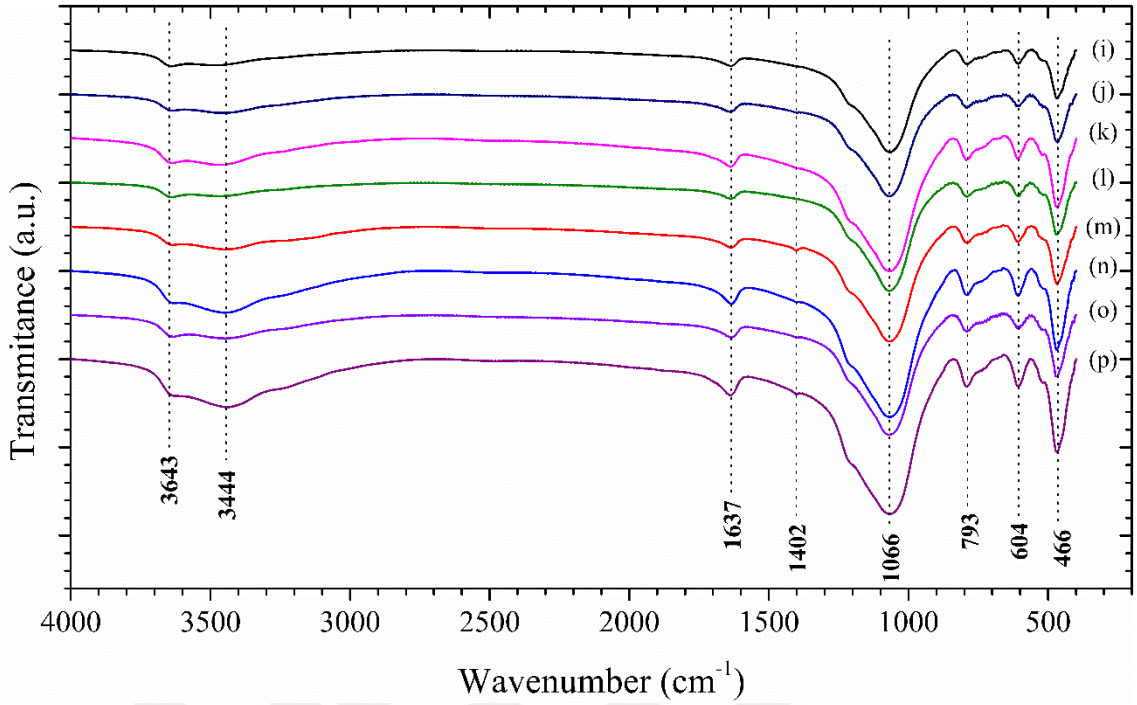

Figure 6.5. *FT-IR spectra of (i):0.5-Ag-CLN, (j):0.5-Li-CLN, (k):0.5-Na-CLN, (l):0.5-K-CLN, (m):0.5-Ni-CLN, (n):0.5-Cu-CLN, (o):0.5-Ca-CLN, (p):0.5-Mg-CLN*

6.1.4. SEM

SEM micrographs of the Raw-CLN sample are presented at various magnifications in Figure 6.6. CLN crystals are typically observed to be in the form of layered structures, coffin-shaped, tabular, or platy [166, 169]. The lamellar morphology of the clinoptilolite crystals is clearly evident in this figure. Moreover, the micrographs indicate that the clinoptilolite particles are formed through the agglomeration of lamellae, rather than through the continuous growth of a single crystalline structure [170].

A comparison of the SEM micrograph of the H-CLN sample, as shown in Figure 6.7, with that of the Raw-CLN sample reveals that the process utilizing ammonium nitrate does not exert a detrimental effect on the clinoptilolite morphology. It is important to note that the observed cavities in the SEM images are not representative of the intrinsic channel structure of clinoptilolite but rather reflect the macroporous texture exhibited by micron-sized particles within the tuff.

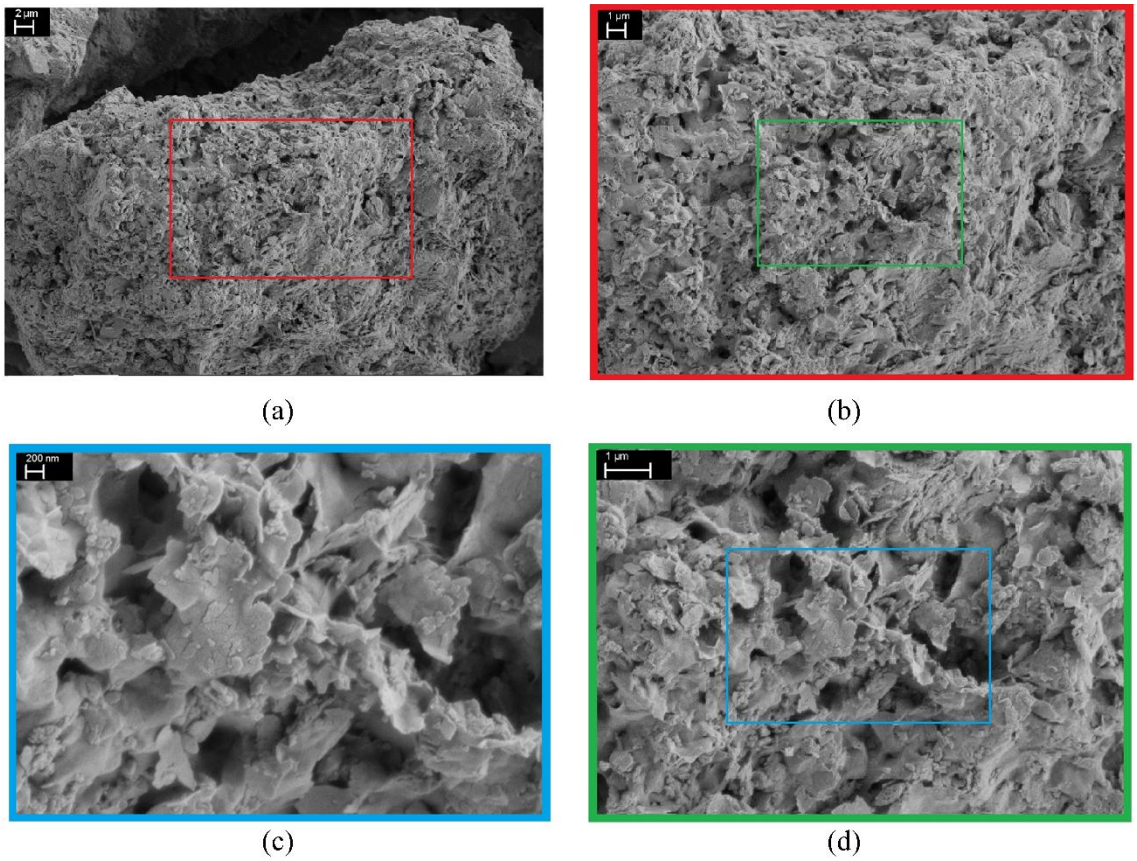

Figure 6.6. *SEM micrographs of the R-CLN sample at various magnifications: (a) 5000x, (b) 10000x, (c) 50000x, (d) 25000x*

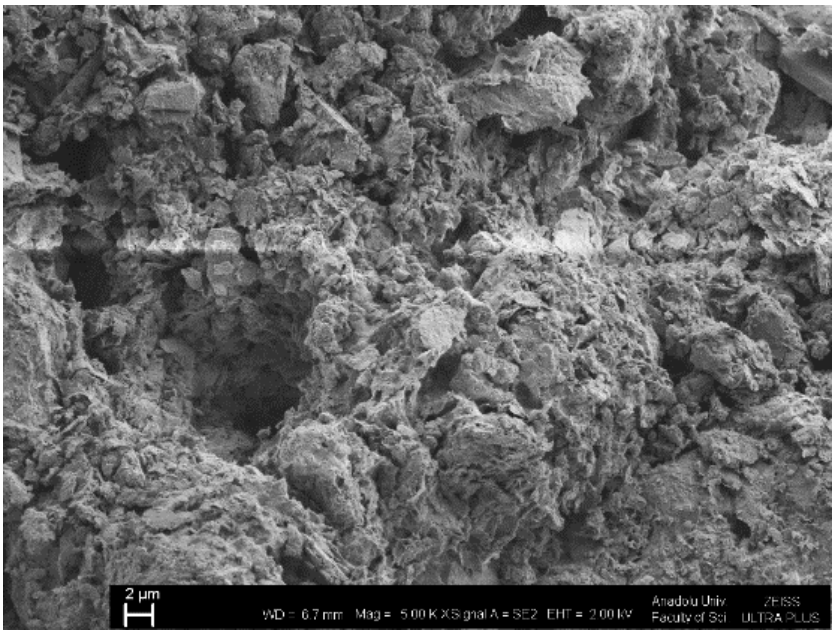

Figure 6.7. *SEM micrographs of the H-CLN*

The morphological characteristics of selected cation-exchanged samples are presented in Figures 6.8, 6.9 and 6.10. Analysis of the SEM results indicates that the modification procedures applied to the samples do not induce any significant structural damage to the morphology of the clinoptilolite specimens.

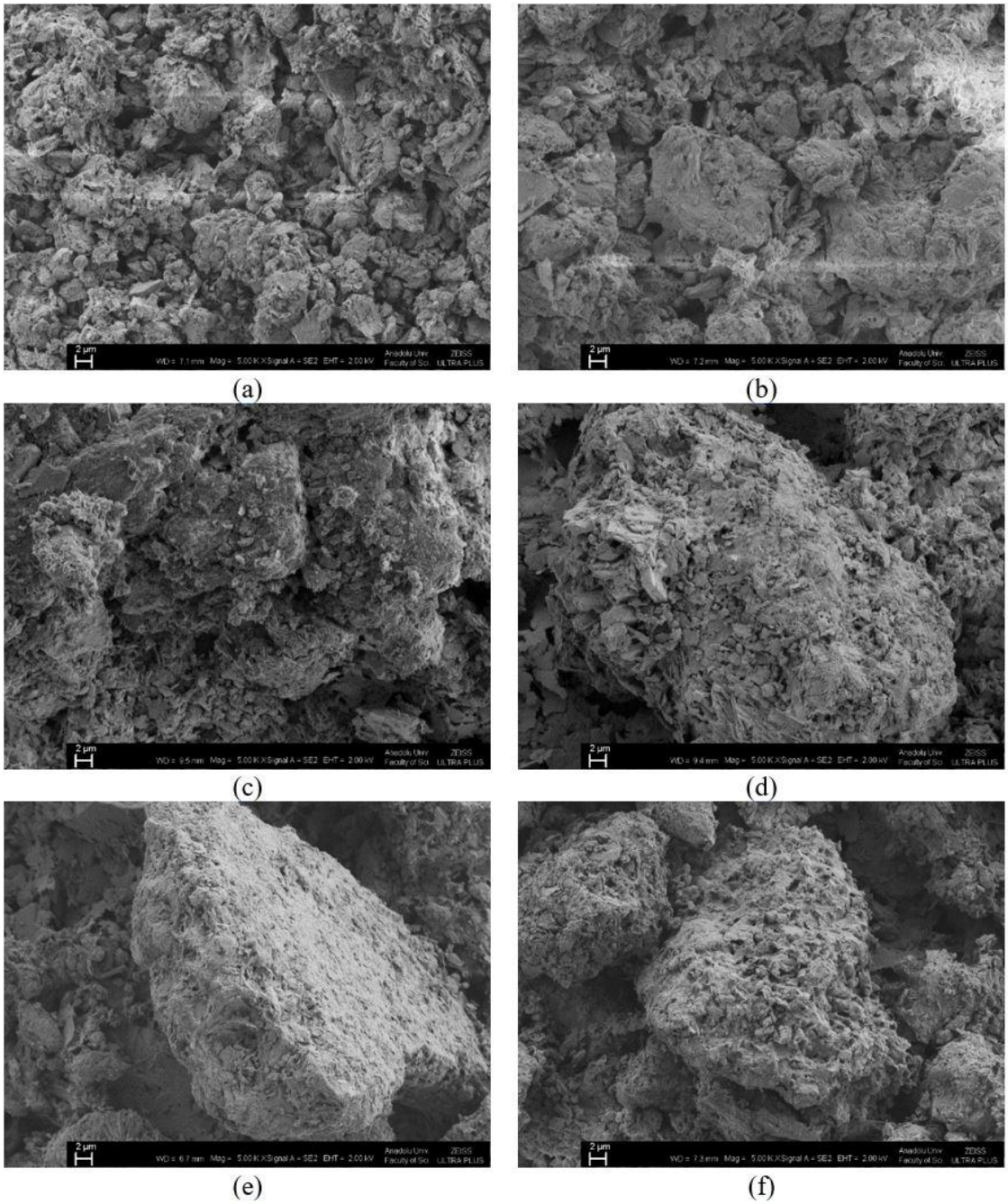

Figure 6.8. *SEM images of cation-exchanged samples: (a) 0.1-Ag CLN, (b) 0.5-Ag-CLN, (c) 0.1-Cu-CLN, (d) 0.5-Cu-CLN, (e) 0.1-Ni-CLN, (f) 0.5-Ni-CLN (Scale bars: 2 µm)*

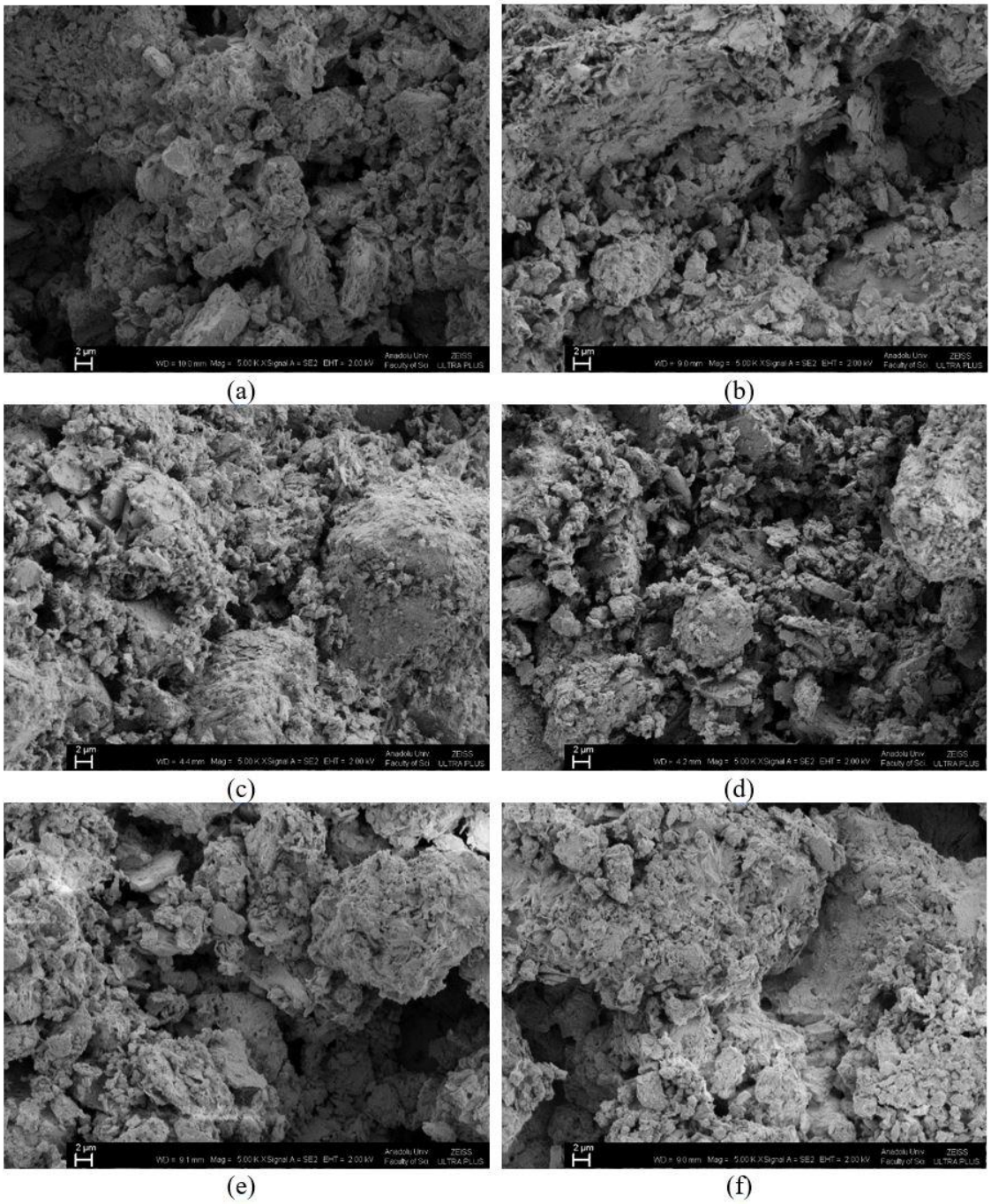

Figure 6.9. *SEM images of cation-exchanged samples: (a) 0.1-Li-CLN, (b) 0.5-Li-CLN, (c) 0.1-Na-CLN, (d) 0.5-Na-CLN, (e) 0.1-K-CLN, (f) 0.5-K-CLN (Scale bars: 2 μm)*

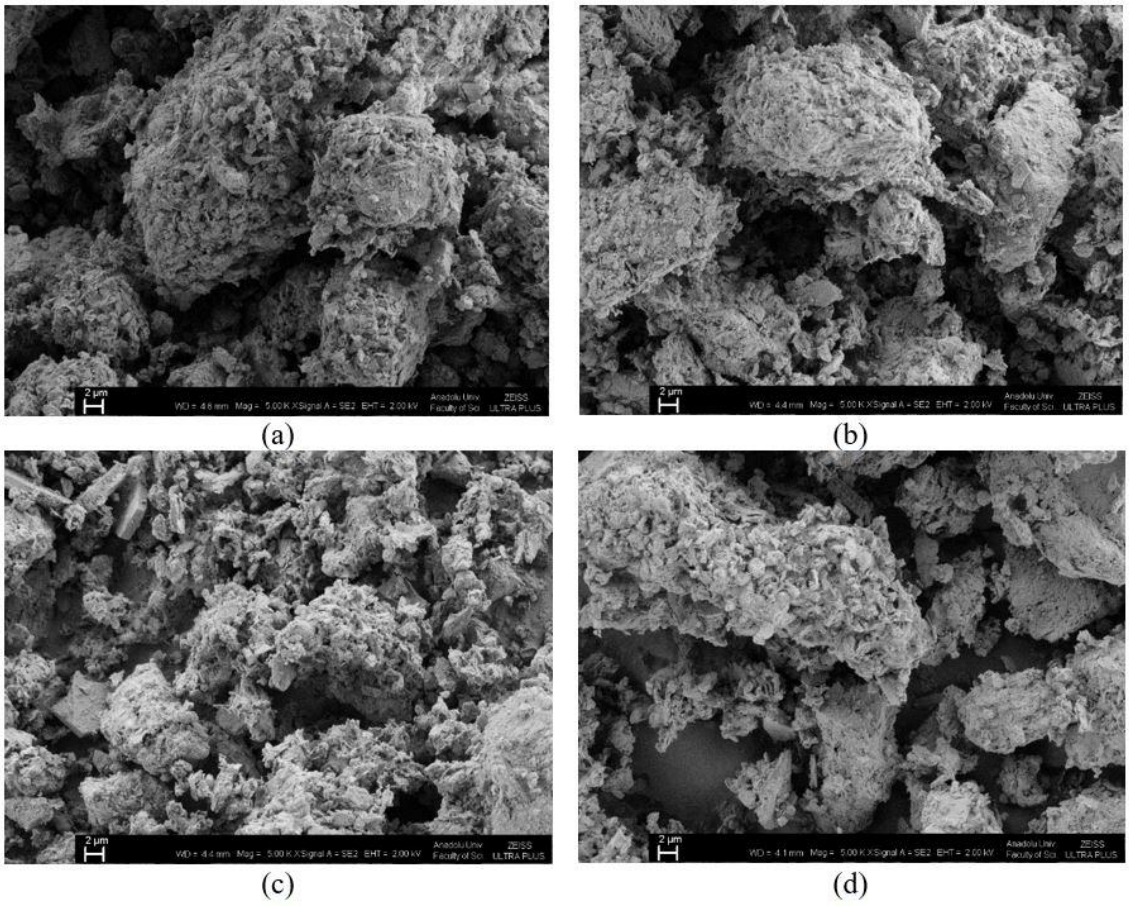

Figure 6.10. *SEM images of cation-exchanged samples: (a) 0.1-Mg-CLN, (b) 0.5-Mg-CLN, (c) 0.1-Ca-CLN, (d) 0.5-Ca-CLN (Scale bars: 2 µm)*

6.1.5. N_2 adsorption

The nitrogen adsorption isotherms of CLN and H-CLN samples are illustrated in Figure 6.11. According to IUPAC classification adsorption isotherm of the raw CLN sample displayed Type IV character. This is clearly shown that the Raw-CLN sample displayed mesoporous character, which is expected [86]. On the other hand, the isotherm belongs to H-CLN sample has totally different character. This isotherm shows Type I behavior at low relative pressure region which corresponds to microporosity and the hysteresis loop indicates the mesoporosity. Furthermore, the adsorption isotherm does not reveal a truly horizontal plateau at relative pressures > 0.1; the observed slope being associated with the filling of mesopores [25]. The hysteresis loops observed for these samples are classified as type H4, characterized by a pronounced uptake at low relative pressures, indicative of micropore filling. H4-type hysteresis is commonly associated with aggregated crystals of zeolites, certain mesoporous zeolites, and micro-mesoporous

carbons [25, 85]. The presence of low-pressure hysteresis in all isotherms may be attributed to the irreversible entrapment of adsorbate molecules within the pore structure, as well as potential volume changes of the adsorbent material resulting from the swelling of non-rigid pores [25].

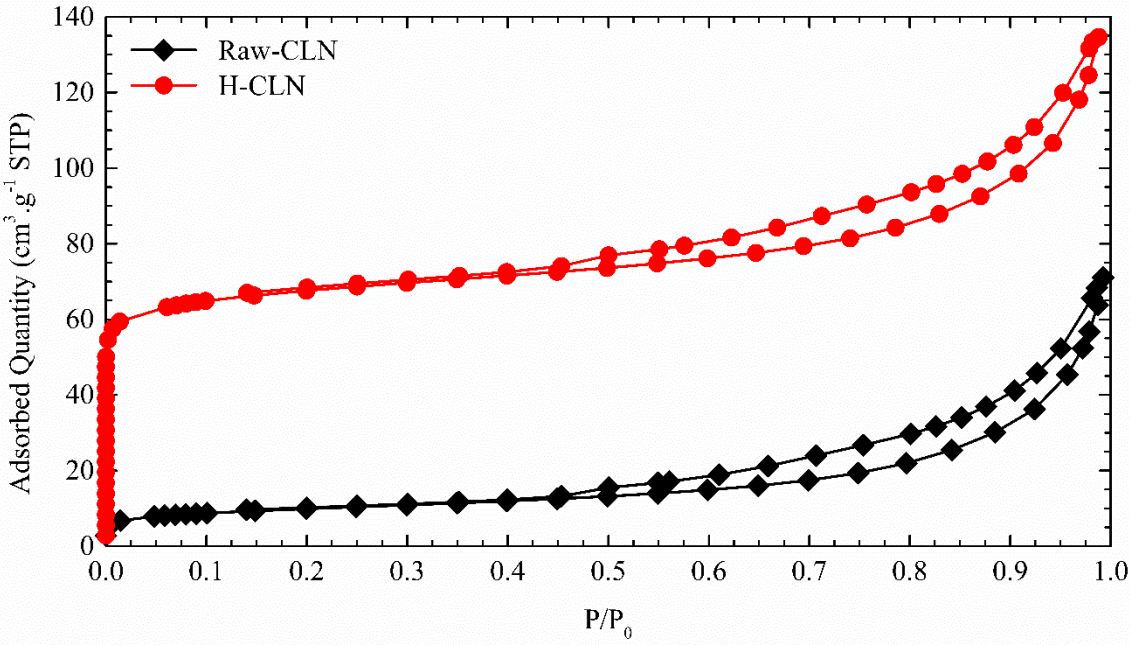

Figure 6.11. *N_2 adsorption isotherms of raw CLN and H-CLN samples at 77 K*

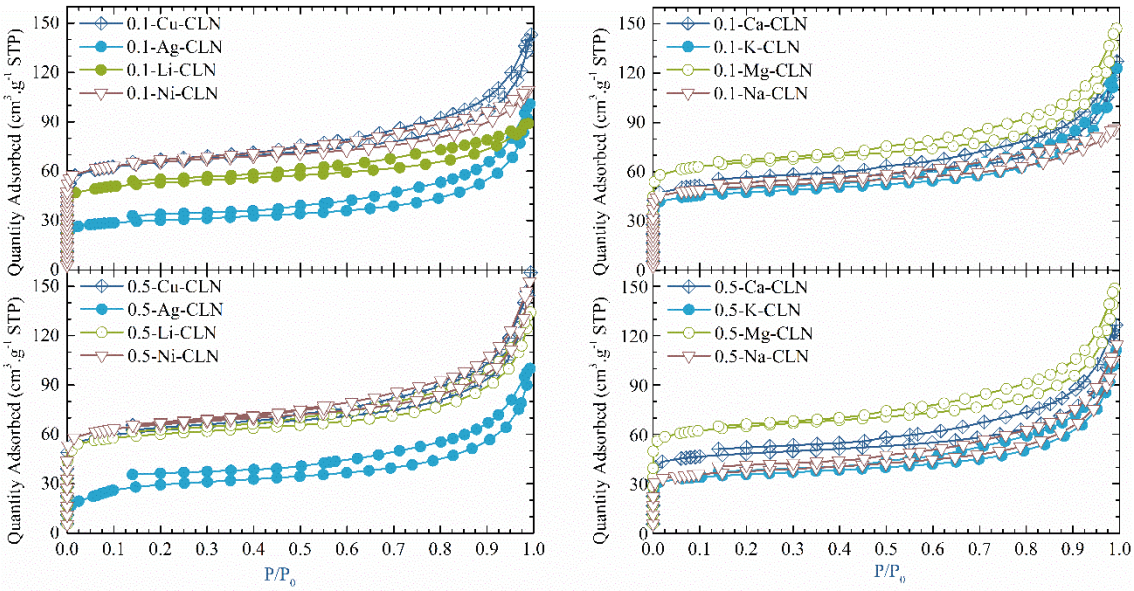

Figure 6.12. *N_2 adsorption isotherms of cation-exchanged forms*

Similar results also are observed in the adsorption isotherms of cation exchanged forms (Figure 6.12).

Table 6.3 compiles the BET specific surface area and micropore data for the cation-modified samples. The results reveal that the BET surface area of all cation-exchanged samples is lower than that of the parent H-CLN. This reduction can be ascribed to the diminutive size and high charge density of the H^+ cation, which leads to a more open pore network in the zeolite following pretreatment and a decrease in the channel blocking factor [171].

Table 6.3. *Porous properties of raw, H-CLN and the other modified CLN samples*

Sample	BET Specific Surface Area ($m^2.g^{-1}$)	Micropore Surface Area ($m^2.g^{-1}$)	Micropore Volume (x 10^{-2} cm3.g^{-1})
Raw-CLN	35.66	9.55	0.39
H-CLN	259.66	200.08	7.84
0.1-Ni-CLN	252.82	216.02	8.58
0.5-Ni-CLN	253.28	209.81	8.34
0.1-Cu-CLN	251.21	204.95	8.13
0.5-Cu-CLN	238.88	194.58	7.76
0.1-Ag-CLN	115.30	86.62	3.42
0.5-Ag-CLN	70.45	42.87	1.74
0.1-Li-CLN	202.23	167.88	6.70
0.5-Li-CLN	231.94	192.11	7.59
0.1-Na-CLN	196.87	164.93	6.52
0.5-Na-CLN	143.61	110.19	4.36
0.1-K-CLN	182.84	147.82	5.84
0.5-K-CLN	136.21	105.21	4.17
0.1-Ca-CLN	205.93	169.35	6.72
0.5-Ca-CLN	186.59	153.74	6.06
0.1-Mg-CLN	253.05	210.15	8.35
0.5-Mg-CLN	249.86	207.88	8.23

It is noteworthy that the cation exchange of H^+ ions with K^+ and Ag^+ cations led to a substantial decrease in both the BET surface area and the micropore area. In the case of the K^+-exchanged sample, this phenomenon can be attributed to the substantial ionic radius of the K^+ cation and consequent pore blockage due to its preferential localization within the channels. Typically, K^+ cations occupy the central region of the eight-membered ring C channels (M(3) site). However, once the M(3) sites are saturated, K^+

cations may also occupy the M(2) or M(4) sites. This phenomenon leads to partial obstruction of the A and B channels [172]. Consequently, the accessibility of N_2 molecules to the micropores is reduced [173]. In addition, the specific locations occupied by Li^+ and Na^+ cations within the channel system may impede the diffusion of N_2 gas as well [98]. These findings are consistent with results reported for natural, acid-activated, cation-exchanged, or thermally treated clinoptilolite in various studies within the literature [36, 161, 173, 174].

6.2 Characterization of ZIF-8 Samples

6.2.1 XRD

The patterns obtained from the powder X-ray diffraction (XRD) analysis of the pristine ZIF-8 and its cation-exchanged derivatives are presented in Figure 6.13.

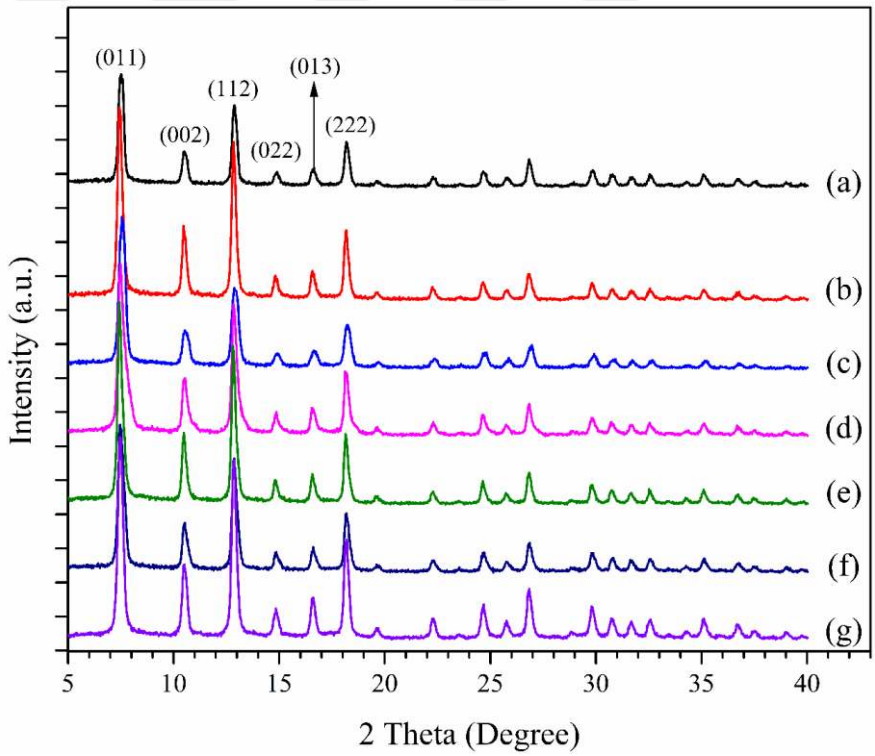

Figure 6.13. *XRD patterns of ZIF-8 samples (a): ZIF-8_P, (b): ZIF-8_5% Li, (c): ZIF-8_10% Li, (d): ZIF-8_20% Li, (e): ZIF-8_5% Na, (f): ZIF-8_10% Na, (g): ZIF-8_20% Na*

For the ZIF-8_P specimen, characteristic reflections were identified at 2θ values of 7.52°, 10.51°, 12.89°, 14.91°, 16.65°, and 18.18°, corresponding to Miller indices (hkl) of (011), (002), (112), (022), (013), and (222), respectively (Table 6.4). The observed diffraction reflections are consistent with previously published data, thereby confirming

the formation of the typical sodalite-type structure of ZIF-8 [175–177]. Moreover, the corresponding hkl indices and 2θ values for the other samples are tabulated in Table 6.4. The XRD patterns of ZIF-8_P and the other samples manifest sharp and well-resolved reflections, indicative of their high crystallinity. A comparison of the diffraction patterns obtained for the Li- and Na-exchanged forms of ZIF-8 samples revealed that the incorporation of Li and Na cations into the synthesis solutions did not result in the destruction of the crystal structure of ZIF-8.

Table 6.4. *Unit cell parameters, miller indices and corresponding 2θ values of ZIF-8 samples*

Unit Cell Parameter		**ZIF-8_P**		**ZIF-8_5% Li**		**ZIF-8_10% Li**	
Sample	**a (nm) from (011)**	**hkl**	**2θ (deg)**	**hkl**	**2θ (deg)**	**hkl**	**2θ (deg)**
ZIF-8_P	16.60	(011)	7.52	(011)	7.42	(011)	7.54
ZIF-8_5% Li	16.83	(002)	10.51	(002)	10.47	(002)	10.53
ZIF-8_10% Li	16.56	(112)	12.89	(112)	12.85	(112)	12.87
ZIF-8_20% Li	16.69	(022)	14.91	(022)	14.82	(022)	14.91
ZIF-8_5% Na	16.79	(013)	16.65	(013)	16.57	(013)	16.63
ZIF-8_10% Na	16.74	(222)	18.18	(222)	18.16	(222)	18.20
ZIF-8_20% Na	16.74						

ZIF-8_20% Li		**ZIF-8_5% Na**		**ZIF-8_10% Na**		**ZIF-8_20% Na**	
hkl	**2θ (deg)**	**hkl**	**2θ (deg)**	**hkl**	**2θ (deg)**	**hkl**	**2θ (deg)**
(011)	7.48	(011)	7.44	(011)	7.46	(011)	7.46
(002)	10.51	(002)	10.49	(002)	10.53	(002)	10.51
(112)	12.83	(112)	12.81	(112)	12.87	(112)	12.85
(022)	14.86	(022)	14.80	(022)	14.86	(022)	12.87
(013)	16.53	(013)	16.57	(013)	16.61	(013)	16.61
(222)	18.12	(222)	18.14	(222)	18.18	(222)	18.20

6.2.2. Elemental composition

The elemental compositions of pristine and in situ modified ZIF-8 samples are presented in Table 6.5. For a commercial ZIF-8 (Sigma Aldrich) elemental composition was found as follows: C: 73.8 At. %, N: 17.6 At. %, O: 1.8 At. % and Zn 6.7 At. % [178]. A comparison of the results obtained in this study with existing literature reveals similar elemental percentages for oxygen and nitrogen atoms, while notable discrepancies are observed in the percentage values of carbon and zinc atoms.

Table 6.5. *Elemental composition of ZIF-8 samples*

Sample	C	N	O	Zn
ZIF-8_P	56.55	17.53	1.45	24.47
ZIF-8_5% Li	58.35	26.67	4.49	10.49
ZIF-8_10% Li	58.47	28.13	3.61	9.79
ZIF-8_20% Li	58.26	25.94	3.74	12.07
ZIF-8_5% Na	57.99	26.52	3.58	11.91
ZIF-8_10% Na	59.68	24.75	1.95	13.61
ZIF-8_20% Na	61.67	20.87	2.85	14.61

Conversely, the percentage of nitrogen and oxygen atoms exhibited a slight increase following Li and Na treatment. This phenomenon can be attributed to the presence of NO_3 compounds, which are not removed during the post-synthesis washing procedure. In addition, the presence of lithium (Li) was not detected due to the EDS apparatus's inadequate sensitivity to detect Li atoms. In addition, the K_α and L_α lines of Na and Zn atoms exhibit proximity, with respective energies of 1.041 and 1.012 eV. Consequently, the presence of a sodium atom is also not observed.

6.2.3. FT-IR

The FT-IR transmission spectra of the ZIF-8 samples are presented in Figure 6.14. The peaks observed at 3137 cm^{-1} are attributed to the asymmetric stretching vibrations of aromatic and aliphatic C–H bonds, respectively. The prominent signal observed at 1566 cm^{-1} is attributed to the C=N stretching vibration. The cluster of absorption bands between 1300 and 1460 cm^{-1} is attributed to ring stretching vibrations, while the band at 1146 cm^{-1} is associated with aromatic C–N stretching. Moreover, the absorption bands detected at approximately 994 cm^{-1} and 759 cm^{-1} are consistent with C–N bending and C–H out-of-plane bending modes, respectively. The absorption band observed at 693 cm^{-1} corresponds to the ring out-of-plane deformation of the H-2-methylimidazolate molecule. It is noteworthy that a distinct Zn–N stretching vibration is manifested at 422 cm^{-1}, thereby confirming the coordination between zinc ions and nitrogen atoms of the methylimidazole ligands. This spectroscopic evidence indicates the successful formation of imidazolate frameworks [177, 179–181].

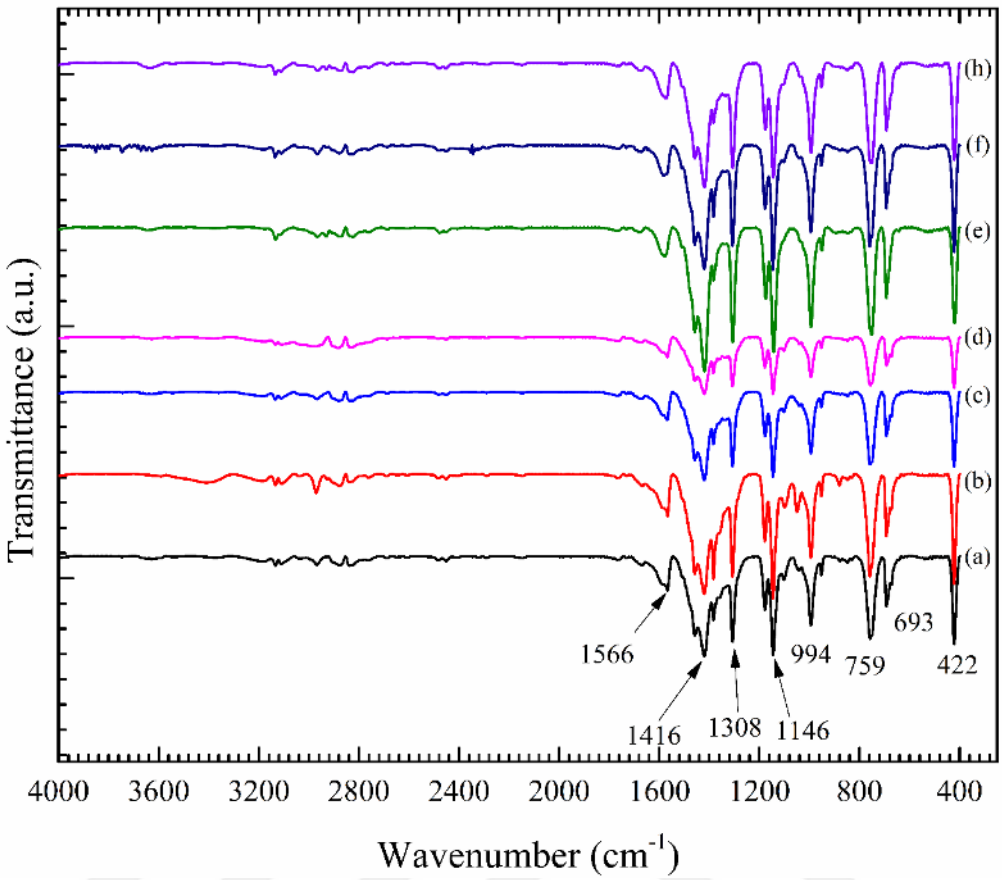

Figure 6.14. *FT-IR results of ZIF-8 samples (a): ZIF-8_P, (b): ZIF-8_5% Li, (c): ZIF-8_10% Li, (d): ZIF-8_20% Li, (e): ZIF-8_5% Na, (f): ZIF-8_10% Na, (g): ZIF-8_20% Na*

6.2.4. SEM

The SEM images in Figure 6.15 reveal the characteristic crystal morphology and surface features of the ZIF-8_P sample and its modified forms. A thorough examination of the particles reveals that they typically exhibit well-defined rhombic dodecahedral shapes. These shapes are indicative of the high crystallinity and uniformity of the synthesized material [180, 181]. Furthermore, the images suggest that the crystals are relatively uniform in size and distribution, with smooth surfaces and sharp edges. The observed morphological consistency indicates the successful synthesis of ZIF-8.

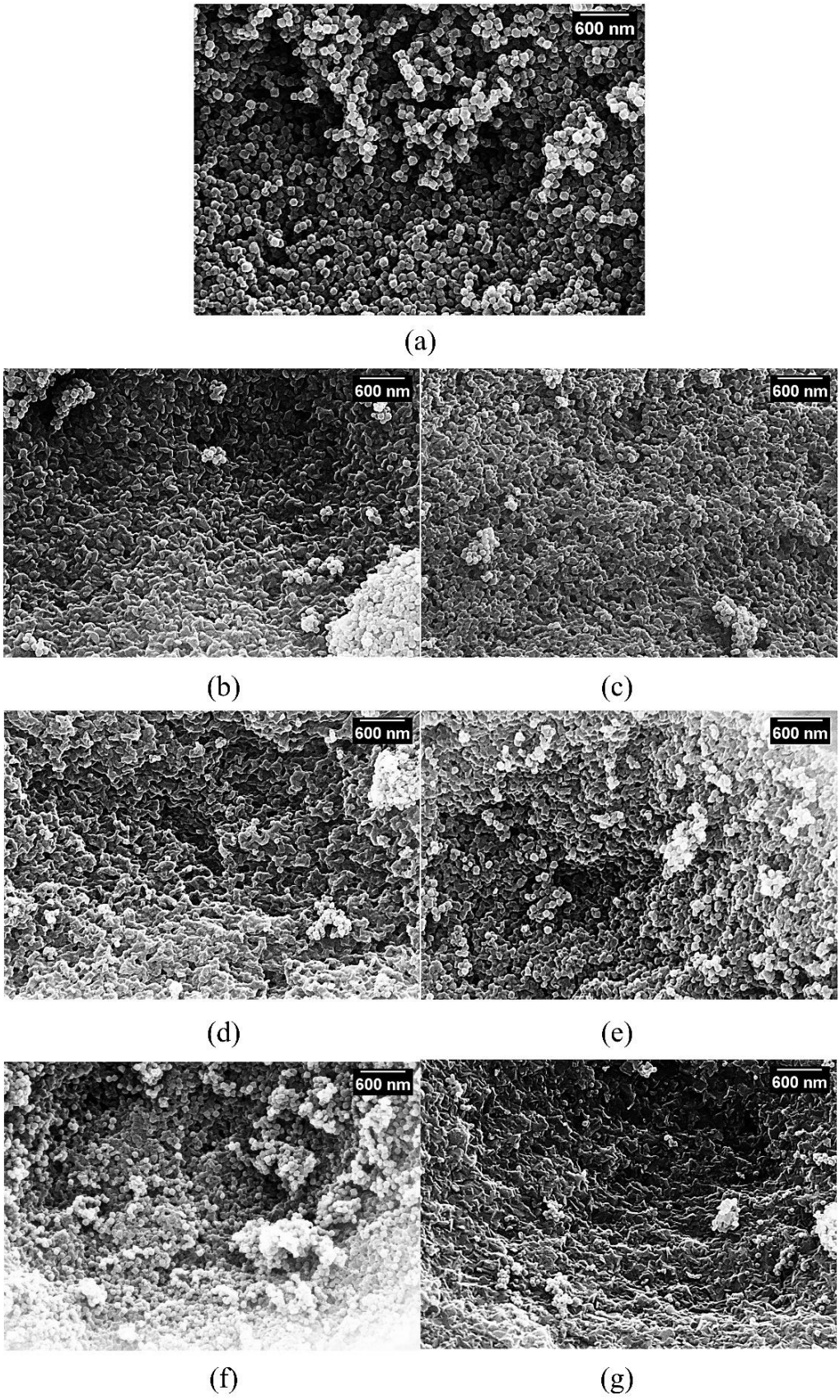

Figure 6.15. *SEM images of ZIF-8 Samples. samples (a): ZIF-8_P, (b): ZIF-8_5% Li, (c): ZIF-8_10% Li, (d): ZIF-8_20% Li, (e): ZIF-8_5% Na, (f): ZIF-8_10% Na, (g): ZIF-8_20% Na*

6.2.5. N_2 adsorption

The nitrogen adsorption isotherms of ZIF-8_P and its modified forms are illustrated in Figure 6.16. All samples exhibit Type-IV isotherms. At low relative pressures, high adsorption values show the microporous character of the ZIF-8 samples. Beyond a relative pressure of 0.1, the isotherms display a nearly flat plateau, which can be attributed to interparticle mesopores formed through the aggregation of ZIF-8 crystals [25].

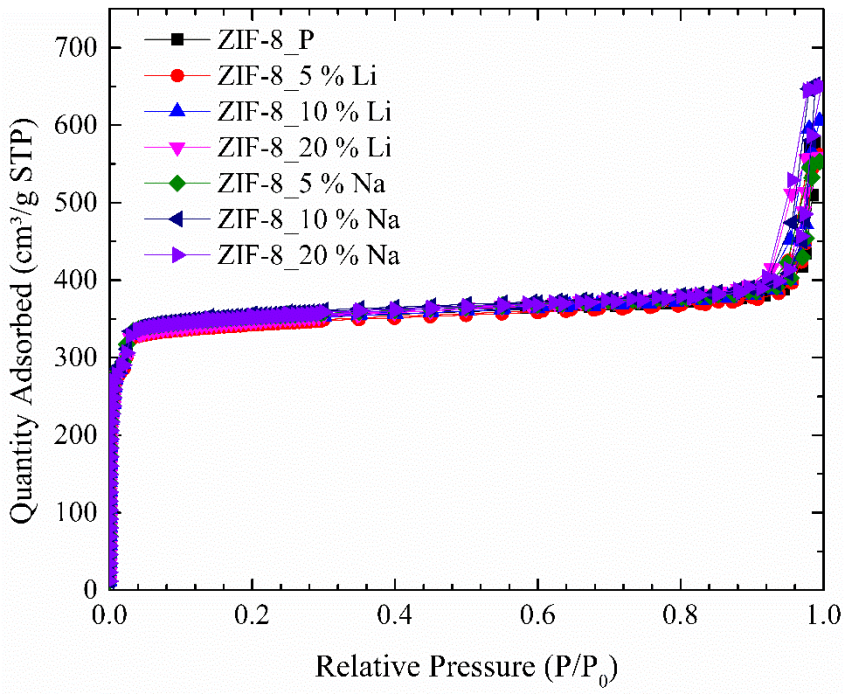

Figure 6.16. *N_2 adsorption isotherms of ZIF-8_P, ZIF-8_5% Li, ZIF-8_10% Li, ZIF-8_20% Li, ZIF-8_5% Na, ZIF-8_10% Na, ZIF-8_20% Na*

Furthermore, step-wise behavior of the adsorption isotherms was observed within the 0.003–0.04 P/P$_0$ range due to the gate opening effect, which is related to the flexible structure of ZIF-8 (Figure 6.17) [182, 183].

Table 6.6 summarizes the BET surface area and micropore properties of the *in situ* modified samples. According to the results, the presence of Li^+ ions during synthesis does not contribute positively to surface area development. By contrast, the introduction of Na^+ ions results in a slight increase in the total surface area. The specific surface areas of the ZIF-8 samples range from 1398.21 to 1472.89 $m^2.g^{-1}$, consistent with previously reported values for highly porous metal–organic frameworks [176].

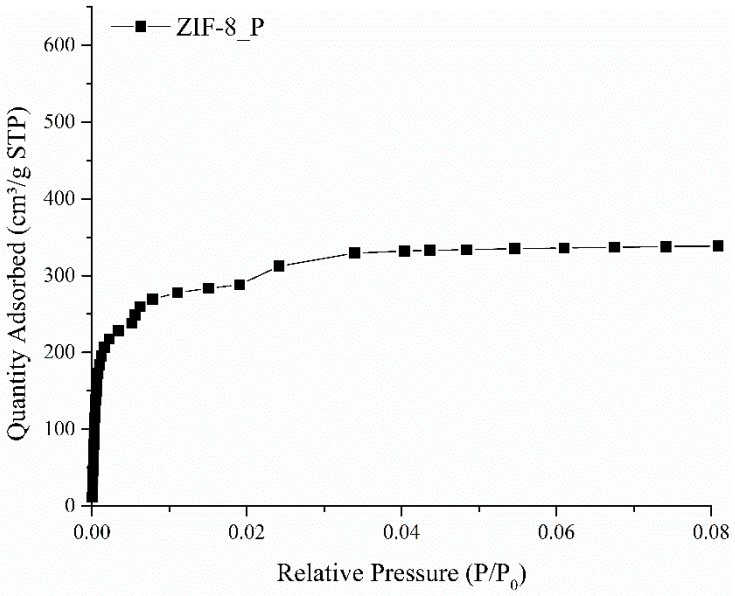

Figure 6.17. *Step-wise adsorption behavior of ZIF-8.*

Table 6.6. *Porous properties of ZIF-8 samples*

Sample	BET Specific Surface Area ($m^2.g^{-1}$)	Micropore Area ($m^2.g^{-1}$)	Micropore Volume ($cm^3.g^{-1}$)
ZIF-8_P	1431.93	1328.67	0.4932
ZIF-8_5% Li	1398.21	1255.56	0.4620
ZIF-8_10% Li	1428.88	1315.96	0.4889
ZIF-8_20% Li	1439.69	1306.15	0.4799
ZIF-8_5% Na	1464.42	1364.39	0.5021
ZIF-8_10% Na	1472.89	1365.89	0.5027
ZIF-8_20% Na	1456.13	1346.25	0.4962

6.3 Characterization of Porous SiNWs

6.3.1 SEM and EDS

SEM images of the silver-deposited samples are presented in Figure 6.18. After 10 seconds of deposition, nucleation and growth of silver nanoparticles on the sample surface is observed, with initial dimensions ranging from 20 to 100 nm. An increase in

particle size is evident with a longer deposition time; after 30 seconds, the surface exhibits near-complete coverage.

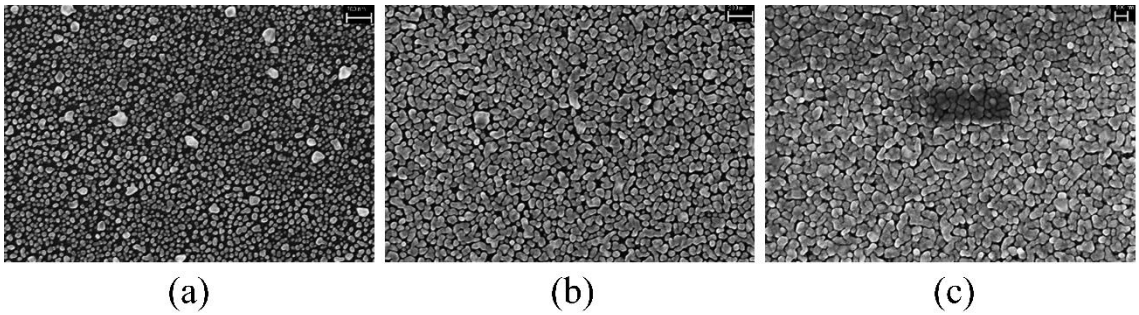

Figure 6.18. *SEM images of Ag deposited samples (a): 10 s, (b): 20 s, (c): 30 s*

Cross-sectional SEM micrographs of the etched samples are presented in Figures 6.19, 6.20 and 6.21, respectively. The SEM analysis of the PWN 1-18 series samples reveals that the etching depth varies between 2 and 10 μm. Contrary to the anticipated increase in etching depth with time, a reduction to approximately 2-4 μm was observed at etching durations exceeding one hour. In the two-step MACE process, both vertical and lateral etching, along with pore formation, occur concurrently. Consequently, the lengths of the synthesized SiNWs are directly influenced by both the vertical and lateral etch rates. When the lateral etch rate is comparable to the vertical etch rate, a decrease in nanowire dimensions with increasing etching time is observed. Conversely, prior studies have demonstrated that for Si wafers with higher resistivity, the dimensions of the obtained nanowires increase with longer etching times [184]. However, the inverse trend has been reported for Si wafers with low resistivity [136].

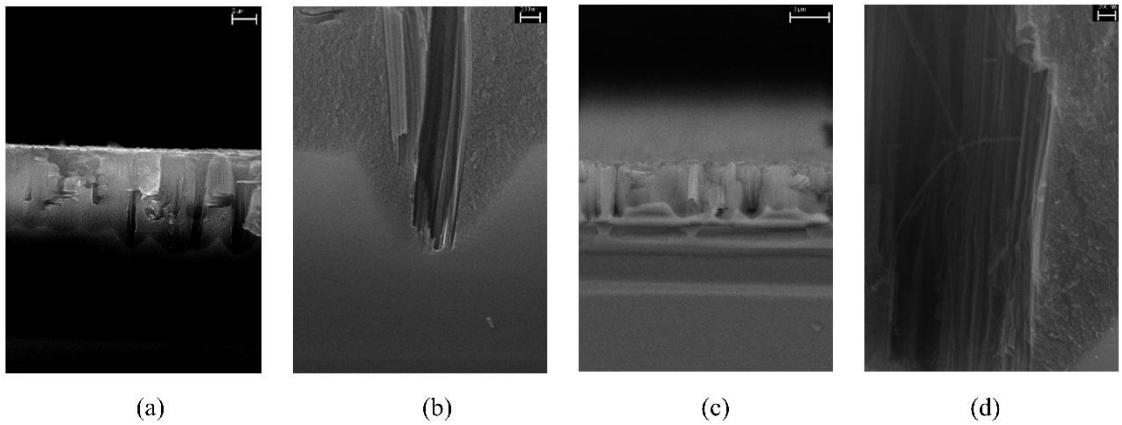

Figure 6.19. *The cross-section SEM images of samples (a): PWN-1, (b): PWN-4, (c): PWN-5, (d): PWN-6 (Scale bars: 2 μm, 200 nm, 10 μm, 200 nm, respectively)*

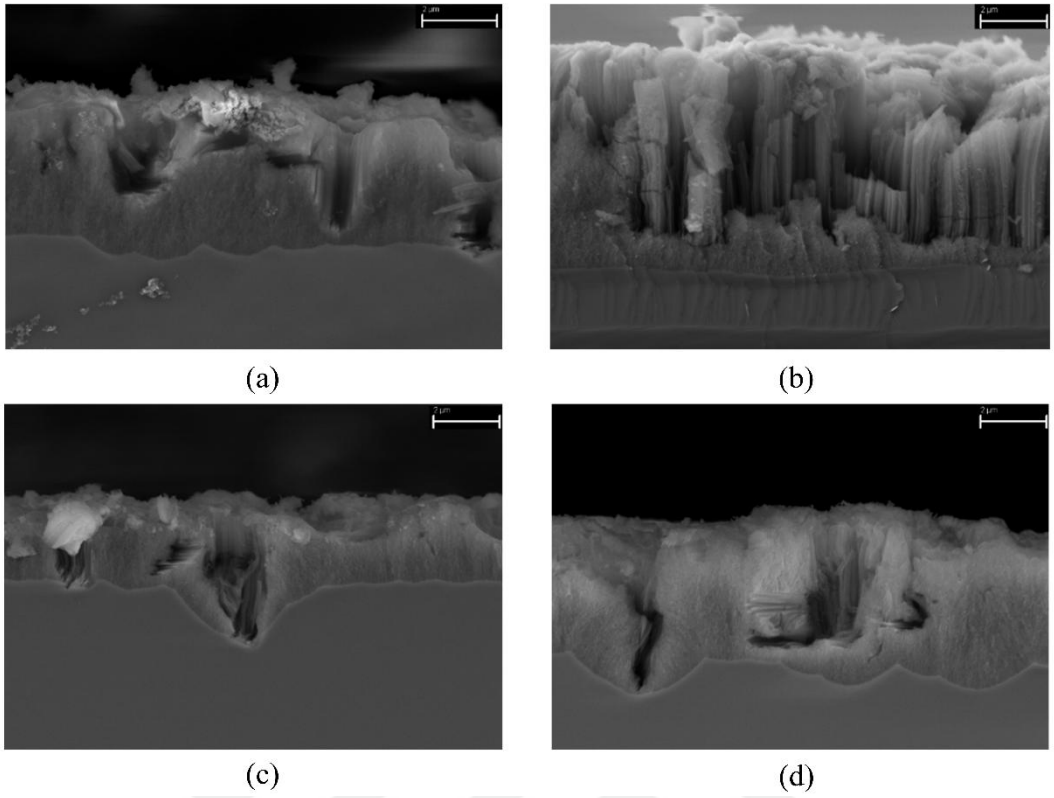

Figure 6.20. *The cross-section SEM images of samples coded (a): PWN-7, (b): PWN-9, (c): PWN-10, (d): PWN-11 (All scale bars 2 µm)*

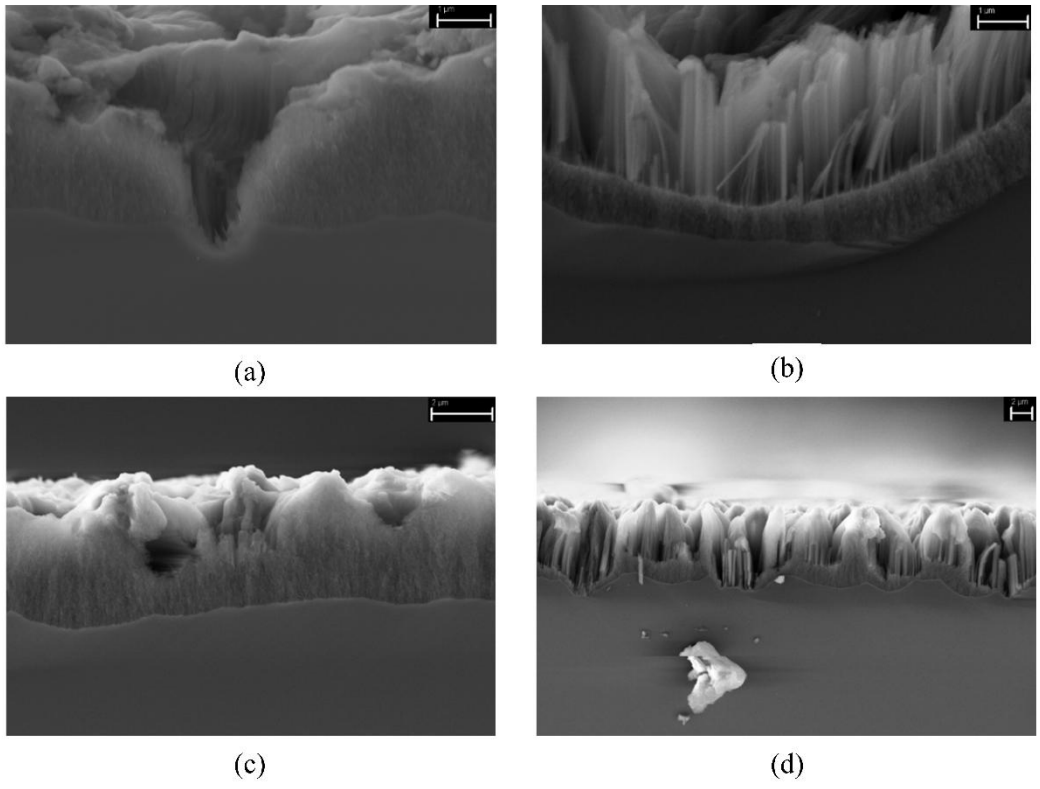

Figure 6.21. *The cross-section SEM images of samples coded (a): PWN-13, (b): PWN-15, (c): PWN-16, (d): PWN-18 (Scale bars (a)-(b) 1 µm, (c)-(d) 2 µm)*

Table 6.7. *Elemental composition (atomic %) of Au dopped PNW-A samples*

Sample	Si	O	Au
PNW-A1	88.75	11.19	0.06
PNW-A2	93.34	6.56	0.10
PNW-A3	93.38	6.47	0.13
PNW-A4	92.91	6.89	0.20

The elemental composition data obtained from EDS analysis of the Au-functionalized samples is presented in Table 6.7. The findings reveal a direct correlation between the atomic percentage of Au in the samples and both the molarity of the doping solution and the duration of the interaction. It is important to note that the quantification of Li content in the other samples was not possible due to the inherent sensitivity limitations of the EDS instrumentation that was employed [185].

6.3.2. N_2 adsorption

The nitrogen adsorption isotherms of the synthesized samples are displayed in Figure 6.22.

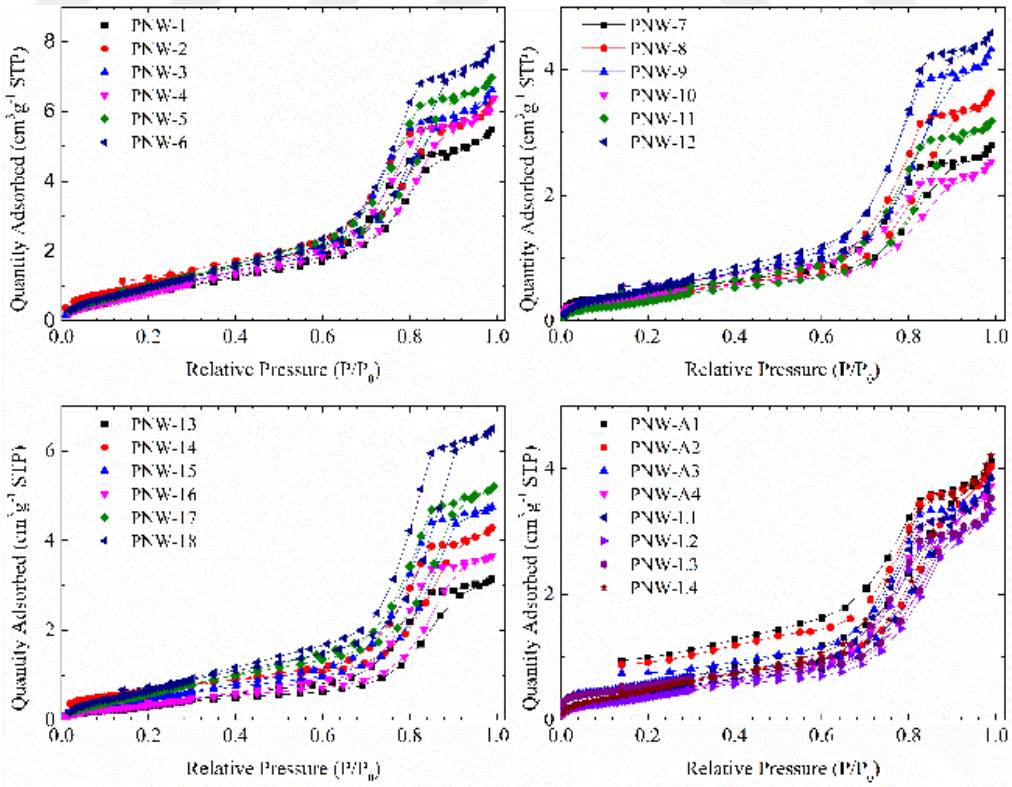

Figure 6.22 *N_2 adsorption isotherms of PNW samples*

The isotherms of all the samples are of Type-IV character, as classified by the IUPAC [85]. The initial segment of the Type-IV isotherm can be attributed to mono-multi-layer adsorption. These isotherms are frequently observed in mesoporous materials. A distinguishing characteristic of Type-IV isotherms is the presence of a hysteresis curve, which serves as an indicator of the underlying mechanisms. The hysteresis curve observed during desorption is due to the fact that gas condenses in the mesopores during adsorption and cannot be desorbed immediately as the pressure decreases. The hysteresis curve observed in the isotherms, designated as type H1, is commonly associated with porous materials that possess well-defined cylindrical pore channels [25].

Table 6.8. *Porous properties of of PNW1-18*

Sample	BET Specific Surface Area ($m^2 \cdot g^{-1}$)	Sample	BET Specific Surface Area ($m^2 \cdot g^{-1}$)	Sample	BET Specific Surface Area ($m^2 \cdot g^{-1}$)
PNW-1	3.93	PNW-7	1.89	PWN-13	0.93
PNW-2	4.55	PNW-8	2.08	PWN-14	2.25
PNW-3	4.59	PNW-9	1.78	PWN-15	2.24
PNW-4	4.48	PNW-10	2.39	PWN-16	1.07
PNW-5	5.44	PNW-11	1.04	PWN-17	3.5
PNW-6	4.78	PNW-12	2.34	PWN-18	3.75

Table 6.8 summarizes the BET specific surface area values of the PWN 1–18 sample series, which were found to vary between 0.9 and 5.44 $m^2.g^{-1}$. A clear decline in surface area was observed as the etching time increased. This trend is likely the result of reduced etching depth and consequent shrinkage of the porous region, as confirmed by scanning electron microscopy (SEM) imaging. The BET surface area values of the Au- and Li-functionalized samples are provided separately in Table 6.9.

Table 6.9. *Porous properties of of PNW-A and PNW-L series*

Sample	BET Specific Surface Area ($m^2 \cdot g^{-1}$)	Sample	BET Specific Surface Area ($m^2 \cdot g^{-1}$)
PNW-A1	3.15	PNW-L1	1.45
PNW-A2	2.73	PNW-L2	1.88
PNW-A3	2.31	PNW-L3	2.16
PNW-A4	2.08	PNW-L4	2.47

In the Au-doped PNW-A sample series, an inverse relationship was observed between the (BET) surface area and the molarity of the Au precursor, as well as the interaction time. This indicates a progressive reduction in surface area with increasing doping conditions. This behavior is likely due to the aggregation of Au atoms, which tend to block pore entrances as their concentration increases. In contrast, Li-doped samples exhibited the opposite trend, with surface areas increasing as a function of Li incorporation. Analysis of pore size distribution revealed that most of the synthesized samples have pore diameters ranging from 2 to 40 nm, which is consistent with mesoporous materials (Figure 6.23).

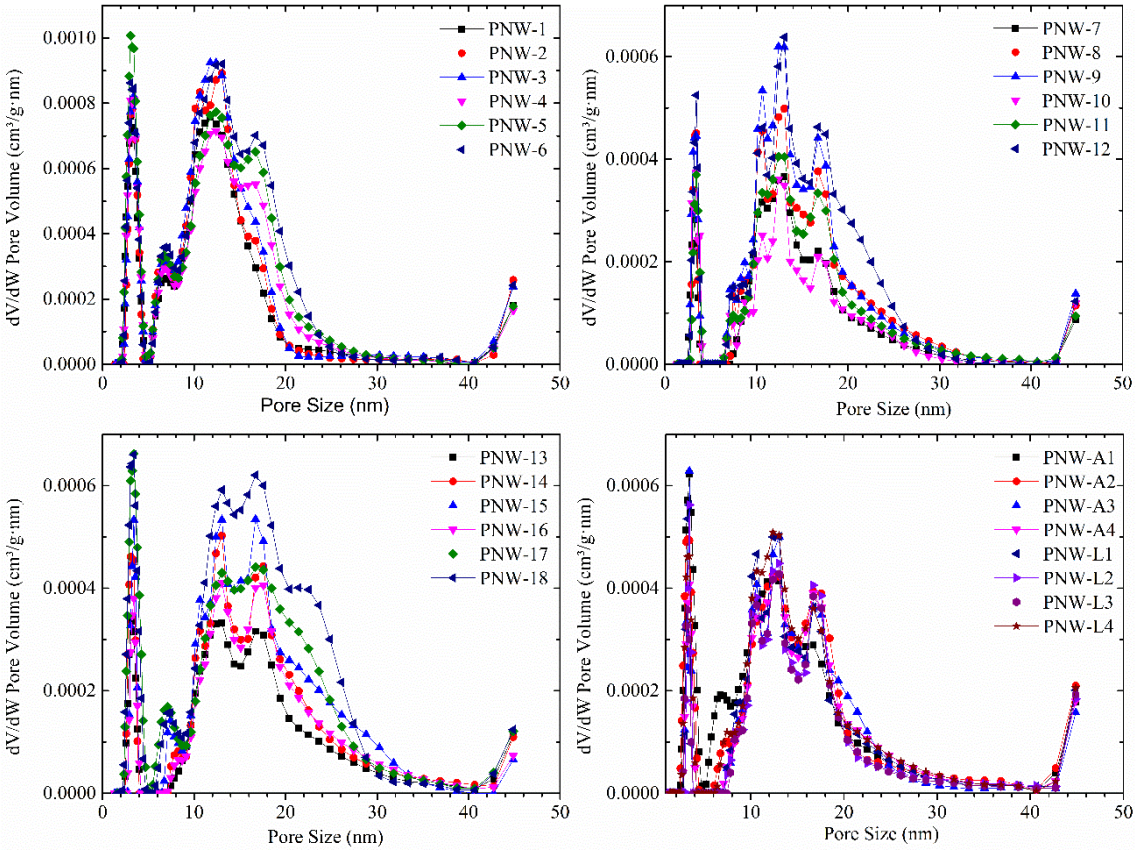

Figure 6.23 *Pore size distributions of PNW samples*

6.4. H_2 adsorption

The hydrogen adsorption isotherms of the raw CLN, H-CLN, and 0.5-Li-CLN samples are presented in Figure 6.24. At a cryogenic temperature of 77 K and a pressure of 113 kPa, the hydrogen uptake capacities of the clinoptilolite samples were found to be in the following ascending order: CLN < 0.5-Ca-CLN < 0.5-Na-CLN < 0.1-Ca-CLN < 0.1-Na-CLN < 0.5-K-CLN < 0.1-Mg-CLN < 0.5-Cu-CLN < 0.1-K-CLN ≈ 0.5-Mg-CLN < 0.1-Ag-CLN < 0.1-Cu-CLN < 0.1-Li-CLN < 0.5-Ag-CLN ≈ 0.1-Ni-CLN < 0.5-Ni-CLN < H-CLN < 0.5-Li-CLN (Table 6.10).

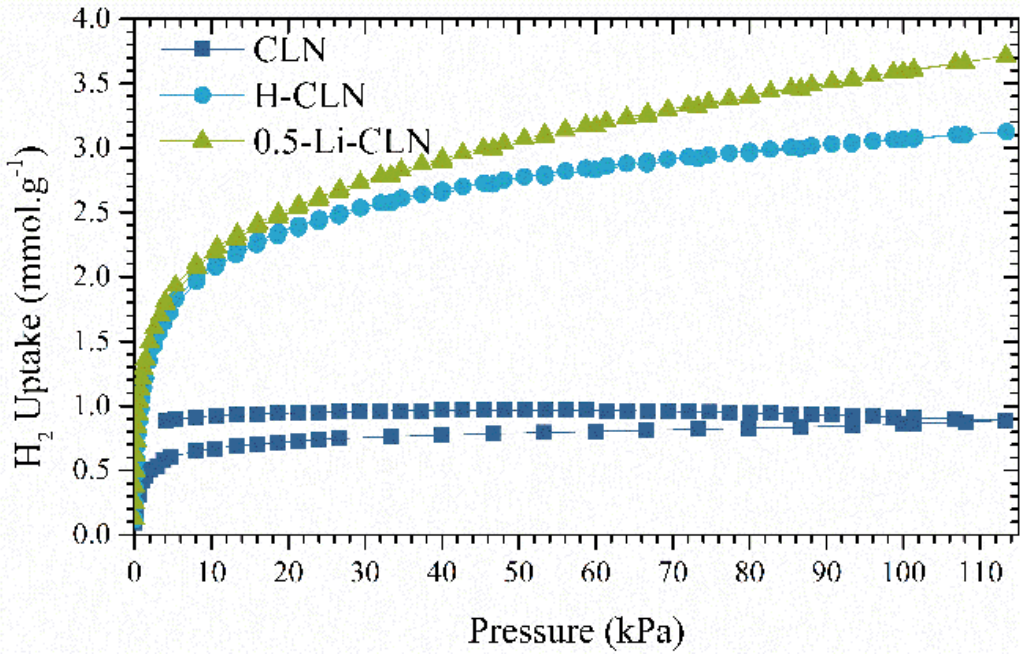

Figure 6.24. *H_2 Adsorption isotherms of raw CLN, H-CLN and 0.5-Li-CLN samples.*

Table 6.10. *H_2 Adsorption date of CLN samples*

Sample	H_2 Uptake		Sample	H_2 Uptake	
	wt %	mmol.g^{-1}		wt %	mmol.g^{-1}
Raw-CLN	0.257	1.273	0.5-Li-CLN	0.749	3.713
H-CLN	0.705	3.497	0.1-Na-CLN	0.602	2.988
0.1-Ni-CLN	0.670	3.323	0.5-Na-CLN	0.584	2.895
0.5-Ni-CLN	0.703	3.488	0.1-K-CLN	0.614	3.045
0.1-Cu-CLN	0.619	3.073	0.5-K-CLN	0.609	3.022
0.5-Cu-CLN	0.612	3.038	0.1-Ca-CLN	0.588	2.919
0.1-Ag-CLN	0.621	3.082	0.5-Ca-CLN	0.579	2.873
0.5-Ag-CLN	0.650	3.225	0.1-Mg-CLN	0.611	3.029
0.1-Li-CLN	0.636	3.153	0.5-Mg-CLN	0.614	3.045

In this investigation, the H_2 adsorption capacity of H-CLN was determined to be 0.705 wt%, which surpasses that of clinoptilolite from the same geographical origin when exchanged with 2.0 M HNO_3 (0.48 wt%) [30] or 1.0 M HCl (0.48 wt%) [29], while a sample modified with 0.5 M HNO_3 at 80 °C for 2 h exhibited a capacity of approximately 0.65 wt% [186]. For H-type zeolites, the concentration of hydroxyl (OH) groups is a crucial factor that influences the characteristics of hydrogen adsorption. The affinity of OH groups for hydrogen molecules is mediated by hydrogen bonding interactions [187, 188]. The population density of OH groups in zeolites is inversely proportional to the SiO_2/Al_2O_3 ratio. Consequently, acid activation using solutions such as HCl and HNO_3 typically leads to dealumination and a concomitant reduction in the total number of OH groups and, hence, H_2 adsorption capacity [186, 189].

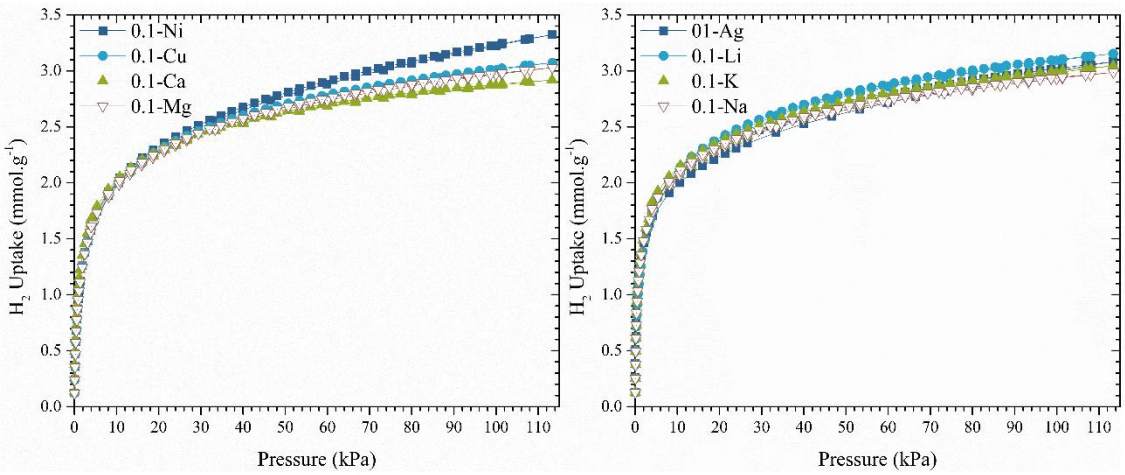

Figure 6.25. *H_2 Adsorption isotherms of cation-exchanged CLN samples with 0.1 M solutions*

The observed variations in the hydrogen adsorption capacities of cation-exchanged samples (Figures 6.25 and 6.26) are contingent upon multiple factors, including the cation selectivity of clinoptilolite, the effective ionic radius of the incorporated cation, the extent of cation doping, and the specific location of these cations within the channel system. The polarizing power of extra-framework cations influences the adsorption mechanism of molecular hydrogen [189]. However, this property of exchangeable cations is also modulated by the structural framework of the adsorptive material [190, 191]. The ionic radii of Na^+, K^+, Ag^+, and Li^+ cations are reported as 0.116, 0.152, 0.126, and 0.090 nm, respectively [192]. Of all the cation-exchanged clinoptilolite samples, the 0.5-Li-CLN sample exhibited the highest hydrogen adsorption capacity, exceeding even that of the H-

CLN sample. This superior performance is due to the small size of the Li^+ cation and its consequently stronger interaction potential with the H_2 molecule compared to other monovalent cations [193]. Exchanging cations with a 0.5 M $LiNO_3$ solution during sample preparation resulted in the complete removal of Na^+ cations and a significant reduction in the proportion of Ca^{2+} cations that could occupy the M(1) site in channel A and the M(2) site in channel B. Furthermore, substantially removing Mg^{2+} cations from the M(4) region in the center of channel A in this sample also prevented potential blockage within the channels.

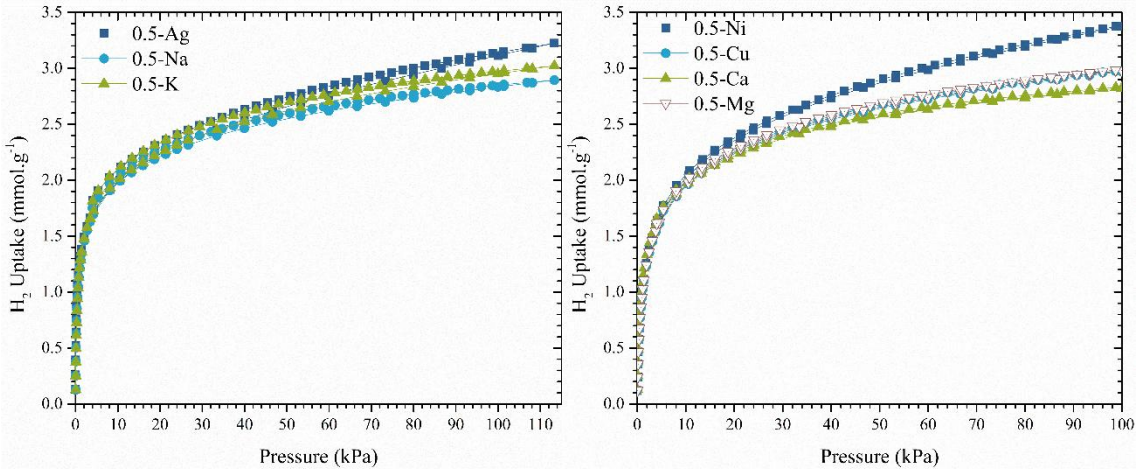

Figure 6.26. *H_2 Adsorption isotherms of cation exchanged CLN samples with 0.5 M solutions*

Of the cation-exchanged clinoptilolites investigated, the 0.5-Li-CLN sample had the highest hydrogen adsorption capacity (0.749 wt%), exceeding that of the H-CLN sample. This superior performance is due to the strong interaction potential between the Li^+ ion and the H_2 molecule [193]. The polarisation strength of cationic species directly influences the adsorption of hydrogen molecules at cationic sites within zeolites [194]. However, the coordination environment of these cationic species with framework oxygen atoms can modulate hydrogen–cation interactions. Theoretical investigations based on Density Functional Theory (DFT) have demonstrated that adsorption strength is directly correlated with the binding affinity of extra-framework cations to the zeolite framework [195, 196].

Notably, the Li^+ cation was found to occupy the M(4) site within channel A preferentially, exhibiting reduced coordination with the framework oxygen atoms. Taking into account the relatively unperturbed polarization strength, favorable ionic radius and

positioning that mitigate pore blockage, the L^{i+}-modified sample demonstrated the highest hydrogen adsorption capacity [98, 197]. A confluence of research findings has consistently corroborated the superior efficacy of the Li^+ cation for enhancing hydrogen adsorption [29, 198, 199]. For example, Kubo et al. documented that lithium-exchanged mordenite (MOR) and faujasite (FAU) zeolites had higher hydrogen adsorption capacities than their sodium-exchanged (Na^+) counterparts [189]. However, the present study highlights that the hydrogen uptake capacity of zeolitic materials is not solely dependent on the incorporated cationic species, but is also intrinsically linked to the zeolite's structural framework [200]. The Na^+-doped CLN samples had lower adsorption capacities than all the other cation-doped forms of CLN. The increased concentration of Na^+ within channel A, along with the continued presence of K^+, resulted in restricted channel accessibility and consequently the lowest hydrogen uptake. Comparative analysis of Ag^+, Cu^{2+} and Ni^{2+}-doped forms reveals that Ni^{2+}-doped CLN samples exhibited the highest adsorption capacity in this group. This can be attributed to the location of the Ni^{2+} ion within the channels of Ni^{2+}-exchanged CLNs derived from protonated forms, which prevents pore blockage effectively [102]. The hydrogen adsorption characteristics of Ni^{2+}-exchanged zeolites depend on the framework. For example, Mg^{2+}-exchanged zeolite-X demonstrated a higher adsorption capacity than Ni^{2+}-exchanged forms in one study (contrary to the findings of the present investigation) [201], while another study reported superior hydrogen adsorption for Ni-doped Zeolite-X compared to the Rh-doped form [202]. Among the samples examined in this study, 0.5-Li-CLN (0.726 wt%) exhibited the highest hydrogen uptake, whereas CLN displayed the lowest hydrogen adsorption capacity. This observation suggests that the pretreatment protocol used to produce the H^+ form (H-CLN), the initial material before cation exchange, is effective in removing most of the exchangeable cations from the structure. This facilitates pore opening and improves gas adsorption capacity. The hydrogen adsorption capacity of the 0.5-Li-CLN sample (0.726 wt%) exceeds that of clinoptilolite originating from the same geographical area that has been exchanged with 1.0 M $LiNO_3$ (0.555 wt%) [29], activated with 2.0 M HNO_3 (0.482 wt%) [30], and activated with 0.2 M NaOH (26.47 $cm^3\ g^{-1}$) [36]. However, it remains lower than that of chabazite treated with 1.0 M $LiNO_3$ (0.944 wt%) [29], NaY (1.16 wt%) [203], zeolite-X (1.60 wt%) [204] and Li-LSX (1.50 wt%) [34]. Although natural clinoptilolite-type materials have an inherently lower hydrogen adsorption capacity than more costly synthetic zeolites, their abundance in nature and the

significant enhancement of their gas adsorption properties through modified processes make them advantageous for hydrogen storage applications.

The hydrogen H_2 adsorption isotherms of the ZIF-8 samples are presented in Figure 6.27 and Table 6.11. The hydrogen uptake capacities of the ZIF-8 samples exhibit a dependence on their Brunauer-Emmett-Teller (BET) specific surface area and micropore area. The uptake capacities followed the ascending order: ZIF-8_20% Na < ZIF-8_10% Li < ZIF-8_20% Li < ZIF-8_5% Li < ZIF-8_P < ZIF-8_5% Na < ZIF-8_10% Na. However, within the margin of experimental error, the hydrogen uptake capacities of these samples are approximately similar, with the exception of ZIF-8_20% Na, ZIF-8_10% Li, and ZIF-8_20% Li.

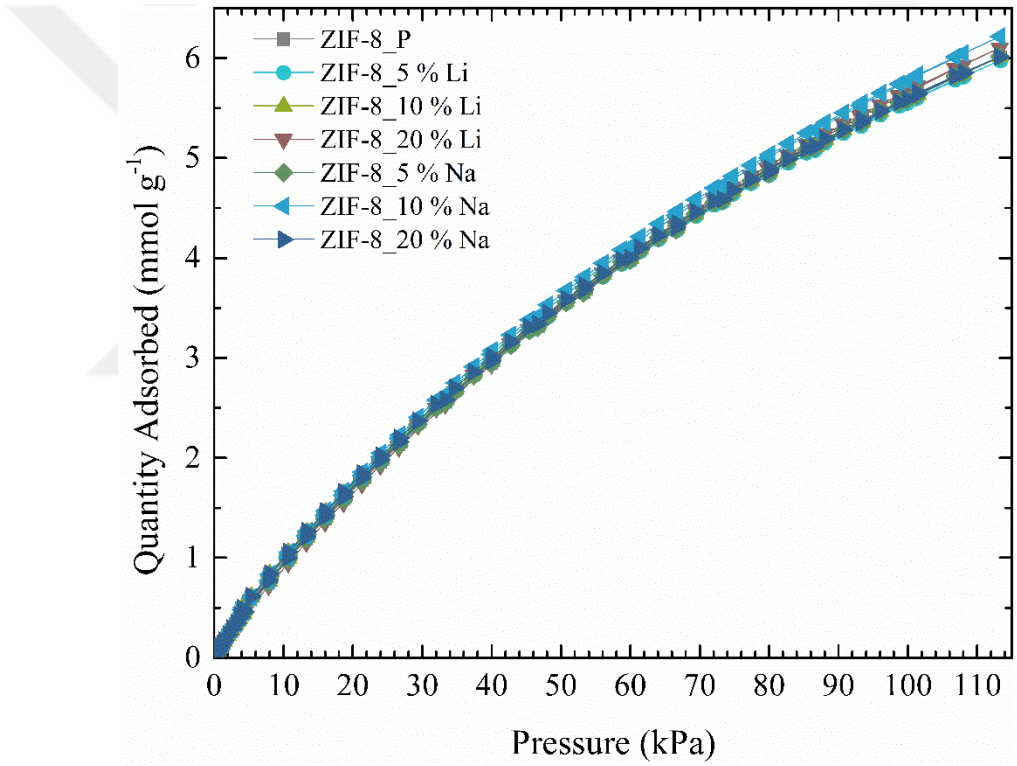

Figure 6.27. *H_2 Adsorption isotherms of ZIF-8 samples*

These findings suggest that the presence of Li^+ ions in the synthesis solutions does not have a positive influence on the hydrogen adsorption properties of the synthesised ZIF-8 materials. Furthermore, the incorporation of Na^+ ions appear to slightly enhance the hydrogen storage capacity of ZIF-8. Several studies in the literature have reported on the hydrogen adsorption performance of ZIF-8 under various conditions. For example, Park et al. [205] reported a hydrogen uptake of 3.1 wt% for ZIF-8 at 77 K and 55 bar.

Similarly, Zhou et al. found hydrogen adsorption capacities of 3.3 wt% at 77 K and 30 bar and 0.13 wt% at ambient temperature and 60 bar [206]. Modified ZIF-8 structures have also been investigated to enhance hydrogen storage capacity. For example, H_2O-pretreated ZIF-8 samples exhibited a capacity of 0.23 wt% at 50 bar [40], while Mg-decorated ZIF-8 nanoparticles demonstrated a notably higher capacity of 5.3 wt% [207]. Additionally, Pd-functionalised ZIF-8 samples exhibited a 30% increase in hydrogen uptake compared to pristine ZIF-8 [208]. More recently, Bose et al. reported a hydrogen storage capacity of 3.13 wt% for unmodified ZIF-8 at 77 K and 50 bar [209]. Furthermore, Balderas-Xicohtencatl et al. observed that ZIF-8 pellets exhibited hydrogen uptake values ranging from 2.64 to 2.82 wt% at 25 bar and 77 K [210].

Table 6.11. *H_2 Adsorption data of ZIF-8 samples*

Sample	H_2 Uptake	
	wt%	mmol.g^{-1}
ZIF-8_P	1.151	5.776
ZIF-8_5% Li	1.148	5.761
ZIF-8_10% Li	1.134	5.690
ZIF-8_20% Li	1.137	5.705
ZIF-8_5% Na	1.152	5.781
ZIF-8_10% Na	1.176	5.903
ZIF-8_20% Na	1.120	5.618

The hydrogen adsorption capacities of the PNW-A and PNW-L samples whose surfaces were functionalized with Au and Li are presented in Table 6.12. Examination of the hydrogen adsorption isotherms (Figure 6.28) revealed the absence of desorption curve closure in all samples. The hydrogen adsorption amounts for the samples ranged from 0.027 to 0.042 mmol g^{-1}. These low adsorption values observed can be attributed to the limited specific surface area and porosity of the synthesized materials. The hydrogen adsorption-desorption isotherms of the synthesized samples belonging to the PWN A and L series reveal a consistent adsorption behavior across all samples. However, the desorption branch of the isotherms indicates that the adsorbed hydrogen is not recoverable through pressure reduction. This phenomenon can be attributed to the fact that hydrogen

undergoes not only surface adsorption on the Si material but also subsurface penetration, reaching the underlying layers [211, 212].

Table 6.12. *H_2 Adsorption data of PNW-A and PNW-L samples*

Sample	H_2 Uptake		Sample	H_2 Uptake	
	wt%	mmol.g^{-1}		wt%	mmol.g^{-1}
PNW-A1	0.007	0.035	PNW-L1	0.005	0.027
PNW-A2	0.008	0.042	PNW-L2	0.006	0.028
PNW-A3	0.006	0.030	PNW-L3	0.008	0.042
PNW-A4	0.006	0.031	PNW-L4	0.007	0.036

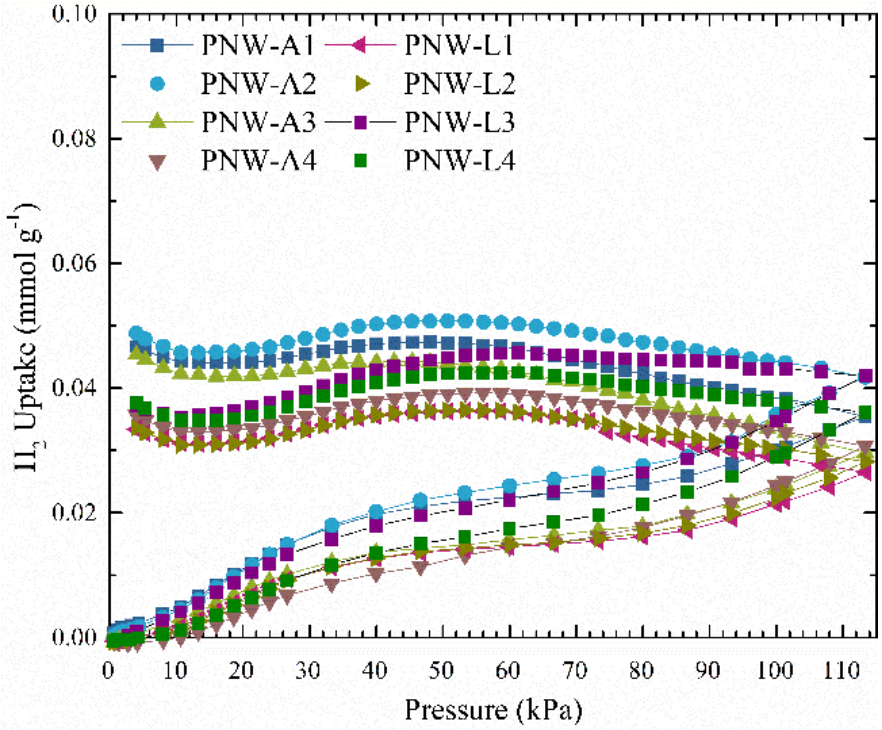

Figure 6.28. *H_2 Adsorption isotherms of PNW-A and PNW-L samples*

To the best of our knowledge, this study is the first to demonstrate molecular hydrogen storage via physisorption in porous silicon nanowires (SiNWs) at 113 kPa and 77 K. Due to the unique experimental conditions and physisorption mechanism, direct quantitative comparisons with existing literature data could be misleading. Nevertheless, to provide context, it is worth noting that lithium-dispersed silica nanotubes have been reported to store hydrogen at capacities of 0.15 wt% (approximately 0.75 mmol g^{-1}) and 0.29 wt% (approximately 1.44 mmol g^{-1}) at 77 K under 4.5 MPa pressure [52]. Other

studies have also explored hybrid materials incorporating porous silicon. For instance, a porous silicon nanowire (SiNW) – lithium hydride (LiH) alloy demonstrated a hydrogen uptake of 3.95 wt% (approximately 20.40 mmol g^{-1}) at approximately 4 MPa and 673 K [49], whereas a nanoporous silicon–single-walled carbon nanotube composite exhibited a notably lower capacity of 0.0793 mmol g^{-1} (approximately 0.016 wt%) [53]. By comparison, the adsorption capacities observed for the PNW-A2 and PNW-L3 samples in this study (0.042 mmol g^{-1}) are lower than those reported for silicon nanoparticles (approximately 11.42 mmol g^{-1}) [48], ball-milled porous silicon (approximately 59.43 mmol g^{-1}) [46] and electrochemically anodized bulk silicon (approximately 0.50 mmol g^{-1}) [50].

7. CONCLUSION

This thesis investigates the structural and hydrogen adsorption characteristics of three distinct porous materials: a natural zeolite clinoptilolite (CLN), in situ modified zeolitic imidazolate framework (ZIF-8), and gold- and lithium-doped porous silicon nanowires (SiNWs). The cation exchange procedure was applied to the hydrogen form of CLN, which was synthesized via thermal treatment following ammonium exchange. Pristine and in situ modified samples of ZIF-8 were obtained via solvo-thermal method. The Metal Assisted Chemical Etching (MACE) procedure was utilized in the synthesis of gold and lithium-doped porous SiNWs. A number of analytical methods were used to describe each substance, including X-ray diffraction, X-ray fluorescence, and scanning electron microscopy. The materials were then evaluated for their hydrogen physisorption behavior at cryogenic temperatures and atmospheric pressure.

The conversion of clinoptilolite to its protonated form (H-CLN) and subsequent doping with various mono- and divalent cations (e.g. Ag^{+}, Na^{+}, K^{+}, Li^{+}, Ni^{2+} and Cu^{2+}) has been demonstrated. When meticulously regulated, the cation-exchange process has been shown to have no detrimental effect on the structural integrity or chemical composition of the parent zeolite. XRD, XRF and FT-IR analyses confirmed that crystallinity and minimal dealumination were preserved post-treatment. A significant increase in the BET surface area was observed, with a rise from 35.68 $m^2.g^{-1}$for the raw CLN to 259.18 $m^2.g^{-1}$ for the H-CLN. This highlights the effectiveness of acid treatment in activating the zeolitic framework. Among the cation-doped variants, 0.5-Li-CLN exhibited the greatest hydrogen adsorption capacity, approximately three times higher than that of the initial CLN. This improvement can be attributed to the small ionic radius and favorable positioning of Li^{+} ions within the M(4) region of the zeolite's A-channel. This effectively impedes pore blockage and optimizes the accessible surface area. These findings corroborate the approach of obtaining H^{+} forms followed by targeted cation exchange as a promising way to improve the physisorption-based hydrogen storage capacity of natural zeolites.

At the same time, the hydrogen storage potential of ZIF-8 and its in situ modified derivatives was investigated, focusing on maintaining framework integrity while manipulating porosity. XRD analyses confirmed that the crystalline structure of ZIF-8 remained largely unchanged upon sodium doping. However, SEM imaging revealed significant morphological deterioration, likely due to the destabilizing effects of the

incorporation of the dopant. Of the synthesized variants, ZIF-8_10% Na exhibited the greatest BET surface area and hydrogen adsorption capacity, achieving 1.176 wt% at 113 kPa and 77 K. This value makes ZIF-8_10% Na a highly promising candidate for low-pressure hydrogen storage applications. Given that these measurements were conducted under moderate pressure conditions, it is reasonable to hypothesize that the storage capacity could increase favorably under higher pressures. Consequently, the findings indicate the necessity for additional experimentation under augmented experimental conditions to completely realize the material's potential in practical storage systems.

Finally, porous silicon nanowires (SiNWs) fabricated via a two-step metal-assisted chemical etching (MACE) method and subsequently doped with Au and Li were evaluated. Despite the successful attainment of a porous morphology characterized by nanowire lengths ranging from 2 to 10 μm, the BET surface areas remained modest, with a maximum value of 5.44 $m^2.g^{-1}$. Furthermore, the hydrogen storage capacities exhibited limitations, with a range from 0.027 to 0.042 $mmol.g^{-1}$. The minimal improvements observed with metal doping suggest that neither Au nor Li significantly enhanced the physisorption behavior at the tested conditions. However, the findings emphasize the potential of Si-based nanostructures, contingent upon the optimization of fabrication parameters, specifically etching depth and stability. In subsequent studies, the substitution of MACE with a more regulated etching strategy and the exploration of alternative dopants may yield enhanced outcomes.

In summary, this study has demonstrated the varying degrees of hydrogen storage performance across different porous materials. Cation-exchanged zeolites and Na and Li modified ZIF-8s demonstrated considerable potential under low-pressure conditions, while porous SiNWs necessitate additional material engineering to achieve viability. Further research is required to investigate the practical potential of these materials when exposed to elevated pressures of approximately 80 MPa. In addition, the theoretical modelling of these materials with quantum mechanical level theories and the simulation of adsorption processes with grand canonical Monte Carlo simulations will contribute to the exploration of new materials for hydrogen storage applications.

REFERENCES

[1] Wilson, S. S. (1981). Sadi Carnot: technik und theorie der dampfmaschine. *Spektrum Wiss.*, 10, 98–109.

[2] Houghton, J. (2005). Global warming. *Reports on Progress in Phys.*, 68, 1343.

[3] Mudge, F. B. (1997). The development of the 'greenhouse' theory of global climate change from Victorian times. *Weather*, 52, 13–17.

[4] Abas, N., Kalair, A., and Khan, N. (2015). Review of fossil fuels and future energy technologies. *Futures*, 69, 31–49.

[5] Smalley, R. E. (2005). Future global energy prosperity: the terawatt challenge. *MRS Bulletin*, 30, 412–417.

[6] Weisz, P. B. (2004). Basic choices and constraints on long-term energy supplies. *Phys. Today*, 57, 47–52.

[7] Grätzel, M. (2005). Solar energy conversion by dye-sensitized photovoltaic cells. *Inorganic Chem.*, 44, 6841–6851.

[8] Harjanne, A. and Korhonen, J. M. (2019). Abandoning the concept of renewable energy. *Energy Policy*, 127, 330–340.

[9] Turkenburg, W. C. and Faaij, A. (2000). Renewable energy technologies. *UNDP/UNDESA/WEC: Energy and the Challenge of Sustainability. World Energy*.

[10] Arutyunov, V. S. and Lisichkin, G. V. (2017). Energy resources of the 21st century: problems and forecasts. can renewable energy sources replace fossil fuels. *Russian Chem. Rev.*, 86, 777.

[11] Yu, K. and Chen, J. (2009). Enhancing solar cell efficiencies through 1-D nanostructures. *Nanoscale Res. Lett.*, 4, 1–10.

[12] Schlapbach, L. (2002). Hydrogen as a fuel and its storage for mobility and transport. *MRS Bull*, 27, 675–679.

[13] Niaz, S., Manzoor, T. and Pandith, A. H. (2015). Hydrogen storage: materials, methods and perspectives. *Renew. Sust. Energy, Rev.*, 50, 457–469.

[14] Kaur, M. and Pal, K. (2019). Review on hydrogen storage materials and methods from an electrochemical viewpoint. *J. Energy. Storage.*, 23, 234–249.

[15] Züttel, A. (2004). Hydrogen storage methods. *Naturwissenschaften*, 91, 157–172.

[16] Lu, K. (2014). *Materials in energy conversion, harvesting, and storage*. John Wiley & Sons.

[17] Goater, A., Hay, R., Hill, J., Mackenzie, C., Wyatt, N., Abraham, S., Taylor, S. (2018). *Hydrogen in a low-carbon economy*. Committee on Climate Change.

[18] Midilli, A., Ay, M., Dincer, I., Rosen, M. A. (2005). On hydrogen and hydrogen energy strategies: I: current status and needs. *Renew. Sust. Energ. Rev.*, 9, 255–271.

[19] Norbeck, J. M., Barth, M. J., Farrell, J. A., Heffel, J. W. (1997). *Development and evaluation of a hydrogen fuel power plant for a hybrid electric vehicle—phase II*. Final report to the South Coast Air Quality Management District under contract 95073.

[20] Broom, D. P., Webb, C. J., Hurst, K. E., Parilla, P. A., Gennett, T., Brown, C. M., Zacharia, R., Tylianakis, E., Klontzas, E., Froudakis, G. E., Steriotis, Th. A., Trikalitis, P. N., Anton, D. L., Hardy, B., Tamburello, D., Corgnale, C., van Hassel, B. A., Cossement, D., Chahine, R., Hirscher, M. (2016). Outlook and challenges for hydrogen storage in nanoporous materials. *Appl. Phys. A*, 122, 151.

[21] Demirocak, D.E. (2017). Hydrogen storage technologies. Nanostructured Materials for Next-Generation Energy Storage and Conversion: Hydrogen Production, Storage, and Utilization 117–142.

[22] Sandi, G. (2004). Hydrogen storage and its limitations. *Electrochem. Soc. Interface.,* 13, 40–44.

[23] Tarasov, B. P., Fursikov, P. V., Volodin, A. A., Bocharnikov, M. S., Shimkus, Y. Y., Kashin, A. M., Yartys, V. A., Chidziva, S., Pasupathi, S., Lototskyy, M. V. (2021). Metal hydride hydrogen storage and compression systems for energy storage technologies. *Int. J. Hydrogen Energy,* 46, 13647–13657.

[24] Hiemenz P.C. and Rajagopalan R. (2016). *Principles of colloid and surface chemistry, revised and expanded.* CRC Press.

[25] Lowell, S., Shields, J.E., Thomas, M.A., Thommes, M. (2004). *Characterization of porous solids and powders: Surface area, pore size and density.* Springer Netherlands, Dordrecht

[26] Ipek, B., Pollock, R. A., Brown, C. M., Uner, D., Lobo, R. F. (2018). H_2 adsorption on Cu(I)-SSZ-13. *J. Phys. Chem. C,* 122, 540–548.

[27] Zecchina, A., Bordiga, S., Vitillo, J. G., Ricchiardi, G., Lamberti, C., Spoto, G., Bjørgen, M., Lillerud, K. P. (2005). Liquid hydrogen in protonic chabazite. *J. Am. Chem. Soc.,* 127, 6361–6366.

[28] Regli, L., Zecchina, A., Vitillo, J. G., Cocina, D., Spoto, G., Lamberti, C., Lillerud, K. P., Olsbye, U., Bordiga, S. (2005). Hydrogen storage in chabazite zeolite frameworks. *Phys. Chem. Chem. Phys.,* 7, 3197–3203.

[29] Erdoğan Alver, B. and Sakızcı, M. (2019). Hydrogen (H_2) adsorption on natural and cation-exchanged clinoptilolite, mordenite and chabazite. *Int. J. Hydrogen Energy,* 44, 6748–6755.

[30] Erdoğan, B. and Dikmen, G. (2020). Effect of the acid type on clinoptilolite-rich tuff for hydrogen storage. *Int. J. Hydrogen Energy,* 45, 2017–2021.

[31] Erdoğan Alver, B. and Esenli, F. (2017). Acid treated mordenites as adsorbents of C_2H_4 and H_2 gases. *Microporous Mesoporous Mater.* 244, 67–73.

[32] Wijiyanti, R., Gunawan, T., Nasri, N. S., Karim, Z. A., Ismail, A. F., Widiastuti, N. (2019). Hydrogen adsorption characteristics for zeolite-Y templated carbon. *Indonesian J. Chem.* 20, 29–42.

[33] Raj, M.C., Prasanth, K.P., Dangi, G.P., Bajaj, H.C. (2012). Hydrogen sorption in transition metal exchanged zeolite Y: Volumetric measurements and simulation study. *J. Porous Mater.* 19:657–666.

[34] Fujiwara, M., Fujio, Y., Sakurai, H., Senoh, H., Kiyobayashi, T (2014). Storage of molecular hydrogen into ZSM-5 zeolite in the ambient atmosphere by the sealing of the micropore outlet. *Chem. Eng. Process.: Process Intensification,* 79, 1–6.

[35] Tantawy, H.A. and Ismail, N. (2020). Microwave synthesis of nano/micronized zeolites from natural source: Evaluation of energy storage capacities. *Egypt. J. Chem.,* 63, 3669–3683.

[36] Bayrakdar Ates, E. (2024). Exploring the impact of NaOH pre-treatment for H_2 and CO_2 adsorption on clinoptilolite. *Int. J. Hydrogen Energy,* 50, 990–1003.

[37] Weitkamp J., Fritz M. and Ernst S. (1993). *Zeolites as media for hydrogen storage.* In: Proceedings from the Ninth International Zeolite Conference. Elsevier, 11–19.

[38] Park, K. S., Ni, Z., Côté, A. P., Choi, J. Y., Huang, R., Uribe-Romo, F. J., Chae, H. K., O'Keeffe, M., Yaghi, O. M. (2006). Exceptional chemical and thermal stability of zeolitic imidazolate frameworks. *Proc. Natl. Acad. Sci.,* 103, 10186–10191.

[39] Wu, H., Zhou, W. and Yildirim, T. (2007). Hydrogen storage in a prototypical zeolitic imidazolate framework-8. *J. Am. Chem. Soc.,* 129, 5314–5315.

[40] Cheng, P. and Hu, Y.H. (2014). H_2O-functionalized zeolitic Zn(2-methylimidazole)$_2$ framework (ZIF-8) for H_2 storage. *J. Phys. Chem. C.,* 118, 21866–21872.

[41] Wang, Y., Lan, Z., Huang, X., Liu, H., Guo, J. (2019). Study on catalytic effect and mechanism of MOF (MOF= ZIF-8, ZIF-67, MOF-74) on hydrogen storage properties of magnesium. *Int. J. Hydrogen Energy,* 44, 28863–28873.

[42] Villajos, J. A., Orcajo, G., Calleja, G., Botas, J. A., Martos, C. (2016). Beneficial cooperative effect between Pd nanoparticles and ZIF-8 material for hydrogen storage. *Int. J. Hydrogen Energy,* 41, 19439–19446.

[43] Bose, R., Ethiraj, J., Sridhar, P., Varghese, J. J., Kaisare, N. S., Selvam, P. (2020). Adsorption of hydrogen and carbon dioxide in zeolitic imidazolate framework structure with SOD topology: Experimental and modelling studies. *Adsorption,* 26, 1027–1038.

[44] Balderas-Xicohtencatl, R., Villajos, J. A., Casabán, J., Wong, D., Maiwald, M., Hirscher, M (2023). ZIF-8 pellets as a robust material for hydrogen cryo-adsorption tanks. *ACS Appl. Energy Mater.,* 6, 9145–9152.

[45] Muduli, R. C., Nishad, N. K., Dashbabu, D., Emadabathuni, A. K., Kale, P. (2024). Synergistic integration of nickel, porous silicon, and thermally reduced graphene oxide for solid-state hydrogen energy storage. *Energy Storage,* 6 (5), e70008.

[46] Muduli, R.C. and Kale, P. (2024). Sorption properties of nanostructured ball-milled porous silicon for solid-state hydrogen storage up to 80 bar. *Int. J. Hydrogen Energy,* 140, 920-930.

[47] Muduli, R.C. and Kale, P. (2023). Silicon nanostructures for solid-state hydrogen storage: A review. *Int. J. Hydrogen Energy,* 48, 1401–1439.

[48] Kale P., Gangal A.C., Edla R., Sharma P. (2012). Investigation of hydrogen storage behavior of silicon nanoparticles. *Int. J. Hydrogen Energy,* 37, 3741–3747.

[49] Muduli, R.C., Chen Z., Guo F., Jain A., Miyaoka H., Ichikawa T., Kale P. (2024). Enhancing the solid-state hydrogen storage properties of lithium hydride through thermodynamic tuning with porous silicon nanowires. *Energy Advances,* 3, 2212–2219.

[50] Muduli, R.C., Gupta, N., Sharma, P., Kale, P. (2024). Investigating reversible hydrogen storage and performance of porous Si by kinetic study and pressure composition isotherms at up to 20 bar. *Int. J. Hydrogen Energy,* 59, 447–456.

[51] Muduli, R.C. and Kale, P. (2023). Chemically modified surface of silicon nanostructures to enhance hydrogen uptake capabilities. *Int. J. Hydrogen Energy* 48, 37819–37833.

[52] Lee, J.B., Lee, S.C., Lee, S.M., Kim, H.J. (2007). Hydrogen adsorption characteristics of Li-dispersed silica nanotubes. *Chem. Phys. Lett.,* 436, 162–166.

[53] He, Z., Wang, S., Wang, X., Iqbal, Z. (2013). Hydrogen storage in hierarchical nanoporous silicon-carbon nanotube architectures. *Int. J. Energy. Res.,* 37, 754–760.

[54] Rouquerol, J., Rouquerol, F., Llewellyn, P., Maurin, G., Sing, K (2013). *Adsorption by powders and porous solids: Principles, methodology and applications.* Academic Press

[55] Chang, F., Zhou, J., Chen, P., Chen, Y., Honghua J., Sameh, M.I., Saad, Y.G., Xun, C., Zheng, T. (2013). Microporous and mesoporous materials for gas storage and separation: A review. *Asia-Pac. J. Chem. Eng.,* 8, 618–626.

[56] Moon,, J.H., Bae, J.H., Han, Y.J., Lee, C.H. (2010). Adsorbent/membrane hybrid (AMH) system for hydrogen separation: Synergy effect between zeolite 5A and silica membrane. *J. Memb. Sci.,* 356, 58–69.

[57] Ackley, M.W., Giese, R.F., and Yang, R.T. (1992). Clinoptilolite: Untapped potential for kinetics gas separations. *Zeolites,* 12, 780–788.

[58] Velarde, L., Nabavi, M. S., Escalera, E., Antti, M. L., Akhtar, F. (2023). Adsorption of heavy metals on natural zeolites: A review. *Chemosphere,* 328, 138508.

[59] Ma J., Su G., Zhang X., Huang W. (2016). Adsorption of heavy metal ions from aqueous solutions by bentonite nanocomposites. *Water Environ. Res.,* 88, 741–746.

[60] Elboughdiri, N. (2020). The use of natural zeolite to remove heavy metals Cu (II), Pb (II) and Cd (II), from industrial wastewater. *Cogent. Eng.,* 7, 1782623.

[61] Pepe, F., de Gennaro B., Aprea P., Caputo D. (2013). Natural zeolites for heavy metals removal from aqueous solutions: Modeling of the fixed bed Ba^{2+}/Na^{+} ion-exchange process using a mixed phillipsite/chabazite-rich tuff. *Chem. Eng. J.,* 219, 37–42.

[62] Zabochnicka-Świątek, M. and Malińska K. (2010). Removal of ammonia by clinoptilolite. *Global Nest. J.,* 12, 256–261.

[63] Saha, D. and Deng, S. (2010). Characteristics of ammonia adsorption on activated alumina. *J. Chem. Eng. Data,* 55, 5587–5593.

[64] Zuo, J. (2010). Adsorption properties of modified zeolite for ammonia removal. *4th Int. Conf. Bioinformatics Biomed. Eng.,* 1–4.

[65] Aziz, M., TriWijayanta, A. and Nandiyanto, A.B.D. (2020). Ammonia as effective hydrogen storage: A review on production, storage and utilization. *Energies,* 13, 3062.

[66] Jena, P. (2011). Materials for hydrogen storage: Past, present, and future. *J. Phys. Chem. Lett.,* 2, 206–211.

[67] Van Den Berg, A.W.C. and Areán, C.O. (2008). Materials for hydrogen storage: Current research trends and perspectives. *Chem. Commun.,* 668–681

[68] Rimza, T., Saha, S., Dhand, C., Dwivedi, N., Patel, S.S., Singh, S., Kumar, P. (2022). Carbon-based sorbents for hydrogen storage: Challenges and sustainability at operating conditions for renewable energy. *ChemSusChem,* 15(11), e202200281.

[69] Shaw, D.J. (1992). *Introduction to colloid and surface chemistry*, 2nd ed. Elsevier.

[70] Sing, K.S.W. (1985). Reporting physisorption data for gas/solid systems with special reference to the determination of surface area and porosity (Recommendations 1984). *Pure Appl. Chem.,* 57, 603–619.

[71] Zdravkov, B., Čermák, J., Šefara, M., Janků, J. (2007). Pore classification in the characterization of porous materials: A perspective. *Open Chem.,* 5, 385–395.

[72] Langmuir, I. (1918). The adsorption of gases on plane surfaces of glass, mica and platinum. *J. Am. Chem. Soc.,* 40, 1361–1403.

[73] Salahshoor, S., Fahes, M. and Teodoriu, C. (2018). A review on the effect of confinement on phase behavior in tight formations. *J. Nat. Gas. Sci. Eng.,* 51, 89–103.

[74] Rouquerol, J., Llewellyn, P. and Rouquerol, F. (2007). *Is the BET equation applicable to microporous adsorbents? In: Studies in surface science and catalysis*. Elsevier, pp 49–56.

[75] Bragg, W.H. and Bragg, W.L. (1913). *The reflection of X-rays by crystals*. *Proc. R. Soc. Lond. A,* 88, 428–438.

[76] Hammond, C. (2015). *The basics of crystallography and diffraction*. Oxford University Press.

[77] Harrington, G.F. and Santiso, J. (2021). Back-to-basics tutorial: X-ray diffraction of thin films. *J. Electroceram.,* 47, 141–163.

[78] Yildiz, A., Genc O. and Bektas, S. (1997). *Enstrümental Analiz Yöntemleri.* Hacettepe Üniversitesi Yayınları, Ankara.

[79] Oyedotun, T.D.T. (2018). X-ray fluorescence (XRF) in the investigation of the composition of earth materials: A review and an overview. *Geol. Ecol. Landscapes,* 2, 148–154.

[80] Gündüz, T. (2018). *Enstrümental Analiz.* Gazi Yayıncılık, Ankara.

[81] Herrero, Y.R., Camas, K.L. and Ullah, A. (2023). *Characterization of biobased materials. In: Advanced Applications of Biobased Materials.* Elsevier, pp. 111–143.

[82] Vernon-Parry, K.D. (2000). Scanning electron microscopy: an introduction. *III-Vs Rev.,* 13, 40–44.

[83] Goldstein, J. I., Newbury, D. E., Michael, J. R., Ritchie, N. W., Scott, J. H. J., Joy, D. C. (2017). *Scanning electron microscopy and X-ray microanalysis.* Springer.

[84] Webb, P.A. and Orr, C. (1997). *Analytical methods in fine particle technology.* Micromeritics Instrument Corporation.

[85] Thommes, M., Kaneko, K., Neimark, A. V., Olivier, J. P., Rodriguez-Reinoso, F., Rouquerol, J., Sing, K. S. (2015). Physisorption of gases, with special reference to the evaluation of surface area and pore size distribution (IUPAC Technical Report). *Pure. Appl. Chem.,* 87, 1051–1069.

[86] Gottardi, G. and Galli, E. (1985). *Natural Zeolites. Springer Berlin Heidelberg,* Berlin, Heidelberg.

[87] Xu R., Pang W., Yu J., Huo, Q., Chen, J. (2009). *Chemistry of zeolites and related porous materials: synthesis and structure.* John Wiley & Sons.

[88] Breck, D.W. (1984). *Zeolite Molecular Sieves: Structure, Chemistry, and Use.* John Wiley & Sons Inc., New York.

[89] Ulmanu, M. and Anger, I. (2012). Physical and chemical properties. In: Handbook of natural zeolites. *Bentham Science Publishers*, pp. 70–102.

[90] IZA Database of Zeolite Structures. Available at: https://www.iza-structure.org/databases/ (Date of Access: 04 Febuary 2025).

[91] Shi, J., Hu, J., Wu, Q., Chen, W., Dong, Z., Zheng, A., Ma, Y., Meng, X. ve Xiao, F.-S. (2023). A six-membered ring molecular sieve achieved by a reconstruction route. *J. Am. Chem. Soc.,* 145, 7712–7717.

[92] Gao, Z. R., Yu, H., Chen, F.-J., Mayoral, A., Niu, Z., Niu, Z., Li, X., Deng, H., Márquez-Álvarez, C., He, H., Xu, S., Zhou, Y., Xu, J., Xu, H., Fan, W., Balestra, S. R. G., Ma, C., Hao, J., Li, J., Wu, P., Yu, J., Camblor, M. A. (2024). Interchain-expanded extra-large-pore zeolites. *Nature,* 62, 99–103.

[93] Mumpton, F.A. (1960). Clinoptilolite redefined. *Am. Miner.,* 45, 351–369.

[94] Erdoğan, B. and Ergürhan, O. (2024). Natural and pretreated Gördes clinoptilolites for ammonia removal: effect of exchangeable cations (Na^+, K^+, Ca^{2+}, and Mg^{2+}). *Clay. Miner.,* 59, 39–49.

[95] Passaglia, E. and Sheppard, R.A. (2001). The crystal chemistry of zeolites. *Rev. Mineral. Geochem.,* 45, 69–116.

[96] Smyth, J.R., Spaid, A.T. and Bish, D.L. (1990). Crystal structures of a natural and a Cs-exchanged clinoptilolite. *Am Miner.,* 75, 522–528.

[97] Jayaraman, A., Yang, R.T., Chinn, D., Munson, C.L. (2005). Tailored clinoptilolites for nitrogen/methane separation. *Ind. Eng. Chem. Res.,* 44, 5184–5192.

[98] Kennedy, D.A. and Teze,l F.H. (2018). Cation exchange modification of clinoptilolite – Screening analysis for potential equilibrium and kinetic adsorption separations involving methane, nitrogen, and carbon dioxide. *Microporous Mesoporous Mater.,* 262, 235–250.

[99] Dimova, L., Petrov, O., Kadiyski, M., Lihareva, N., Stoyanova-Ivanova, A., Mikli, V. (2011). Preparation and Rietveld refinement of Ag-exchanged clinoptilolite. *Clay Miner.,* 46, 205–212.

[100] de las Pozas, C., Lopez-Cordero, R., Diaz-Aguila, C., Cora, M., Roque-Malherbe, R. (1995). Location and reducibility of Ni ions in HEU-type zeolites. *J. Solid State Chem.,* 114, 108–111.

[101] Armbruster, T., Simoncic, P., Döbelin, N., Malsy, A., Yang, P. (2003). Cu^{2+}-acetate and Cu^{2+}-ammine exchanged heulandite: a structural comparison. *Microporous Mesoporous Mater.,* 57, 121–131.

[102] Garcia-Basabe, Y., Ruiz-Salvador, A. R., Maurin, G., de Menorval, L. C., Rodriguez-Iznaga, I., Gomez, A. (2012). Location of extra-framework Co^{2+}, Ni^{2+}, Cu^{2+} and Zn^{2+} cations in natural and dealuminated clinoptilolite. *Microporous Mesoporous Mater.,* 155, 233–239.

[103] Ghahri, A., Golbabaei, F., Vafajoo, L., Mireskandari, S. M., Yaseri, M., Shahtaheri, S. J (2017). Removal of greenhouse gas (N_2O) by catalytic decomposition on natural clinoptilolite zeolites impregnated with cobalt. *Int. J. Environ. Res.,* 11, 327–337.

[104] Karousos, D. S., Sapalidis, A. A., Kouvelos, E. P., Romanos, G. E., Kanellopoulos, N. K. (2016). A study on natural clinoptilolite for CO_2/N_2 gas separation. *Sep. Sci. Technol.,* 51, 83–95.

[105] Zeszyt, T., Maèala, J., Pandová, I., Panda, A. (2009). Clinoptilolite as a mineral usable for cleaning of exhaust gases. *Gospodarka Surowcami Mineralnymi – Miner., Resour. Manag.,* 25, 23–32.

[106] Allen, S.J., Ivanova, E. and Koumanova, B. (2009). Adsorption of sulfur dioxide on chemically modified natural clinoptilolite. Acid modification. *Chem. Eng. J.,* 152, 389–395.

[107] Banerjee, R., Furukawa, H., Britt, D., Knobler, C., O'Keeffe, M., Yaghi, O. M. (2009). Control of pore size and functionality in isoreticular zeolitic imidazolate frameworks and their carbon dioxide selective capture properties. *J. Am. Chem. Soc.,* 131, 3875–3877.

[108] Morris, W., Doonan, C. J., Furukawa, H., Banerjee, R., Yaghi, O. M. (2008). Crystals as molecules: postsynthesis covalent functionalization of zeolitic imidazolate frameworks. *J. Am. Chem. Soc.,* 130, 12626–12627.

[109] Acuna-Yeomans E., Gutierrez-Sevillano J.J., Calero S., Dubbeldam D. (2023). Evaluation of ZIF-8 flexible force fields for structural and mechanical properties. *Microporous and Mesoporous Mater.,* 348, 112406.

[110] Zhang, C., Lively, R. P., Zhang, K., Johnson, J. R., Karvan, O., Koros, W. J. (2012). Unexpected molecular sieving properties of zeolitic imidazolate framework-8. *J. Phys. Chem. Lett.,* 3, 2130–2134.

[111] Cravillon, J., Münzer, S., Lohmeier, S.J., Feldhoff, A., Huber, K., Wiebcke, M. (2009). Rapid room-temperature synthesis and characterization of nanocrystals of a prototypical zeolitic imidazolate framework. *Chem. Mater.,* 21, 1410–1412.

[112] Butova, V.V., Budnyk, A.P., Bulanova, E. A., Lamberti, C., Soldatov, A.V. (2017). Hydrothermal synthesis of high surface area ZIF-8 with minimal use of TEA. *Solid State Sci.,* 69, 13–21.

[113] Seoane, B., Zamaro, J.M., Tellez, C., Coronas, J. (2012). Sonocrystallization of zeolitic imidazolate frameworks (ZIF-7, ZIF-8, ZIF-11 and ZIF-20). *CrystEngComm,* 14, 3103–3107.

[114] Cho, H.-Y., Kim, J., Kim, S.-N., Ahn, W.-S. (2013). High yield 1-L scale synthesis of ZIF-8 via a sonochemical route. *Microporous and Mesoporous Mater.,* 169, 180–184.

[115] Martinez, V., Stolar, T., Karadeniz, B., Brekalo, I., Užarević, K (2023). Advancing mechanochemical synthesis by combining milling with different energy sources. *Nat. Rev. Chem.,* 7, 51–65.

[116] Martinez, V., Karadeniz, B., Biliškov, N., Lončarić, I., Muratović, S., Žilić, D., Avdoshenko, S. M., Roslova, M., Popov, A. A., Užarević, K. (2020). Tunable fulleretic sodalite MOFs: highly efficient and controllable entrapment of C60 fullerene via mechanochemistry. *Chem. Mater.,* 32, 10628–10640.

[117] Yang, L. and Lu, H. (2012). Microwave-assisted ionothermal synthesis and characterization of zeolitic imidazolate framework-8. *Chin. J. Chem.,* 30, 1040–1044.

[118] Bao, Q., Lou, Y., Xing, T., Chen, J. (2013). Rapid synthesis of zeolitic imidazolate framework-8 (ZIF-8) in aqueous solution via microwave irradiation. *Inorg. Chem. Commun.,* 37, 170–173.

[119] Xing, T., Lou, Y., Bao, Q., Chen, J. (2014). Surfactant-assisted synthesis of ZIF-8 nanocrystals in aqueous solution via microwave irradiation. *CrystEngComm,* 16, 8994–9000.

[120] Mu, L., Liu, B., Liu, H., Yang, Y., Sun, C., Chen, G (2012). A novel method to improve the gas storage capacity of ZIF-8. *J. Mater. Chem.,* 22, 12246–12252.

[121] Liu, M., Yu, H., Liu, D., Zhang, G., Wang, F. (2024). Methane dense storage in ZIF-8@cu under low pressure via adsorption-absorption synergy. *J. Energy Storage*., 103, 114400.

[122] Hu, Y., Liu, Z., Xu, J., Huang, Y., Song, Y. (2013). Evidence of pressure enhanced CO_2 storage in ZIF-8 probed by FTIR spectroscopy. *J. Am. Chem. Soc.,* 135, 9287–9290.

[123] Byrne, C., Ristić, A., Mal, S., Opresnik, M., Zabukovec Logar, N. (2021). Evaluation of ZIF-8 and ZIF-90 as heat storage materials by using water, methanol and ethanol as working fluids. *Crystals (Basel),* 11, 1422.

[124] Paul, A., Banga I.K., Muthukumar S., Prasad S. (2022). Engineering the ZIF-8 pore for electrochemical sensor applications─ a mini review. *ACS Omega,* 7, 26993–27003.

[125] Dai, H., Yuan, X., Jiang, L., Wang, H., Zhang, J., Zhang, J., Xiong, T. (2021). Recent advances on ZIF-8 composites for adsorption and photocatalytic wastewater pollutant removal: fabrication, applications and perspective. *Coord. Chem. Rev.,* 441, 213985.

[126] Abdelhamid, H.N. (2021). Zeolitic imidazolate frameworks (ZIF-8) for biomedical applications: a review. *Curr. Med. Chem.,* 28, 7023–7075.

[127] Hoseinpour, V. and Shariatinia, Z. (2021). Applications of zeolitic imidazolate framework-8 (ZIF-8) in bone tissue engineering: a review. *Tissue Cell,* 72, 101588.

[128] Karagiaridi, O., Lalonde, M. B., Bury, W., Sarjeant, A. A., Farha, O. K., Hupp, J. T. (2012). Opening ZIF-8: a catalytically active zeolitic imidazolate framework of sodalite topology with unsubstituted linkers. *J. Chem. Soc.,* 134, 18790–18796.

[129] Sahoo, M.K. and Kale, P. (2019). Integration of silicon nanowires in solar cell structure for efficiency enhancement: a review. *J. Materiomics,* 5, 34–48.

[130] Sahoo, M.K. and Kale, P. (2019). Restructured porous silicon for solar photovoltaic: a review. *Microporous and Mesoporous Mater.,* 289, 109619.

[131] Korotcenkov, G. and Cho, B.K. (2010). Porous semiconductors: advanced material for gas sensor applications. *Crit. Rev. Solid State Mater. Sci.,* 35, 1–37.

[132] Kale, P.G. and Solanki, C.S. (2010). Synthesis of Si nanoparticles from freestanding porous silicon (PS) film using ultrasonication. In: *2010 35th IEEE Photovoltaic Specialists Conference*. IEEE, 3692–3697.

[133] Huang, Z., Geyer, N., Werner, P., De Boor, J., Gösele, U (2011). Metal-assisted chemical etching of silicon: a review. *Adv. Mater.,* 23, 285–308.

[134] Ghafarinazari, A., Mozafari, M. (2014). A systematic study on metal-assisted chemical etching of high aspect ratio silicon nanostructures. *J. Alloys. Compd.,* 616, 442–448.

[135] Weisse, J. M., Lee, C. H., Kim, D. R., Cai, L., Rao, P. M., Zheng, X. (2013). Electroassisted transfer of vertical silicon wire arrays using a sacrificial porous silicon layer. *Nano. Lett.,* 13, 4362–4368.

[136] Singh N., Sahoo M.K. and Kale P.G. (2018). Effect of MACE parameters on length of porous silicon nanowires (PSiNWs). *J. Cryst. Growth,* 496–497, 10–14.

[137] Toor, F., Miller, J. B., Davidson, L. M., Nichols, L., Duan, W., Jura, M. P., Yim, J., Forziati, J., Black, M. R. (2016). Nanostructured silicon via metal assisted catalyzed etch (MACE): chemistry fundamentals and pattern engineering. *Nanotechnol.* 7, 412003.

[138] Peng, K.Q., Huang, Z.P. and Zhu, J. (2004). Fabrication of large-area silicon nanowire p–n junction diode arrays. *Adv. Mater.* 16, 73–76.

[139] Smith, Z.R., Smith, R.L. and Collins, S.D. (2013). Mechanism of nanowire formation in metal assisted chemical etching. *Electrochim Acta* 92, 139–147.

[140] Dimova-Malinovska, D., Sendova-Vassileva, M., Tzenov, N., Kamenova, M. (1997). Preparation of thin porous silicon layers by stain etching. *Thin Solid Films* 297, 9–12.

[141] Li, X. and Bohn, P. W. (2000). Metal-assisted chemical etching in HF/H_2O_2 produces porous silicon. *Appl. Phys. Lett.*, 77(18), 2572–2574.

[142] Qu, Y., Zhou, H. and Duan, X. (2011). Porous silicon nanowires. *Nanoscale*, 3(9), 4060.

[143] Sailor, M. J. (2012). Porous silicon in practice: preparation, characterization and applications. John Wiley & Sons.

[144] Monaico, E., Tiginyanu, I. and Ursaki, V. (2020). Porous semiconductor compounds. *Semicond. Sci. Technol.*, 35(10), 103001.

[145] Lévy-Clément, C. (2014). Porous silicon formation by metal nanoparticle-assisted etching. In L. Canham (Ed.), Handbook of porous silicon (pp. 49–66). Springer International Publishing.

[146] Chiappini, C. (2014). Mace silicon nanostructures. In L. Canham (Ed.), Handbook of porous silicon (pp. 171–186). Springer International Publishing.

[147] Tang, C. H., Li, W. J., Hung, C. H., Hsiao, P. H., Chen, C. Y. (2017). Highly porous silicon nanowires made with solvent-mediated wet chemical etching and their thermoelectric applications. *ChemistrySelect*, 2(34), 10865–10870.

[148] Lo, Faro, M. J., Leonardi, A. A., D'Andrea, C., Morganti, D., Musumeci, P., Vasi, C., Priolo, F., Fazio, B., Irrera, A. (2020). Low cost synthesis of silicon nanowires for photonic applications. *J. Mater. Sci. Mater. Electronics* 31(1), 34–40.

[149] Hui, S., Zhang, J., Chen, X., Xu, H., Ma, D., Liu, Y., Tao, B. (2011). Study of an amperometric glucose sensor based on Pd–Ni/SiNW electrode. *Sens. Actuators B: Chem.*, 155 (2), 592–597.

[150] Zhang, F., Wan, L., Chen, J., Li, X., Yan, X. (2018). Crossed carbon skeleton enhances the electrochemical performance of porous silicon nanowires for lithium ion battery anode. *Electrochimica Acta*, 280, 86–93.

[151] Qin, Y., Liu, D., Zhang, T., Cui, Z. (2017). Ultrasensitive silicon nanowire sensor developed by a special Ag modification process for rapid NH_3 detection. *ACS Appl. Mater. Interfaces*, 9 (36), 28766–28773.

[152] Moore, D. M. and Reynolds, R. C. Jr. (1997). *X-ray diffraction and the identification and analysis of clay minerals.* Oxford University Press.

[153] Esenli, F. and Sirkecioğlu, A. (2005). The relationship between zeolite (heulandite-clinoptilolite) content and the ammonium-exchange capacity of pyroclastic rocks in Gördes, Turkey. *Clay Miner.* 40 (4), 557–564.

[154] Rodríguez-Iznaga, I., Shelyapina, M.G. and Petranovskii, V. (2022). Ion exchange in natural clinoptilolite: aspects related to its structure and applications. *Minerals*, 12 (12), 1628.

[155] Galli, E., Gottardi, G., Mayer, H., Preisinger, A., Passaglia, E. (1983). The structure of potassium-exchanged heulandite at 293, 373 and 593 K. *Acta Cryst. B*, 39(1), 189–197.

[156] Kitsopoulos, K. P. (2001) The relationship between the thermal behavior of clinoptilolite and its chemical composition. *Clays Clay Miner.*, 49(3), 236-243.

[157] Garcia-Basabe, Y., Rodriguez-Iznaga, I., de Menorval, L.-C., Llewellyn, P., Maurin, G., Lewis, D. W., Binions, R., Autie, M., Ruiz-Salvador, A. R. (2010). Step-wise dealumination of natural clinoptilolite: structural and physicochemical characterization. *Microporous Mesoporous Mater.*, 135 (1–3), 187–196.

[158] Kudoh, Y. and Takéuchi, Y. (1983). Thermal stability of clinoptilolite: the crystal structure at 350°C. *Mineral. J.*, 11 (4), 392–406.

[159] Bish, D. L. (1984). Effects of exchangeable cation composition on the thermal expansion/contraction of clinoptilolite. *Clays Clay Miner.*, 32 (6), 444–452.

[160] Tansel, B., Sager, J., Rector, T., Garland, J., Strayer, R. F., Levine, L., Roberts, M., Hummerick, M., Bauer, J. (2006). Significance of hydrated radius and hydration shells on ionic permeability during nanofiltration in dead end and cross flow modes. *Sep. Pur. Technol.*, 51 (1), 40–47.

[161] Elaiopoulos, K., Perraki, T. and Grigoropoulou, E. (2010). Monitoring the effect of hydrothermal treatments on the structure of a natural zeolite through a combined XRD, FTIR, XRF, SEM and N_2-porosimetry analysis. *Microporous Mesoporous Mater.*, 134 (1–3), 180–187.

[162] Tomazović, B., Ćeranić, T. and Sijarić, G. (1996). The properties of the NH4-clinoptilolite. Part 2. *Zeolites*, 16 (4), 309–312.

[163] Nakamoto, K. (2008). Infrared and Raman spectra of inorganic and coordination compounds part A: theory and applications in inorganic chemistry. John Wiley & Sons.

[164] Mozgawa, W. (2001). The relation between structure and vibrational spectra of natural zeolites. *J. Mol. Struct.*, 596 (1–3), 129–137.

[165] Handke, M. and Mozgawa, W. (1993). Vibrational spectroscopy of the amorphous silicates. *Vibrational Spectroscopy*, 5 (1), 75–84.

[166] Akdeniz, Y. and Ülkü, S. (2008). Thermal stability of Ag-exchanged clinoptilolite rich mineral. *J. Therm. Anal. Calorim.*, 94 (3), 703–710.

[167] Rodriguez-Fuentes, G., Ruiz-Salvador, A. R., Mir, M., Picazo, O., Quintana, G., Delgado, M. (1998). Thermal and cation influence on IR vibrations of modified natural clinoptilolite. *Microporous Mesoporous Mater.*, 20 (3), 269–281.

[168] Mozgawa, W. and Bajda, T. (2006). Application of vibrational spectra in the studies of cation sorption on zeolites. *J. Mol. Struc.*, 792–793, 170–175.

[169] Brundu, A. and Cerri, G. (2015). Thermal transformation of Cs-clinoptilolite to CsAlSi5O12. *Microporous Mesoporous Mater.*, 208, 44–49.

[170] Mansouri, N., Rikhtegar, N., Panahi, H. A., Atabi, F., Shahraki, B. K. (2013). Porosity, characterization and structural properties of natural zeolite-clinoptilolite as a sorbent. *Enviro. Protection Eng.*, 39(2), 139–152.

[171] Faghihian, H., Talebi, M. and Pirouzi, M. (2008). Adsorption of nitrogen from natural gas by clinoptilolite. *J.Iranian Che. Soc.*, 5(3), 394–399.

[172] Ackley, M. W. and Yang, R. T. (1991). Diffusion in ion-exchanged clinoptilolites. *AIChE J.*, 37 (11), 1645–1656.

[173] Kennedy, D. A., Khanafer, M. and Tezel, F. H. (2019). The effect of Ag^+ cations on the micropore properties of clinoptilolite and related adsorption separation of CH_4 and N_2 gases. *Microporous Mesoporous Mater.*, 283, 137–144.

[174] Elaiopoulos, K., Perraki, T., Grigoropoulou, E. (2008). Mineralogical study and porosimetry measurements of zeolites from Scaloma area, Thrace, Greece. *Microporous Mesoporous Mater.*, 112 (1–3), 441–449.

[175] Chang, N., Chen, Y. R., Xie, F., Liu, Y. P. and Wang, H. T. (2021). Facile construction of Z-scheme AgCl/Ag-doped-ZIF-8 heterojunction with narrow band gaps for efficient visible-light photocatalysis. *Colloids Surf. A: Physicochem. Eng. Asp.*, 616, 126351.

[176] Zhang, C., Lively, R. P., Zhang, K., Johnson, J. R., Karvan, O., Koros, W. J. (2012). Unexpected molecular sieving properties of zeolitic imidazolate framework-8. *J. Phys. Chem. Lett.*, 3 (15), 2130–2134.

[177] Zhang, Y., Jia, Y. and Hou, L. (2018). Synthesis of zeolitic imidazolate framework-8 on polyester fiber for PM2.5 removal. *RSC Advances*, 8(55), 31471–31477.

[178] Tuncel, D. and Ökte, A. N. (2021). Improved adsorption capacity and photoactivity of ZnO-ZIF-8 nanocomposites. *Catal. Today*, 361, 191–197.

[179] Ahmad, M., Patel, R., Lee, D. T., Corkery, P., Kraetz, A., Prerna, Tenney, S. A., Nykypanchuk, D., Tong, X., Siepmann, J. I., Tsapatsis, M., Boscoboinik, J. A. (2024). ZIF-8 vibrational spectra: peak assignments and defect signals. *ACS Appl. Mater. Interfaces*, 16(25), 27887–27897.

[180] Wang, H.-T., Liu, Y.-P., Zhang, H., Chang, N., Shao, W., Shi, M.-S., Ao, D., Lu, M. (2019). Design and synthesis of porous C–ZnO/TiO2@ZIF-8 multi-component nano-system via pyrolysis strategy with high adsorption capacity and visible light photocatalytic activity. *Microporous Mesoporous Mater.*, 288, 109548.

[181] Li, N., Zhou, L., Jin, X., Owens, G., Chen, Z. (2019). Simultaneous removal of tetracycline and oxytetracycline antibiotics from wastewater using a ZIF-8 metal organic-framework. *J. Hazard. Mater.*, 366, 563–572.

[182] Boada, R., Chaboy, J., Hayama, S., Keenan, L. L., Freeman, A. A., Amboage, M., Díaz-Moreno, S. (2022). Unraveling the molecular details of the "gate opening" phenomenon in ZIF-8 with X-ray absorption spectroscopy. *J. Phys. Chemy. C*, 126, 5935–5943.

[183] Chokbunpiam, T., Fritzsche, S., Chmelik, C., Caro, J., Janke, W., Hannongbua, S. (2016). Gate opening effect for carbon dioxide in ZIF-8 by molecular dynamics–confirmed, but at high CO_2 pressure. *Chem. Phys. Lett.*, 648, 178–181.

[184] Li, S., Ma, W., Zhou, Y., Chen, X., Xiao, Y., Ma, M., Zhu, W., Wei, F. (2014). Fabrication of porous silicon nanowires by MACE method in $HF/H_2O_2/AgNO_3$ system at room temperature. *Nanoscale Res. Lett.*, 9, 196.

[185] Paul, P. P., McShane, E. J., Colclasure, A. M., Balsara, N., Brown, D. E., Cao, C., Chen, B.-R., Chinnam, P. R., Cui, Y., Dufek, E. J., Finegan, D. P., Gillard, S., Huang, W., Konz, Z. M., Kostecki, R., Liu, F., Lubner, S., Prasher, R., Preefer, M. B., Qian, J., Rodrigues, M.-T. F., Schnabel, M., Son, S.-B., Srinivasan, V., Steinrück, H.-G., Tanim, T. R., Toney, M. F., Tong, W., Usseglio-Viretta, F., Wan,

J., Yusuf, M., McCloskey, B. D., Weker, J. N. (2021). A review of existing and emerging methods for lithium detection and characterization in Li-ion and Li-metal batteries. *Adv. Energy. Mater.*, 11.

[186] Akyalcin, S., Akyalcin, L. and Ertugrul, E. (2024). Modification of natural clinoptilolite zeolite to enhance its hydrogen adsorption capacity. *Res. Chem. Intermeds.*, 50, 1455–1473.

[187] Bordiga, S., Turnes Palomino, G., Pazè, C., Zecchina, A. (2000). Vibrational spectroscopy of H_2, N_2, CO and NO adsorbed on H, Li, Na, K-exchanged ferrierite. *Microporous Mesoporous Mater.*, 34, 67–80.

[188] Drenchev, N. and Hadjiivanov, K. (2014). Interaction of H_2 (D_2) with OH (OD) groups in a ZSM-5 zeolite: FTIR study of the isotopic effects. *J. Phys. Chem. C*, 118, 25118–25123.

[189] Kubo, M., Kamimura, Y., Itabashi, K., Okubo, T. (2014). Cryogenic hydrogen adsorption onto H-, Li-, Na-exchanged zeolites with various Si/Al ratios. *Adsorption Sci. Tech.*, 32, 413–423.

[190] Zavorotynska, O., Vitillo, J. G., Spoto, G., Zecchina, A. (2011). Role of extraframework metal sites for hydrogen adsorption into the pores of a zeolite: FT-IR study. *Int. J. Hydrogen. Energy*, 36, 7944–7950.

[191] Kozyra, P. and Piskorz, W. (2016). A comparative computational study on hydrogen adsorption on the Ag^{+}, Cu^{+}, Mg^{2+}, Cd^{2+}, and Zn^{2+} cationic sites in zeolites. *Phys. Chem. Chem. Phys.*, 18, 12592–12603.

[192] Shannon, R. D. (1976). Revised effective ionic radii and systematic studies of interatomic distances in halides and chalcogenides. *Acta Crystallogr. Section A*, 32, 751–767.

[193] Fellah, M. F. (2014). Hydrogen adsorption on M-ZSM-12 zeolite clusters (M = K, Na and Li): a density functional theory study. *J. Porous Mater.*, 21, 883–888.

[194] Garrone, E., Bonelli, B. and Otero Areán, C. (2008). Enthalpy–entropy correlation for hydrogen adsorption on zeolites. *Chem. Phy.s Lett.*, 456, 68–70.

[195] Kang, L., Deng, W., Han, K., Zhang, T., Liu, Z. (2008). A DFT study of adsorption hydrogen on the Li-FAU zeolite. *Int. J. Hydrogen Energy*, 33, 105–110.

[196] Nachtigall, P., Garrone, E., Palomino, G. T., Delgado, M. R., Nachtigallova, D., & Areán, C. O. (2006). FTIR spectroscopic and computational studies on hydrogen adsorption on the zeolite Li–FER. *Phys. Chem. Chem. Phys.*, 8, 2286–2292.

[197] Ozturk, Z. (2018). Hydrogen storage on lithium modified silica based CHA-bazite type zeolite, a computational study. *Int. J. Hydrogen Energy*, 43, 22365–22376.

[198] Li, Y. and Yang, R. T. (2006). Hydrogen storage in low silica type X zeolites. *J. Phys. Chem. B*, 110, 17175–17181.

[199] Wang, L. and Yang, R. T. (2010). Hydrogen storage properties of low-silica type X zeolites. *Ind. Eng. Chem. Res.*, 49, 3634–3641.

[200] Kubo, M., Kamimura, Y., Itabashi, K., Okubo, T. (2014). Cryogenic hydrogen adsorption onto H-, Li-, Na-exchanged zeolites with various Si/Al ratios. *Adsorption Sci. Technol.*, 32, 413–423.

[201] Li, J., Wu, E., Song, J., Xiao, F., Geng, C. (2009). Cryoadsorption of hydrogen on divalent cation-exchanged X-zeolites. *Int. J. Hydrogen Energy*, 34, 5458–5465.

[202] Prasanth, K. P., Pillai, R. S., Bajaj, H. C., Jasra, R. V., Chung, H. D., Kim, T. H., Song, S. D. (2008). Adsorption of hydrogen in nickel and rhodium exchanged zeolite X. *Int. J. Hydrogen Energy*, 33, 735–745.

[203] Raj, M.C., Prasanth, K.P., Dangi, G.P., Bajaj, H.C. (2012). Hydrogen sorption in transition metal exchanged zeolite Y: volumetric measurements and simulation study. *J.Porous Mater.*, 19, 657–666.

[204] Kurniawan, R.Y., Romadiansyah, T.Q., Tsamarah, A.D., Widiastuti, N. (2018). Synthesis of zeolite-X from bottom ash for H_2 adsorption. In: *IOP Conference Series: Materials Science and Engineering*. IOP Publishing, p. 012083.

[205] Park, K.S., Ni, Z., Côté, A.P., Choi, J.Y., Huang, R., Uribe-Romo, F.J., Chae, H. K., O'Keeffe, M., Yaghi, O.M. (2006). Exceptional chemical and thermal stability of zeolitic imidazolate frameworks. *Proc. Natl. Acad. Sci.*, 103, 10186–10191.

[206] Zhou, W., Wu, H., Hartman, M.R., Yildirim, T. (2007). Hydrogen and methane adsorption in metal−organic frameworks: a high-pressure volumetric study. *J. Phys. Chem. C*, 111, 16131–16137.

[207] Wang, Y., Lan, Z., Huang, X., Liu, H., Guo, J. (2019). Study on catalytic effect and mechanism of MOF (MOF = ZIF-8, ZIF-67, MOF-74) on hydrogen storage properties of magnesium. *Int. J. Hydrogen Energy.*, 44, 28863–28873.

[208] Villajos, J. A., Orcajo, G., Calleja, G., Botas, J. A., Martos, C. (2016). Beneficial cooperative effect between Pd nanoparticles and ZIF-8 material for hydrogen storage. *Int. J. Hydrogen Energy.*, 41, 19439–19446.

[209] Bose, R., Ethiraj, J., Sridhar, P., Varghese, J.J., Kaisare, N.S., Selvam, P. (2020). Adsorption of hydrogen and carbon dioxide in zeolitic imidazolate framework structure with SOD topology: experimental and modelling studies. *Adsorption*, 26, 1027–1038.

[210] Balderas-Xicohtencatl, R., Villajos, J.A., Casabán, J., Wong, D., Maiwald, M., Hirscher, M. (2023). ZIF-8 pellets as a robust material for hydrogen cryo-adsorption tanks. *ACS Appl. Energy Mater.*, 6, 9145–9152.

[211] Terashi, M., Kuge, J. K., Shinohara, M., Shoji, D., Niwano, M. (1998). Hydrogen adsorption and desorption processes on Si(100). *Appl. Surf. Sci.*, 130, 260–265.

[212] Merazga, S., Cheriet, A., M'hammedi, K., Mefoued, A., Gabouze, N. (2019). Investigation of porous silicon thin films for electrochemical hydrogen storage. *Int. J. Hydrogen Energy*, 44, 9994–10002.

[213] Zikri, A., Trisnaliani, L., Aswan, A., and Firdausia, A. (2019). Hydrogen storage from the result of reactor ACE (Aluminum Corrosion and Electrolysis) production by pysisorption method. In: *J. Phys.: Conference Series*. Institute of Physics Publishing.

[214] Altiparmak, I., Karakaya, B., Uner, D., İpek, B. (2019). H_2 adsorption on Cu(I)-ZSM-5: exploration of Cu(I)-exchange in solution. *Int. J. Hydrogen Energy*, 44, 18866–18874.

[215] Erdogan, F. O. (2019). Freundlich, Langmuir, Temkin and Harkins-Jura isotherms studies of H_2 adsorption on porous adsorbents. *Chem. Chem. Technol.*, 13, 129–135.

[216] Moreira, M. A., Dias, R. O. M., Lee, U. H., Chang, J. S., Ribeiro, A. M., Ferreira, A. F. P., Rodrigues, A. E. (2019). Adsorption equilibrium of carbon dioxide, methane, nitrogen, carbon monoxide, and hydrogen on UiO-66(Zr)_$(COOH)_2$. *J. Chem. Eng. Data*, 64, 4724–4732.

[217] Larasati, Z. S. and Widiastuti, N. (2018). Adsorption-desorption of CO_2 and H_2 gases on zeolite-X supported on glass fiber. In: *AIP Conference Proceedings*. AIP Publishing.

[218] Dewi, S.T.J. and Widiastuti, N. (2018). Modification of zeolite-Y templated carbon at various nitrogen loading for hydrogen adsorption. In: *AIP Conference Proceedings*. American Institute of Physics Inc.

[219] Singh, S.B. and De, M. (2018). Alumina based doped templated carbons: a comparative study with zeolite and silica gel templates. *Microporous Mesoporous Mater.*, 257, 241–252.

[220] Beatrice, C.A.G., Oliveira, A.D., Passador, F.R., Pessan, L.A. (2017). Polymer nanocomposites for hydrogen storage. In: *AIP Conference Proceedings*. American Institute of Physics Inc.

[221] Blankenship T.S., Balahmar N. and Mokaya R. (2017). Oxygen-rich microporous carbons with exceptional hydrogen storage capacity. *Nat. Commun.,* 8, 1.

[222] Blankenship T.S. and Mokaya R. (2017). Cigarette butt-derived carbons have ultra-high surface area and unprecedented hydrogen storage capacity. *Energy Environ. Sci.,* 10, 2552–2562.

[223] Roy P. and Das N. (2017). Ultrasonic assisted synthesis of bikitaite zeolite: A potential material for hydrogen storage application. *Ultrason. Sonochem.,* 36, 466–473.

[224] Dündar-Tekkaya E., Yürüm Y. (2016). Mesoporous MCM-41 material for hydrogen storage: A short review. *Int. J. Hydrogen Energy,* 41, 9789–9795.

[225] Musyoka, N.M., Ren, J., Annamalai, P., Langmi, H.W., North, B.C., Mathe, M., Bessarabov, D. (2016) Synthesis of a hybrid MIL-101(Cr)/ZTC composite for hydrogen storage applications. *Res. Chem. Intermed.,* 42, 5299–5307.

[226] Sevilla, M., Sangchoom, W., Balahmar, N., Fuertes, A. B., Mokaya, R. (2016). Highly porous renewable carbons for enhanced storage of energy-related gases (H_2 and CO_2) at high pressures. *ACS Sustain. Chem. Eng.,* 4, 4710–4716.

[227] Adeniran B. and Mokaya R. (2015). Compactivation: A mechanochemical approach to carbons with superior porosity and exceptional performance for hydrogen and CO_2 storage. *Nano Energy,* 16, 173–185.

[228] Dündar-Tekkaya E. and Yürüm Y. (2015). Effect of loading bimetallic mixture of Ni and Pd on hydrogen storage capacity of MCM-41. *Int. J. Hydrogen Energy,* 40, 7636–7643.

[229] Musyoka, N.M., Ren, J., Langmi, H.W., North, B.C., Mathe, M. (2015). A comparison of hydrogen storage capacity of commercial and fly ash-derived zeolite X together with their respective templated carbon derivatives. *Int. J. Hydrogen Energy,* 40, 12705–12712.

[230] Morel, M., Mosquera, E., Diaz-Droguett, D.E., Carvajal, N., Roble, M., Rojas, V., Espinoza-González, R. (2015). Mineral magnetite as precursor in the synthesis of multi-walled carbon nanotubes and their capabilities of hydrogen adsorption. *Int. J. Hydrogen Energy,* 40, 15540–15548.

[231] Geng, Z., Zhang, C., Wang, D., Zhou, X., Cai, M. (2015). Pore size effects of nanoporous carbons with ultra-high surface area on high-pressure hydrogen storage. *J. Energy Chem.,* 24, 1–8.

[232] Cai, J., Li, L., Lv, X., Yang, C., Zhao, X. (2014). Large surface area ordered porous carbons via nanocasting zeolite 10x and high performance for hydrogen storage application. *ACS Appl. Mater. Interfaces,* 6, 167–175.

[233] Rubio, C., Murillo, B., Casado-Coterillo, C., Mayoral, Á., Téllez, C., Coronas, J., Berenguer-Murcia, Á., Cazorla-Amorós, D. (2014). Development of exfoliated layered stannosilicate for hydrogen adsorption. *Int. J. Hydrogen Energy,* 39, 13180–13188.

[234] Xia K., Hu J. and Jiang J. (2014). Enhanced room-temperature hydrogen storage in super-activated carbons: The role of porosity development by activation. *Appl. Surf. Sci.,* 315, 261–267.

[235] Cai J., Yang M., Xing Y., Zhao X. (2014). Large surface area sucrose-based carbons via template-assisted routes: Preparation, microstructure, and hydrogen adsorption properties. *Colloids Surf. A Physicochem. Eng. Asp.,* 444, 240–245.

[236] Liao X., Zhang T., Xiao Q., Yang, H., Zhao, G., Leng, X. (2013). Different effects of temperature on supramolecular protein and non-protein materials in hydrogen storage. *Int. J. Hydrogen Energy* 38, 991–998.

[237] Masika, E. and Mokaya, R. (2013). Preparation of ultrahigh surface area porous carbons templated using zeolite 13X for enhanced hydrogen storage. *Prog. Nat. Sci. Mater. Int.,* 23, 308–316.

[238] Öztürk, Z., Köse, D. A., Öztürk, B., Asan, A. (2013). Bazi metal organik kafes yapili bileşiklerin hidrojen depolama performanslarinin. *Gazi Üniversitesi Mühendislik Mimarlık Fakültesi Dergisi,* 28, 333–337

[239] Masika, E., Bourne, R. A., Chamberlain, T. W., Mokaya, R. (2013). Supercritical CO_2 mediated incorporation of Pd onto templated carbons: A route to optimizing the Pd particle size and hydrogen uptake density. *ACS Appl Mater. Interfaces,* 5, 5639–5647.

[240] Abid, H.R., Tian, H., Ang, H.M., Tade, M.O., Buckley, C.E., Wang, S. (2012). Nanosize Zr-metal organic framework (UiO-66) for hydrogen and carbon dioxide storage. *Chem. Eng. J.,* 187, 415–420.

[241] Stadie, N.P., Vajo, J.J., Cumberland, R.W., Wilson, A.A., Ahn, C.C., Fultz, B. (2012). Zeolite-templated car.bon materials for high-pressure hydrogen storage. *Langmuir,* 28, 10057–10063

[242] Yang S.J., Jung H., Kim T., Park C.R. (2012). Recent advances in hydrogen storage technologies based on nanoporous carbon materials. *Prog. Nat. Sci. Mater. Int.,* 22, 631–638.

[243] Yang, S.J., Im, J.H., Nishihara, H., Jung, H., Lee, K., Kyotani, T., Park, C.R. (2012). General relationship between hydrogen adsorption capacities at 77 and 298 K and pore characteristics of the porous adsorbents. *J. Phys. Chem. C,* 116, 10529–10540.

[244] Xia, Y., Zhu, Y. and Tang, Y. (2012). Preparation of sulfur-doped microporous carbons for the storage of hydrogen and carbon dioxide. *Carbon,* 50, 5543–5553.

[245] Masika, E. and Mokaya, R. (2012). Hydrogen storage in high surface area carbons with identical surface areas but different pore sizes: Direct demonstration of the effects of pore size. *J. Phys. Chem. C,* 116, 25734–25740.

[246] Anbia, M. and Mandegarzad, S. (2012). Enhanced hydrogen sorption on modified MIL-101 with Pt/CMK-3 by hydrogen spillover effect. *J. Alloys. Compd*., 532, 61–67.

[247] Prasanth, K.P., Rallapalli, P., Raj, M.C., Bajaj, H.C., Jasra, R.V. (2011). Enhanced hydrogen sorption in single walled carbon nanotube incorporated MIL-101 composite metal-organic framework. *Int. J. Hydrogen Energy.,* 36, 7594–7601.

[248] Alam, N. and Mokaya, R. (2011). The effect of Al content of zeolite template on the properties and hydrogen storage capacity of zeolite templated carbons. *Microporous Mesoporous Mater.,* 144, 140–147.

[249] Tedds, S., Walton, A., Broom, D.P., Book, D. (2011). Characterisation of porous hydrogen storage materials: Carbons, zeolites, MOFs and PIMs. *Faraday Discuss.,* 151, 75–94.

[250] Yang, Y., Brown, C.M., Zhao, C., Chaffee, A.L., Nick, B., Zhao, D., Webley, P.A., Schalch, J., Simmons, J.M., Liu, Y., Her, J.-H., Buckley, C.E., Sheppard, D.A. (2011). Micro-channel development and hydrogen adsorption properties in templated microporous carbons containing platinum nanoparticles. *Carbon,* 49, 1305–1317.

[251] Alam, N. and Mokaya, R. (2011). Characterisation and hydrogen storage of Pt-doped carbons templated by Pt-exchanged zeolite y. *Microporous Mesoporous Mater.,* 142, 716–724.

[252] Armandi, M., Bonelli, B., Cho, K., Ryoo, R., Garrone, E. (2011). Study of hydrogen physisorption on nanoporous carbon materials of different origin. *Int.. J Hydrogen Energy,* 36, 7937–7943.

[253] Alam N. and Mokaya R. (2010). Evolution of optimal porosity for improved hydrogen storage in templated zeolite-like carbons. *Energy Environ. Sci.,* 3, 1773–1781.

[254] Calleja G., Botas J. A., Sánchez-Sánchez M., Orcajo M. G. (2010). Hydrogen adsorption over zeolite-like MOF materials modified by ion exchange. *Int. J. Hydrogen Energy,* 35, 9916–9923.

[255] Prasanth, K. P., Raj, M. C., Bajaj, H. C., Kim, T. H., Jasra, R. V. (2010). Hydrogen sorption in transition metal modified mesoporous materials. *Int. J. Hydrogen Energy* 35, 2351–2360.

[256] Sevilla, M., Alam, N. and Mokaya, R. (2010). Enhancement of hydrogen storage capacity of zeolite-templated carbons by chemical activation. *J. Phys. Chem. C,* 114, 11314–11319.

[257] Zlotea, C., Campesi, R., Cuevas, F., Leroy, E., Dibandjo, P., Volkringer, C., Loiseau, T., Férey, G., Latroche, M. (2010). Pd nanoparticles embedded into a metal-organic framework: Synthesis, structural characteristics, and hydrogen sorption properties. *J. Am. Chem. Soc.,* 132, 2991–2997.

[258] Sevilla, M., Foulston, R. and Mokaya, R. (2010). Superactivated carbide-derived carbons with high hydrogen storage capacity. *Energy. Environ. Sci.,* 3, 223–227.

[259] Prasanth, K.P., Bajaj, H.C., Chung, H.D., Choo, K.Y., Kim, T.H., Jasra, R.V. (2009). Hydrogen sorption in transition metal modified ETS-10. *Int. J. Hydrogen Energy,* 34, 888–896.

[260] Nishihara, H., Hou, P.-X., Li, L.-X., Ito, M., Uchiyama, M., Kaburagi, T., Ikura, A., Katamura, J., Kawarada, T., Mizuuchi, K., Kyotani, T. (2009). High-pressure hydrogen storage in zeolite-templated carbon. *J. Phys. Chem. C,* 113, 3189–3196.

[261] Prasanth, K.P., Bajaj, H. C., Chung, H.D., Choo, K.Y., Kim, T.H., Jasra, R. V. (2009). Hydrogen sorption in transition metal modified NaETS-4. *J. Alloys. Compd.*, 480, 580–586.

[262] Nouar, F., Eckert, J., Eubank, J. F., Forster, P., Eddaoudi, M. (2009) Zeolite-like metal-organic frameworks (ZMOFs) as hydrogen storage platform: lithium and magnesium ion-exchange and h-(rho-ZMOF) interaction studies. *J. Am. Chem. Soc.*, 131, 2864–2870.

[263] Luzan, S.M., Jung, H., Chun, H., Talyzin, A.V. (2009). Hydrogen storage in co-and zn-based metal-organic frameworks at ambient temperature. *Int. J. Hydrogen Energy*, 34, 9754–9759.

[264] Yang, Y.X., Bourgeois, L., Zhao, C., Zhao, D., Chaffee, A., Webley, P. A. (2009) Ordered micro-porous carbon molecular sieves containing well-dispersed platinum nanoparticles for hydrogen storage. *Microporous Mesoporous Mater.*, 119, 39–46.

[265] Msayib, K.J., Book, D., Budd, P.M., Chaukura, N., Harris K.D.M., Helliwell M., Tedds S., Walton A., Warren J. E., Xu M., McKeown N. B. (2009) Nitrogen and hydrogen adsorption by an organic microporous crystal. *Angew. Chem. Int. Ed.*, 48, 3273–3277.

[266] Xia, Y., Walker, G.S., Grant, D.M., Mokaya, R. (2009). Hydrogen storage in high surface area carbons: experimental demonstration of the effects of nitrogen doping. *J. Am. Chem. Soc.*, 131, 16493–16499.

[267] Guan, C., Zhang, X., Wang, K., Yang, C. (2009). Investigation of H_2 storage in a templated carbon derived from zeolite Y and PFA. *Sep. Purif. Technol.*, 66, 565–569.

[268] Xia, Y., Yang, Z. and Mokaya, R. (2010). CVD nanocasting routes to zeolite-templated carbons for hydrogen storage. *Chem. Vap. Deposition*, 16, 322–328.

[269] Almasoudi, A. and Mokaya, R. (2014). Porosity modulation of activated ZIF-templated carbons via compaction for hydrogen and CO_2 storage applications. *J. Mater. Chem. A*, 2, 10960.

[270] Yang, Z., Xiong, W., Wang, J., Zhu, Y., Xia, Y. (2016) A systematic study on the preparation and hydrogen storage of zeolite 13X-templated microporous carbons. *Eur. J. Inorg. Chem.*, 2016, 2152–2158.

[271] Molefe, L.Y., Musyoka, N.M., Ren, J., Langmi, H.W., Mathe, M., Ndungu, P. G. (2019). Polymer-based shaping strategy for zeolite templated carbons (ZTC) and their metal organic framework (MOF) composites for improved hydrogen storage properties. *Front. Chem.*, 7.

[272] Bader, N., Abdelmottaleb, O. (2017). CO_2 activation of olive bagasse for hydrogen storage. *Environ. Prog. Sustain. Energy*, 36, 315–324.

[273] Guan, Y.L., Elkamel, A., Wang, K. (2015). Energy gas storage in template-synthesized carbons with different porous structures. *Can. J. Chem. Eng.*, 93, 527–531.

[274] Lamari Darkrim, F., Malbrunot, P. and Tartaglia, G.P. (2002). Review of hydrogen storage by adsorption in carbon nanotubes. *Int. J. Hydrogen Energy*, 27, 193–202.

[275] Lin, X., Jia, J., Zhao, X., Thomas, K. M., Blake, A. J., Walker G. S., Champness N. R., Hubberstey P., Schröder M. (2006) High H_2 adsorption by coordination-framework materials. *Angew. Chem. Int. Ed.*, 45, 7358–7364.

[276] Li, Y. and Yang, R.T. (2006). Significantly enhanced hydrogen storage in metal-organic frameworks via spillover. *J. Am. Chem. Soc.*, 128, 726–727.

[277] Yang, Z., Xia, Y. and Mokaya, R. (2007). Enhanced hydrogen storage capacity of high surface area zeolite-like carbon materials. *J. Am. Chem. Soc.*, 129, 1673–1679.

[278] Langmi, H. W., Book, D., Walton, A., Johnson, S. R., Al-Mamouri,M. M., Speight, J. D., Edwards, P. P., Harris, I. R., Anderson, P. A. (2005). Hydrogen storage in ion-exchanged zeolites. *J. Alloys Compd.*, 404, 637–642.

[279] Züttel, A., Nützenadel, C., Sudan, P., Mauron, P., Emmenegger, C., Rentsch, S., Schlapbach, L., Weidenkaff, A., Kiyobayashi T. (2002). Hydrogen sorption by carbon nanotubes and other carbon nanostructures. *J. Alloys Compd.*, 330, 676–682.

[280] Chen, P., Wu, X., Lin, J., Tan, K.L. (1999). High H_2 uptake by alkali-doped carbon nanotubes under ambient pressure and moderate temperatures. *Science*, 285(5424), 91-93.

[281] Zhao, X.B., Xiao, B., Fletcher, A.J., Thomas, K.M. (2005). Hydrogen adsorption on functionalized nanoporous activated carbons. *J. Phys. Chem. B*, 109, 8880–8888.

[282] Poirier, E., Chahine, R., Bénard, P., Cossement, D., Lafi, L., Mélançon, E., Bose, T.K., Désilets, S. (2004) Storage of hydrogen on single-walled carbon nanotubes and other carbon structures. *Appl. Phys. A Mater. Sci. Process.*, 78, 961–967

APPENDIX

Material	Properties of Material	Temperature (K)	Pressure (kPa)	H_2 Adsorption Capacity (wt%)	Reference
Zeolit	-	-	250.00	20.42	[213]
Cu(I)-[Al]-ZSM-5	Cu(I) doped zeolite	323	40	0.15	[214]
Fe_MWCNT	Fe doped carbon nanotube	77	101.325	1.96	[215]
Na-CHA	Zeolite	77	100.00	1.07	[29]
UiO-66(Zr)_(COOH)2	Acid modified MOF	269	3035	0.03	[216]
zeolite-X (bottom ash)	-	303	-	1.60	[204]
zeolite-X (on glass fiber)	-	303	-	4.94	[217]
ZTC-Nitrogen 5 mL	Zeolite-Y templated carbon	304	101	3.85	[218]
Cu(I)-[B]-SSZ-13	Cu(I) doped zeolite	303	101.325	0.05	[26]
Pt/AlS-N	Pt doped alumina templated carbon	77	2500	4.1	[219]
PEIS/ZEO/AL (60/10/30)	Hybrid nanoporous material	393	3200	2.0	[220]
CA-4700	Activated carbon	77	3000	8.9	[221]
SF-4600	Carbon	77	4000	11.2	[222]
BIK	Zeolite	77	298	1.27	[223]

M-3N	Zeolite	77	100	0.34	[31]
Sucrose-Zeolite-Y	Zeolite	323	100	1.72	[32]
MCM-41	Silicate mesoporous material	77	3500	2.01	[224]
MIL-101(Cr)/ZTC	Hybrid MOF/Zeolite templated carbon	77	100	2.55	[225]
AS-2M	Porous carbon	77	2000	6.8	[226]
MPPY4	Carbon	77	2000	14.2	[227]
10:100 Pd-Ni:MCM-41	Pd and Ni doped Silicate	298	4000	0.98	[228]
Com ZTC	Zeolite templated carbon	77	100	2.4	[229]
M2	Carbon nanotube	-	5.87	1.76	[230]
CAC1	Activated carbon	77	100	3.21	[231]
10Xc60-7S	Synthetic Zeolite	77	100	2.27	[232]
UZAR-S4	Stannosilicate	77	4000	4.2	[233]
Na-FAU(Si:Al=2.7)	Zeolite	77	100	1.21	[189]
SAC15-8	Activated carbon	298	8000	0.90	[234]
UCs-90-2	Carbon	77	2000	3.65	[235]
ZSM-5-O	Synthetic Zeolite	77	98	0.006	[34]
Sample III	Protein based material	303	4000	2.91	[236]
FA-ZTC2	Zeolite templated carbon	77	2000	6.6	[237]

A3	MOF	77	9000	3.22	[238]
ZTC8Pd-0.2	Zeolite templated carbon	77	2000	5.3	[239]
Zr-MOF	MOF	77	6000	4.2	[240]
ZTC-3	Zeolite templated carbon	303	30000	1.64	[241]
NaY	Synthetic Zeolite	77	101.3	1.16	[33]
AC-K6	Activated carbon	77	2000	7.08	[242]
MDC-1	MOF	77	100	3.25	[243]
SCEMC700	Sulfide doped microporous carbon	77	2000	4.43	[244]
ZTC-X	Zeolite templated carbon	77	2000	7.3	[245]
MIL-101TE (mod)	MOF	298	2000	1.34	[246]
MIL-101@SWNT-6	MOF/carbon nanotube	77	6000	8.60	[247]
CY8502	Zeolite templated carbon	77	100	1.8	[248]
IRMOF-1	MOF	77	1500	4.86	[249]
1%Pt-Ac	Activated carbon	77	100	2.0	[250]
IW 700	Zeolite templated carbon	77	100	1.59	[251]
CS29	Carbon	77	1100	3.422	[252]
750	Zeolite templated carbon	77	2000	5.4	[253]
SodZMOF	MOF	77	1000	1.6	[254]

RhSBA-15	Rh doped amorphous silica	77.4	112	0.85	[255]
Ac-ZTC1	Zeolite templated carbon	77	100	2.6	[256]
MIL100(Al)	MOF	77	4000	3.1	[257]
AC-900	Activated carbon	77	100	2.7	[258]
Li-LSX	Synthetic zeolite	77	101.325	1.50	[199]
RhETS-10	Rh doped titanosilicate	77.4	100	0.74	[259]
Pt/P7(2)-H	Zeolite templated carbon	303	10000	0.95	[260]
ETS-4(Rh)	Rh doped titanosilicate	77.4	100	0.59	[261]
DMA-rho-ZMOF	MOF	78	99.3	0.95	[262]
ZBDh	MOF	293	12000	0.51	[263]
1%Pt-C	Pt nanoparticle/ microporous carbon	77	100	2.8	[264]
1	Organic microporous crystal	77	1000	0.78	[265]
CMFAET	Carbon	77	2000	6.9	[266]
TC	Zeolite templated carbon	77	5000	3.1	[267]
CYETD	Zeolite templated carbon	77	100	4.9	[268]
AC-BF900at5Ton	ZIF templated carbon	77	2000	6.5	[269]
CXFAETS	Zeolite templated carbon	77	100	2.36	[270]
Pristine ZTC	Zeolite templated carbon	77	100	2.38	[271]

OB-CO2	Organic based material	77	100	1.69	[272]
C1050	Carbon	77	100	2.24	[273]
SWNT	Karbon nanotube	80	10000	11	[274]
Li-LSX (Si/Al 1.0)	Synthetic zeolite	77	101	1.5	[198]
1	COF	78	101	2.59	[275]
IRMOF-8	MOF	77	101.325	1.48	[276]
CB850h	Zeolitic carbon material	77	2000	6.9	[277]
CaX	Synthetic zeolite	77	1500	2.19	[278]
SWNT purified	Carbon nanotube	298	10000	2.0	[279]
Li-dopedCNT	Carbon nanotube	473-673	101.325	20.0	[280]
H-SSZ-13	Zeolite	77	92	1.28	[27]
G212	Activated carbon	77	100	2.10	[281]
H-Chabazite (Si/Al=2.1)	Zeolite	77	92	1.10	[28]
BT(X) Hipco (CNI)	Carbon	77	100	3.8	[282]

CURRICULUM VITAE

ORCID ID: 0000-0002-7067-5746

Name Surname **:**Orkun ERGÜRHAN

Foreign Language **:**English

Education and Professional Background:

- B.Sc. 2015. Ege University. Faculty of Science. Department of Physics
- M.Sc. 2019. Ege University. Institute of Science. General Physics
- 2019-Present. Research Assistant. Eskişehir Technical University. Faculty of Science. Department of Physics

Publications and Scientific Activities:

a) Articles published in international refereed journals:

1. Ergürhan Orkun, Erdoğan Burcu (2025). Effect of NH_4NO_3 pre-treatment on hydrogen adsorption properties of Na^+, K^+, Ag^+, Li^+, H^+, Ni^{2+}, Ca^{2+}, Cu^{2+} and Mg^{2+} exchanged natural clinoptilolite. International Journal of Hydrogen Energy. 144. 200-210. Doi: 10.1016/j.ijhydene.2025.06.054

2. Ergürhan Orkun, Erdoğan Burcu (2025). Hydrogen Adsorption Characteristics of Au and Li Decorated Nanowires on Bulk Silicon. Silicon. Doi:10.1007/s12633-025-03352-1

3. Ergürhan Orkun, Erdoğan Burcu (2024). Structural and Ammonia Adsorption Properties of the Gördes Clinoptilolite After HCl Acid Treatment. Gazi University Journal of Science. 37(4). 1902- 1916.. Doi: 10.35378/gujs.1311206

4. Erdoğan Burcu, Ergürhan Orkun (2024). Hydrogen adsorption on Ag^+. Ca^{2+} and Ni^{2+} exchanged chabazite: Influence of ammonium nitrate pretreatment and calcination. International Journal of Hydrogen Energy. 92. 801-809. Doi: 10.1016/j.ijhydene.2024.10.313

5. Erdoğan Burcu, Ergürhan Orkun (2024). Natural and pretreated Gördes clinoptilolites for ammonia removal: effect of exchangeable cations (Na^+, K^+, Ca^{2+}, and Mg^{2+}). Clay Minerals. 59(1). 39-49. Doi: 10.1180/clm.2024.5

6. Ergürhan Orkun, Erdoğan Burcu (2023). Effect of Calcination after NH4NO3 Modification of Natural Clinoptilolite on the Structural and Textural Properties. Russian Journal of Physical Chemistry A. 97(13). Doi: 10.1134/S0036024423130083

7. Erdoğan Burcu, Ergürhan Orkun. Anter Aslihan (2021). Influence of acid activation on the NH3-adsorption properties of a Turkish bentonite. Clay Minerals. 56(3). 7-184.. Doi: 10.1180/clm.2021.31

8. Ergürhan Orkun, Parlak Cemal. Alver Özgür. Şenyel Mustafa (2018). Conformational and electronic properties of hydroquinone adsorption on C60 fullerenes: Doping atom. solvent and basis set effects. Journal Of Molecular Structure. 1167. 5-231. Doi: 10.1016/j.molstruc.2018.04.092

b) Papers presented at international scientific meetings and published in proceedings:

1. Ergürhan Orkun, Erdoğan Burcu (2022). Influence of Calcination After NH_4NO_3 Modification on Bigadiç Clinoptilolite. International Dumlupınar Science & Mathematics Congress (Abstract/Oral Presentation)

2. Ergürhan Orkun, Erdoğan Burcu (2022). Influence of HCl activation on the Ammonia Adsorption Properties of Natural Clinoptilolite. 2nd International Conference on Applied Engineering and Natural Sciences (Abstract/Oral Presentation

3. Ergürhan Orkun, Erdoğan Burcu (2022). Effect Of Acid Activation on the Structure of Clinoptilolite. 2nd. International Symposium of Scientific Research and Innovative Studies. 1(1). 1161-1162. (Abstract/Oral Presentation)

c) Articles published in national refereed journals:

1. Ergürhan Orkun, Parlak Cemal. Alver Özgür (2021). Nonlinear Optical and Spectral Properties of Hydroquinone & Fullerene Systems. Eskişehir Teknik Üniversitesi Bilim ve Teknoloji Dergisi B- Teorik Bilimler. 9(2). 47-53. Doi: 10.20290/estubtdb.923753

d) Positions in Projects:

2025. Gümüş Katkılanmış ZIF-8' in Hidrojen Adsorpsiyon Özelliklerinin Tayini. Scientific Research Project Supported by Higher Education Institutions. Researcher. Eskişehir Technical University

2024. Ag^{+} Katkılı Klinoptilolitte Hidrojen Depolama. Scientific Research Project Supported by Higher Education Institutions. Researcher. Eskişehir Technical University

2024. İki Aşamalı Metal Destekli Kimyasal Aşındırma Yöntemiyle Sentezlenen Gözenekli Si Nanotellerin Fiziksel Adsorpsiyonla Hidrojen Depolama Kapasitesinin İncelenmesi. TÜBİTAK Project (1002). Manager. Eskişehir Technical Universtiy

2024. Hidrojen depolamada kullanılacak şabazit temelli bir malzemenin geliştirilmesi. TÜBİTAK Project (1002). Reseacher. Eskişehir Technical University

2023. Klinoptilolitin Gaz Adsorpsiyon Özelliklerine Farklı Katyon Formlarının Etkisi. Scientific Research Project Supported by Higher Education Institutions. Researcher. Eskişehir Technical University

2022. Doğal ve Sentetik Adsorbanların Hidrojen Adsorpsiyon Özelliklerinin Tayini. Scientific Research Project Supported by Higher Education Institutions. Researcher. Eskişehir Technical University

2021. Amonyak gazının klinoptilolit türü zeolitle uzaklaştırılması. Scientific Research Project Supported by Higher Education Institutions. Researcher. Eskişehir Technical University

Awards:

- 2025. Eskişehir Teknik Üniversitesi Bilim, Teknoloji Sanat ve Tasarım Ödülleri, Makale Performans Ödülü. Eskişehir.